

Experimental study of discrete symmetry in a compound nucleus

Takuya Okudaira

**Laboratory for Particle Properties
Department of Physics, Nagoya University**

February 2018

Abstract

CP-violation beyond the Standard Model is required in order to explain today's matter dominant universe. According to the CPT theorem, this implies that as-of-yet unknown T-violating effects should exist. Several T-violation searches, for example the search for a neutron electric dipole moment, have been carried out in the world. We are proposing a more sensitive T-violation search using a neutron induced compound nucleus.

Parity violating effects enhanced by up to 10^6 times compared to proton-proton scattering have been observed in several neutron induced compound nuclei. This P-violating effect occurs at a p-wave resonance located at the tail of an s-wave resonance and is theoretically explained as interference between an s-wave and a p-wave amplitudes (s-p mixing). There is a theoretical prediction that T-violating effects can also be enhanced in these nuclei under the assumption of the s-p mixing implying that T-violation can be searched for by making very sensitive measurements on the compound nucleus. However, the enhancement mechanism of the P-violation has not yet been studied well, and a more detail investigation is needed.

In order to study the enhancement mechanism, the angular distribution of the (n,γ) reaction was measured with ^{139}La , which is a possible candidate nucleus for the T-violation search due to its large enhanced P-violation, by using a high-quality germanium γ -ray detector assembly and a very intense neutron beam at J-PARC. Resulting from this measurement, a clear angular distribution of γ -rays from the p-wave resonance was found.

The angular distribution was analyzed within the framework of the s-p mixing, and the ratio of the partial p-wave neutron width to the neutron width in the entrance channel of the compound nucleus was determined. This result provides the basis to study the enhancement mechanism of P-violation in the compound nucleus. Moreover, the enhancement of T-violation in the compound nucleus was quantified using the results, and the experimental sensitivity of the T-violation search using ^{139}La was also discussed.

These results indicate a new possibility to adopt the enhancement mechanism of the discrete symmetry in the compound nucleus to the search for physics beyond the Standard Model.

Contents

1	Introduction	1
1.1	Discrete symmetry violation	1
1.2	Discrepancy between theoretical prediction by standard model and cosmological observation	2
1.3	Current status of search for the electric dipole moment	3
1.4	Overview and organization of this thesis	5
2	Discrete symmetry violation in a compound nucleus	9
2.1	PNC effect in a compound nucleus	9
2.1.1	PNC effect in proton-proton scattering	9
2.1.2	PNC effect in a compound nucleus	10
2.2	Enhancement of T-violation in a compound nucleus	13
2.3	Experimental principle of the T-violation search	15
2.4	The candidate nuclei for the T-violation search	18
2.5	Properties of the neutron absorption reaction of ^{139}La	20
3	The angular distribution in (n,γ) reaction	23
3.1	The angular distributions in (n, γ) reactions	23
3.2	The angular distributions in (n, γ) reactions for unpolarized neutrons	27
4	Facilities and experimental setup	31
4.1	Facility for the neutron beam	31
4.2	Beam Line 04 at MLF	33
4.2.1	Spatial distribution of the neutron beam	34
4.2.2	Energy resolution of the neutron beam	35
4.3	Germanium detector assembly	38
4.3.1	Energy calibration and linearity of pulse height	43
4.3.2	Definitions of symbols describing detector characteristics	43
4.3.3	Simulation of the germanium detectors	45
4.4	Data acquisition system	49
4.5	Nuclear targets	51

4.5.1	Lanthanum target	51
4.5.2	Boron carbide target	51
4.5.3	Melamine target	52
5	Measurement	53
5.1	Definitions of the symbols describing the measurement results	53
5.2	Measurement of the beam intensity spectrum	54
5.3	Measurement of the angular distribution in $^{139}\text{La}(n, \gamma)$ reactions	56
5.3.1	γ -ray spectrum and TOF spectrum	56
5.3.2	Fitting to obtain the resonance parameters	60
5.3.3	Correction for the relative photo-peak efficiency	62
5.3.4	Correction for the background γ -rays	64
5.3.5	Correction for the pileup of the detector signals	65
5.3.6	Angular Distribution	66
6	Analysis	71
6.1	Analysis to determine the partial γ width	71
6.2	Analysis using the formalism of the differential cross section of γ -rays in $^{139}\text{La}(n, \gamma)$ reactions	73
7	Discussion	79
7.1	More detailed analysis	79
7.2	Further analysis and experiments for the (n, γ) reaction	82
7.3	Estimation of the sensitivity for the T-violation search	86
7.3.1	Estimation of the upper limit of the W_T/W	86
7.3.2	Estimation of the forward scattering amplitude and an optimum target thickness .	87
7.3.3	Experimental setup	87
7.3.4	Estimation of the measurement time	91
8	Conclusion	93
A	Neutron absorption cross section	97

List of Figures

1.1	A schematics plot of the hierarchy of scales between the CP-odd source and three generic classes of observable EDMs.	4
1.2	The upper limit of the experimental value of nEDM.	6
2.1	Schematics of a p-wave resonance located at the tail of a large s-wave resonance	11
2.2	ϕ dependence of $\kappa(J)$ for $I=1/2$	11
2.3	Comparison of the ϕ dependence of $\kappa(J)$ for $^{139}\text{La}, ^{131}\text{Xe}, ^{117}\text{Sn}, ^{81}\text{Br}$	14
2.4	ϕ dependence of $\kappa(J)$ for $I=1/2$	17
2.5	Cross section of ^{139}La with neutron	20
2.6	Transitions from $^{139}\text{La}+n$ to ^{140}La	21
3.1	Feynman diagrams of the forward scattering	24
3.2	Neutron energy dependences of $a_0, a_{1x}, a_{1y}, a_{3xy}$ and a_{3yy} in $^{139}\text{La}(n,\gamma)$ reactions to the $F = 5$ final state	29
4.1	A bird's view of the J-PARC accelerators	32
4.2	Schematic of ANNRI installed on beamline 04 of J-PARC/MLF.	34
4.3	Spatial distributions of the neutron beam in ANNRI for a 22 mm-diameter beam	35
4.4	Examples of the simulated time structure of the neutron beam and fitting results	36
4.5	Energy dependence of the α, β, C and R in the Ikeda-Carpenter function	37
4.6	Energy resolution of the neutron beam at ANNRI	37
4.7	The simulation and measured value of the energy resolution of the neutron beam at ANNRI	38
4.8	Configuration of the germanium spectrometer assembly.	39
4.9	Schematics of the upper seven Type-A detectors.	40
4.10	Schematics of Type-B detectors.	41
4.11	The crystal shapes of type-A detectors and Type-B detectors	41
4.12	The schematics of a unit of type-B detector	42
4.13	The relationship the between pulse height and the photo-peak energy	43
4.14	Schematic of the definition of the photo-peak in the pulse height spectrum.	44

4.15	Comparison of the pulse height spectrum for γ -rays from a radioactive source ^{137}Cs and the numerical simulation for a type-B detector unit and a type-A detector unit	46
4.16	Comparison of pulse the height spectrum for prompt γ -rays emitted in the $^{14}\text{N}(\text{n},\gamma)$ reaction and the numerical simulation for a type-A detector unit and a type-B detector unit	46
4.17	Block diagram of the signal processing	50
4.18	Schematic of the signal processing	50
5.1	γ -ray spectrum with boron carbide target	54
5.2	TOF spectrum gated with 477 keV photo-peak with the boron carbide target.	55
5.3	Beam intensity spectrum measured with the boron carbide target	55
5.4	$\partial^2 I_\gamma / \partial t^m \partial E_\gamma^m$ 2-dimensional histogram of γ -rays with the lanthanum target as a function of leading-edge timing t^m and photo-peak γ -ray energy E_γ^m	56
5.5	Pulse height spectrum of γ -rays $\partial I_\gamma / \partial E_\gamma^m$ from the (n,γ) reaction with the lanthanum target as a function of E_γ^m	57
5.6	Expanded pulse height spectrum of γ -rays $\partial I_\gamma / \partial E_\gamma^m$ from the (n,γ) reaction with the lanthanum target as a function of E_γ^m	57
5.7	γ -ray count normalized by the incident beam intensity as a function of t^m for $E_\gamma^m \geq 2 \text{ MeV}$, which is referred to as $\partial I_\gamma / \partial t^m$	58
5.8	Magnified 2-dimensional histogram	59
5.9	Fitted result of the p-wave resonance. The solid line shows the best fit.	61
5.10	Pulse height spectrum of γ -rays $\partial I_\gamma / \partial E_\gamma^m$ from the (n,γ) reaction with the melamine target as a function of E_γ^m	62
5.11	Expanded pulse height spectrum of γ -rays $\partial I_\gamma / \partial E_\gamma^m$ from the (n,γ) reaction with the melamine target as a function of E_γ^m	63
5.12	Expanded $I_\gamma(E_\gamma^m)$ and an estimation of the background by the simulation	64
5.13	The neutron spectra gated with 5161 keV at $\bar{\theta}_d = 90^\circ$ before and after the correction for pileup events	65
5.14	$\partial N / \partial t^m$ in the vicinity of p-wave resonance for each $\bar{\theta}_d$	67
5.15	The Neutron energy dependence of the Legendre polynomial c_0 , c_1 and c_2	68
5.16	Visualization of the definition of N_L and N_H	69
5.17	Angular dependences of N_L and N_H	69
5.18	Angular dependences of A_{LH}	70
6.1	Comparison of the expanded $I_\gamma(E_\gamma^m)$ gated in the vicinities of the s_1 -wave resonance ($E_n^m = 0.2\text{-}0.4 \text{ eV}$), the p-wave resonance ($E_n^m = 0.6\text{-}0.9 \text{ eV}$), and the s_2 -wave resonance ($E_n^m = 70\text{-}75 \text{ eV}$)	72
6.2	TOF spectrum gated with the 5161 keV photo-peak with corrections for neutron beam spectrum, background γ -rays and pile up of the signals	73
6.3	Visualization of the value of ϕ on the xy -plane	77

6.4	Value of $ \kappa(J) $ as a function of ϕ	78
7.1	Angular dependences of $N_L - N_H$ and $N_L + N_H$	80
7.2	a_1 and a_3 on the xy -plane for the cases of $J_1 = J_2 = 4, J_3 = 3$	81
7.3	a_1 and a_3 on the xy -plane in the case of $J_1 = J_2 = J_3 = 3$	81
7.4	Neutron energy dependences of a_0 - a_{17} in $^{139}\text{La}(n,\gamma)$ reactions to the $F = 3$ final state using obtained x	83
7.5	Neutron energy dependences of a_0 - a_{17} in $^{139}\text{La}(n,\gamma)$ reactions to the $F = 4$ final state using obtained x	84
7.6	Neutron energy dependences of a_0 - a_{17} in $^{139}\text{La}(n,\gamma)$ reactions to the $F = 5$ final state using obtained x	85
7.7	Target thickness dependence of experimental sensitivity	88
7.8	Experimental setup to measure A_x	88
7.9	Experimental setup in order to measure P_x	89
7.10	Polarization, transmission and FOM of ^3He spin filter at 70% polarization of ^3He for neutron at $E_n = 0.74$ eV	90

List of Tables

2.1	The properties of the candidate nuclei for the T-violation search	19
2.2	Resonance parameters of ^{139}La	20
4.1	Design characteristics of the moderators at 10 m from the moderator surface at 1 MW of beam power at J-PARC	32
4.2	Parameters of RCS	33
4.3	Summary of χ^2/ndf between γ -ray spectrum of the melamine target and the simulated response function for each germanium detector.	47
4.4	Values of $\bar{P}_{d,p}/\bar{P}_{d,0}$ for $p = 0, 1, 2$ are shown for all detectors together with the weighted average angle of each detector $\bar{\theta}_d$ at $E_\gamma=0.662$ MeV and $E_\gamma=5.262$ MeV	48
4.5	The contaminations of the lanthanum target.	51
5.1	Resonance parameters of ^{139}La of the published value and the measured value in this work	60
5.2	The relative photo-peak efficiencies $\bar{\varepsilon}_d^{\text{pk},1/4}$ for all detectors. d20 and d22 detectors were not used.	63
6.1	Resonance parameters of ^{139}La used in the analysis	71

Chapter 1

Introduction

1.1 Discrete symmetry violation

Three discrete symmetries: charge conjugation (C), parity (P) and time reversal (T) transformations are defined in physics. Charge conjugation transformation means the change of a particle into its anti-particle. Parity transformation means the reversal of spatial coordinates. Time reversal means the reversal of the direction of time. The conservation of these symmetries in physics was believed in all fundamental interactions for a long time.

A possibility for P-violation in the weak interaction was proposed by Lee and Yang in 1956 [1]. The experiment to verify P-violation was carried out by measuring the angular distribution of electrons emitted from polarized ^{60}Co by Wu et al. in 1957 [2]. In this experiment, an asymmetric angular distribution with respect to the spin direction of ^{60}Co was observed exhibiting a direct evidence of P-violation. Subsequently, C-violation in the weak interaction with a meson decay was also discovered in the same year by Garwin et al. [3] and Friedman et al. [4].

In 1964, CP-violation in the weak interaction in neutral kaon decay was observed by Christenson et al. [5]. In that time, two kinds of kaon K_1 and K_2 which have different decay channels were observed. K_1 and K_2 decay to two pions ($\pi^0\pi^0$ and $\pi^+\pi^-$) and three pions ($\pi^0\pi^0\pi^0$ and $\pi^+\pi^-\pi^0$), respectively, and this implies that these two kaon are different CP eigenstates. On the other hand, other two kinds of kaon K_L and K_S , which have different life times $\tau_L = 5.2 \times 10^{-8}$ s and $\tau_S = 8.9 \times 10^{-11}$ s, were also observed. Before the experiment by Christenson et al, K_L and K_S were believed to be K_2 and K_1 , respectively. However, they found that K_L decays to two pions with a branching ratio of 2×10^{-3} . This implies that K_L and K_S do not equal to K_2 and K_1 and they are mixtures of the two CP eigenstates, which is an evidence of CP-violation [6]. Later, CP-violation was also discovered at neutral B meson decay at KEK [7] and SLAC [8].

The CP violation observed in these experiments can be fully described by the Standard Model. Two possible CP-violation sources exist in the Standard Model. One is the complex phase of the CKM matrix in the weak interaction. The flavor of quark can be changed by the weak interaction, and the weak current

is described as

$$j^\mu = (\bar{u}, \bar{c}, \bar{t}) \frac{\gamma^\mu(1 - \gamma^5)}{2} V_{\text{CKM}} \begin{pmatrix} d \\ s \\ b \end{pmatrix}, \quad (1.1)$$

where γ^μ is the gamma matrix, $\gamma = i\gamma^0\gamma^1\gamma^2\gamma^3$. Here V_{CKM} is a 3×3 matrix that describes the mixture of the flavors of quark and given as

$$V_{\text{CKM}} = \begin{pmatrix} V_{ud} & V_{us} & V_{ub} \\ V_{cd} & V_{cs} & V_{cb} \\ V_{td} & V_{ts} & V_{tb} \end{pmatrix} = \begin{pmatrix} c_{12}c_{13} & s_{12}c_{13} & s_{13}e^{-i\delta_{13}} \\ -s_{12}c_{23} - c_{12}c_{23}e^{-i\delta_{13}} & c_{12}c_{23} - s_{12}s_{23}s_{13}e^{-i\delta_{13}} & s_{23}c_{13} \\ s_{12}c_{23} - c_{12}c_{23}s_{13}e^{-i\delta_{13}} & -c_{12}c_{23} - s_{12}c_{23}s_{13}e^{-i\delta_{13}} & c_{23}c_{13} \end{pmatrix}, \quad (1.2)$$

where, $\theta_{12} = 13.04 \pm 0.05^\circ$, $\theta_{13} = 0.201 \pm 0.011^\circ$, $\theta_{23} = 2.38 \pm 0.06^\circ$, and $\delta_{13} = 1.20 \pm 0.08$ rad [9]. Here, c_i and s_i denote $\cos \theta_i$ and $\sin \theta_i$, respectively. Because the theory is CP-invariant when the matrix elements are real, a non-zero δ_{13} implies CP-violation. This CKM matrix can fully explain the experimental results.

The other CP-violating source in the Standard Model is the θ term in Quantum Chromodynamics (QCD). The Lagrangian of QCD is given as $L = L_{\text{QCD}} + L_\theta$, where L_{QCD} corresponds the strong interaction among quarks and gluons, which is CP-invariant term, and L_θ corresponds to a CP-violating term given as [10]

$$L_\theta = \frac{g^2}{32\pi^2} G^{\alpha\mu\nu} \tilde{G}_{\mu\nu}^\alpha \theta, \quad (1.3)$$

where $G^{\alpha\mu\nu}$ is the gluon field strength tensor, $\tilde{G}_{\mu\nu}^\alpha = \frac{1}{2}\epsilon_{\mu\nu\rho\sigma}G^{\alpha\rho\sigma}$, g is the strong coupling constant and θ is a constant implying the magnitude of CP-violation. This θ is determined by only experiments, and the neutron dipole moment search experiment, explained later, has given the upper limit of $\theta < \mathcal{O}(10^{-10})$. This implies that CP-violation in the strong interaction is very small, and is called the strong CP problem [11].

Although the P-, C- and CP-violation have been observed, the conservation of CPT transformation is believed due to the CPT theorem [12, 13]. According to the theorem, CPT transformation is always conserved if we assume the locality of the interaction, Lorentz invariance and hermiticity of the Hamiltonian, which are very fundamental physics principles. Therefore, the CPT theorem and experimental results of CP-violation result in the T-violation.

1.2 Discrepancy between theoretical prediction by standard model and cosmological observation

The Standard Model can fully explain the experimental results of CP-violation. However, there is a discrepancy between theoretical prediction by the Standard Model and cosmological observation.

In the early universe, the same number of baryons and anti-baryons were created and annihilated to photons. If there was no symmetry violation between baryons and anti-baryons, baryons would not exist in today's universe. The asymmetry between baryons and anti-baryons is evaluated by using η as

$$\eta = \frac{n_B - n_{\bar{B}}}{n_B + n_{\bar{B}}}, \quad (1.4)$$

where n_B and $n_{\bar{B}}$ are numbers of baryons and anti-baryons, respectively. Since $n_B - n_{\bar{B}}$ is the number of baryons left in today's universe and $n_B + n_{\bar{B}}$ is the number of photons generated from the annihilation of baryons and anti-baryons, the ratio of the number of baryons to the number of photons quantifies the amount of symmetry violation. This ratio was measured from results of observations of cosmic microwave background radiation, and found to be

$$\frac{n_B - n_{\bar{B}}}{n_B + n_{\bar{B}}} = \frac{n_B - n_{\bar{B}}}{n_\gamma} \sim 10^{-9}, \quad (1.5)$$

where n_γ is the number of photons. On the other hand, the ratio by theoretical estimation using the Standard Model is

$$\frac{n_B - n_{\bar{B}}}{n_B + n_{\bar{B}}} \sim 10^{-18} [14]. \quad (1.6)$$

This 10^9 discrepancy is one of the most important problems in physics. This large discrepancy implies the Standard Model cannot explain today's matter-dominated universe.

In 1967, Sakharov proposed the conditions to generate today's matter-dominated universe, known as the Sakharov conditions [15]:

1. Baryon number violation
2. C- and CP-violation
3. Processes outside of thermal equilibrium

The 2nd condition strongly suggests that there should be an unknown CP-violation source. This implies the existence of an unknown T-violation source by invoking the CPT theorem.

1.3 Current status of search for the electric dipole moment

Several T-violation searches have been carried out in the world. The best limit for the T-violation is given by the Electric dipole moment (EDM) search. Fig 1.1 shows the hierarchy of scales between the CP-odd sources and three generic classes of observable EDMs. The fundamental CP-violation appears as several observables through different paths as shown in Fig 1.1. Therefore the results from different observables complement each other in searching for fundamental CP-violation.

The reason why a non-zero value of the permanent EDM violates T-symmetry is explained as follows. If

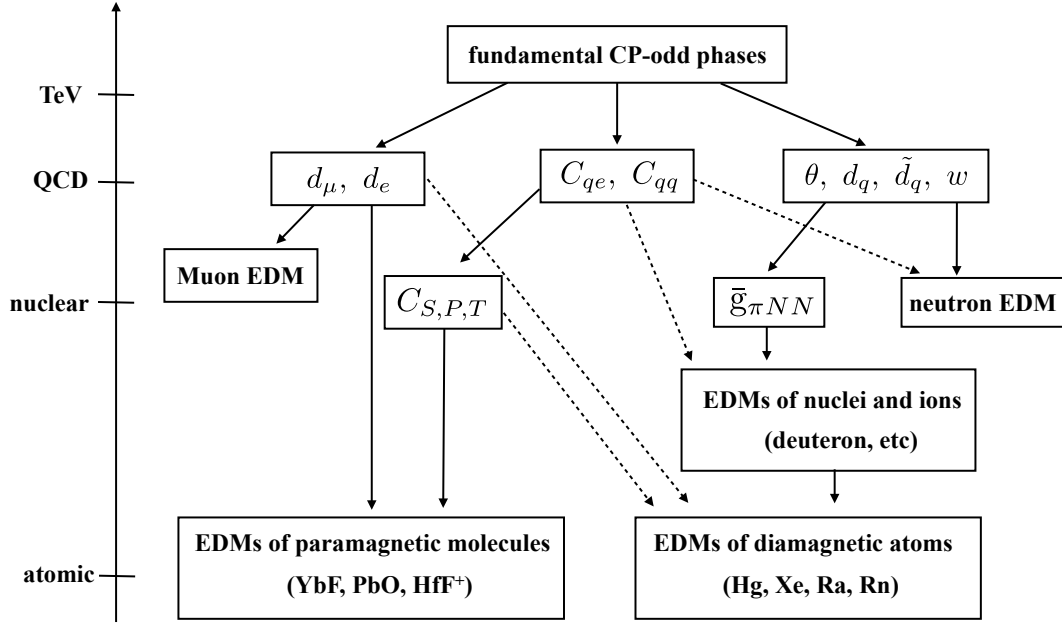


Figure 1.1: A schematics plot of the hierarchy of scales between the CP-odd source and three generic classes of observable EDMs. The dashed lines indicate generically weaker dependencies [16].

a particle which has a magnetic moment μ and an electric dipole moment d is placed in a magnetic field B and an electric field E , the potential of the particle U can be described as

$$U = -\mu \cdot B - d \cdot E. \quad (1.7)$$

In T transformed coordinates, B , E , μ and d are transformed as

$$B \rightarrow -B, E \rightarrow E, \mu \rightarrow -\mu, d \rightarrow -d. \quad (1.8)$$

Therefore U is transformed in T transformed coordinates as

$$U = -\mu \cdot B + d \cdot E. \quad (1.9)$$

If d is non-zero, the potential U will change by the T transformation. Hence a non-zero EDM value of the particle implies T-violation.

Experimental searches for EDM have been carried out on several elementary particles and atoms. For charged particle such as electrons, it is difficult to distinguish the effects of EDM from the Coulomb force and the Lorentz force. Therefore electrons bounded in atoms have been studied using the Cerium atom [17], Thallium atom [18, 19] and so on, which has one unpaired electron. In a non-relativistic neutral system, any applied electric field will be shielded and the effect of the EDM will not appear, which is referred to as the Schiff shielding theorem. However, in fact, this theorem is violated in heavy

atoms due to the relativistic effect, and the effect of EDM can be detected. This violating effect is strongly enhanced with a large atomic number, and the paramagnetic enhancement of the electron EDM is given by [20, 21, 22]

$$d_{\text{para}}(d_e) \sim 10 \frac{Z^3 \alpha}{J(J+1/2)(J+1)^2} d_e, \quad (1.10)$$

where J is the angular momentum and Z is the atomic number. The current best limit on the electron EDM is given by a measurement using the molecule YbF [23] as,

$$|d_e| < 10.5 \times 10^{-28} \text{ e} \cdot \text{cm} \text{ (90\%C.L.)}. \quad (1.11)$$

On the other hand, nuclear EDMs have been studied in massive atoms such as xenon and mercury, whose total electron angular spin equal zero. Although this method has the advantage of accumulating statistics over a long time, the effect from EDM will be reduced by the interaction of the electron cloud with the E field [24]. The best limit for nuclear EDM is given by the measurement using ^{199}Hg as [25]

$$|d_{\text{Hg}}| < 3.1 \times 10^{-29} \text{ e} \cdot \text{cm} \text{ (95\%C.L.)}. \quad (1.12)$$

The neutron EDM (nEDM) has also been studied for a long time. It is advantageous in that the neutron is a more simple system than the massive atom to compare experimental results with theoretical calculations. However it is hard to collect statistics over a long time due to the short life time of the neutron and a difficulty in generating neutrons. The history of the upper limit of the nEDM is shown in Fig 1.2. Currently the most sensitive nEDM search is given by the measurement using a storage method with ultracold neutrons (UCN) at ILL as

$$|d_n| < 2.9 \times 10^{-26} \text{ e} \cdot \text{cm} \text{ (90\%C.L.)}. \quad (1.13)$$

The nuclear EDM can be used to estimate the nEDM, and the limit from ^{199}Hg gives a similar sensitivity to the above nEDM limits.

Although a new type of neutron source for high-density UCN, which enables us to probe the nEDM on the order of 10^{-27} to 10^{-28} e·cm, has been internationally developed, the improvement of the upper limit of the nEDM has saturated in recent years as shown in Fig 1.2. Thus a completely different method with different systematic uncertainties is required to improve the experimental sensitivity to search for T-violation.

1.4 Overview and organization of this thesis

We are proposing a new method to search for T-violation using a neutron induced compound nucleus. Large enhanced P-violation has been observed in the neutron induced compound nucleus due to the in-

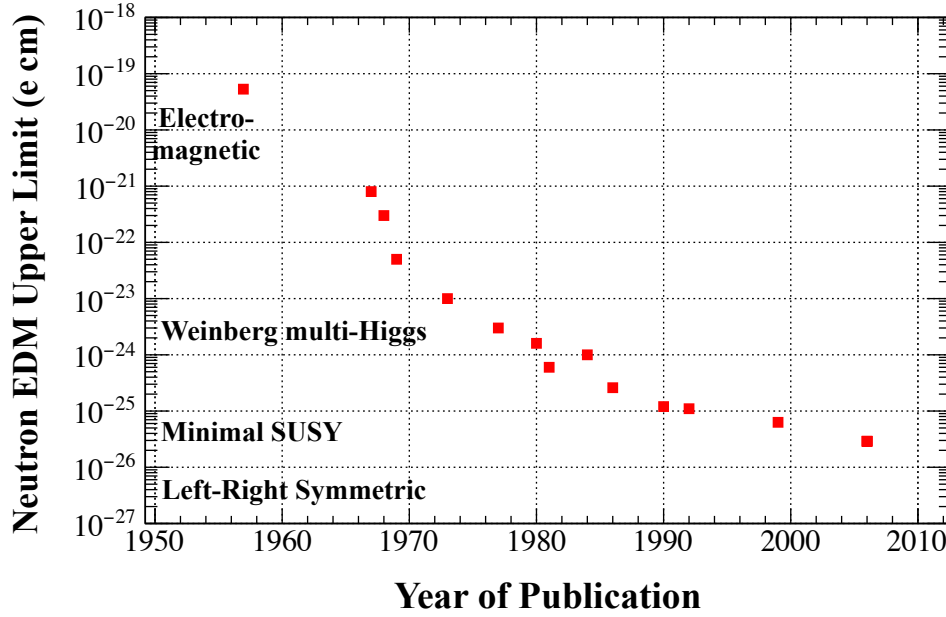


Figure 1.2: The upper limit of the experimental value of nEDM. [26, 27, 28, 29, 30, 31, 32, 33, 34, 35, 36, 37, 38, 39, 40].

interference between an s-wave resonance and a p-wave resonance. There is a theoretical prediction that the CP-violation in the nucleon-nucleon interaction, in which CP-violation in $g_{\pi NN}$ coupling in Fig 1.2, is enhanced in a neutron induced compound nucleus in the same mechanism, and the effect can be observed by measuring the T-odd term in the forward scattering amplitude of a polarized neutron with a polarized nucleus. However, the enhancement factor $\kappa(J)$, which represents the sensitivity for the T-violation search, has not been determined yet in all nuclei, and the experimental sensitivity to T-violation depends on properties of the target nucleus. Therefore, a target nucleus to use in the experiment needs to be selected carefully by measuring $\kappa(J)$. The details of the theory and the principles of the experimental method of the T-violation search are discussed in Chapter 2. The properties of the candidate nuclei are also summarized there.

Initial tests to select the candidate nuclei and verify the principles are carried out on beam line 04 at MLF in J-PARC. These tests consist of measuring the angular distribution of emitted γ -rays in neutron absorption reactions of the target nucleus. My research focuses on the measurement and analysis of the angular distribution of the emitted γ -rays. The principles of the angular distribution measurement are given in Chapter 3.

The measurement was performed with ^{139}La , which is a first candidate nuclei for the T-violation search, by using a very intense neutron beam and a high resolution germanium detector assembly. The facilities and experimental setup are described in Chapter 4.

Resulting from the measurement, a clear γ -ray angular distribution from a neutron induced compound nucleus was observed and the important parameter $\kappa(J)$ was determined for the first time. The measurement results and analysis are described in Chapter 5 and Chapter 6, respectively.

More detailed analysis, further experiments for the detailed study and the experimental sensitivity for the T-violation search are discussed in Chapter 7. Finally this thesis concludes in Chapter 8.

Chapter 2

Discrete symmetry violation in a compound nucleus

In this section, discrete symmetry violation in a neutron induced compound nucleus is described.

2.1 PNC effect in a compound nucleus

2.1.1 PNC effect in proton-proton scattering

In the nucleon-nucleon interaction where the strong interaction is dominant, parity non-conserving (PNC) effect caused by the weak interaction is very small. PNC effect in proton-proton scattering has been observed by several experimental groups who measured the longitudinal asymmetry of the scattering cross section using a polarized proton beam and an unpolarized proton target. The longitudinal asymmetry, A_{pp} , is given as

$$A_{pp} = \frac{\sigma_{pp}^+ - \sigma_{pp}^-}{\sigma_{pp}^+ + \sigma_{pp}^-}, \quad (2.1)$$

where σ_{pp}^+ and σ_{pp}^- are the scattering cross sections of the unpolarized proton to positive and negative helicity proton respectively. A_{pp} was measured at several incident proton energies and values were approximately 10^{-7} [41, 42, 43].

This P-violating effect is theoretically explained as follows. The total scattering amplitude f consists of the parity conserving part f_{PC} and the parity non-conserving part f_{PNC} as

$$\begin{aligned} |f|^2 &= |f_{PC} + f_{PNC}|^2 \\ &= |f_{PC}|^2 \left(1 + \frac{f_{PC} f_{PNC}^* + f_{PC}^* f_{PNC}}{|f_{PC}|^2} + \frac{|f_{PNC}|^2}{|f_{PC}|^2} \right). \end{aligned} \quad (2.2)$$

The asymmetry corresponds to the second term of Eq. 2.2.

$$\begin{aligned}
 A_{\text{pp}} &\approx \frac{f_{\text{PC}} f_{\text{PNC}}^* + f_{\text{PC}}^* f_{\text{PNC}}}{|f_{\text{PC}}|^2} \approx \frac{|f_{\text{PNC}}|}{|f_{\text{PC}}|} \\
 &\approx \frac{V_{\text{PNC}}}{V_{\text{PC}}} \approx G_{\text{F}} m_{\pi}^2 \\
 &\approx 2 \times 10^{-7}.
 \end{aligned} \tag{2.3}$$

Here, V_{PNC} and V_{PC} are the parity conserving and the parity non-conserving light meson exchange potential and G_{F} and m_{π} are the Fermi coupling constant and the pion mass, respectively. This theoretical estimation is consistent with the experimental results.

2.1.2 PNC effect in a compound nucleus

The compound nucleus model was introduced by Niels Bohr in 1936. An incident particle is captured by a target nucleus and the nucleus becomes an excited state that has a long lifetime of the order of $10^{-18} \sim 10^{-16}$ s, called "compound nucleus". This lifetime is long enough to share the energy of the incident particle among all nucleons and the information of the entrance channel is lost by a large number of the collisions between nucleons. As a result, a complete statistical equilibrium is established in the compound nucleus. Subsequently, particles, for example, γ , neutron or proton, are emitted from the compound nucleus as an exit channel.

In several neutron induced compound nuclei, large P-violation up to 10^{-1} has been observed. The P-violation was evaluated as a longitudinal asymmetry A_{L} of the helicity dependence of the neutron absorption cross section as

$$A_{\text{L}} = \frac{\sigma_{\text{abs}}^+ - \sigma_{\text{abs}}^-}{\sigma_{\text{abs}}^+ + \sigma_{\text{abs}}^-}, \tag{2.4}$$

where σ_{abs}^+ and σ_{abs}^- are the neutron absorption cross section of target nucleus corresponding to positive and negative helicity neutrons respectively. This large P-violation has been observed in the vicinity of p-wave (neutron orbital angular momentum $l = 1$) resonances located at the tail of large s-wave ($l = 0$) resonances, shown as Fig 2.1, in neutron absorption reactions of ^{139}La , ^{131}Xe , ^{117}Sn , ^{115}In , ^{81}Br and so on. This implies that the P-violation in nucleon-nucleon interactions is enhanced by up to 10^6 times in the p-wave resonance of a neutron induced compound nucleus. The observed large P-violation in several nuclei are shown in Fig 2.2.

Theoretically, the large enhancement of the P-violation is explained as an interference of an s-wave resonance amplitude and a p-wave amplitude (s-p mixing) as follows. The angular momentum of the incident neutron can be written as

$$\mathbf{j} = \mathbf{l} + \mathbf{s}, \tag{2.5}$$

where l is the orbital angular momentum of the incident neutron and s is its spin. The p-wave amplitude can be one of two state of $j = 1/2$ or $j = 3/2$. On the other hand, the s-wave amplitude can only allow

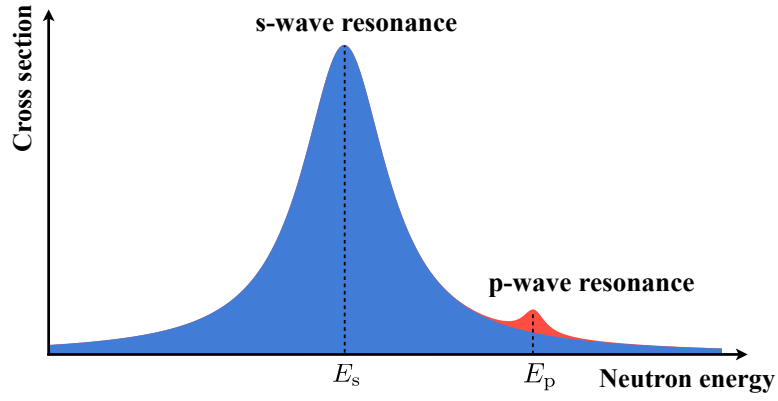


Figure 2.1: Schematics of a p-wave resonance located at the tail of a large s-wave resonance. The large enhanced P-violation has been observed at such p-wave resonance.

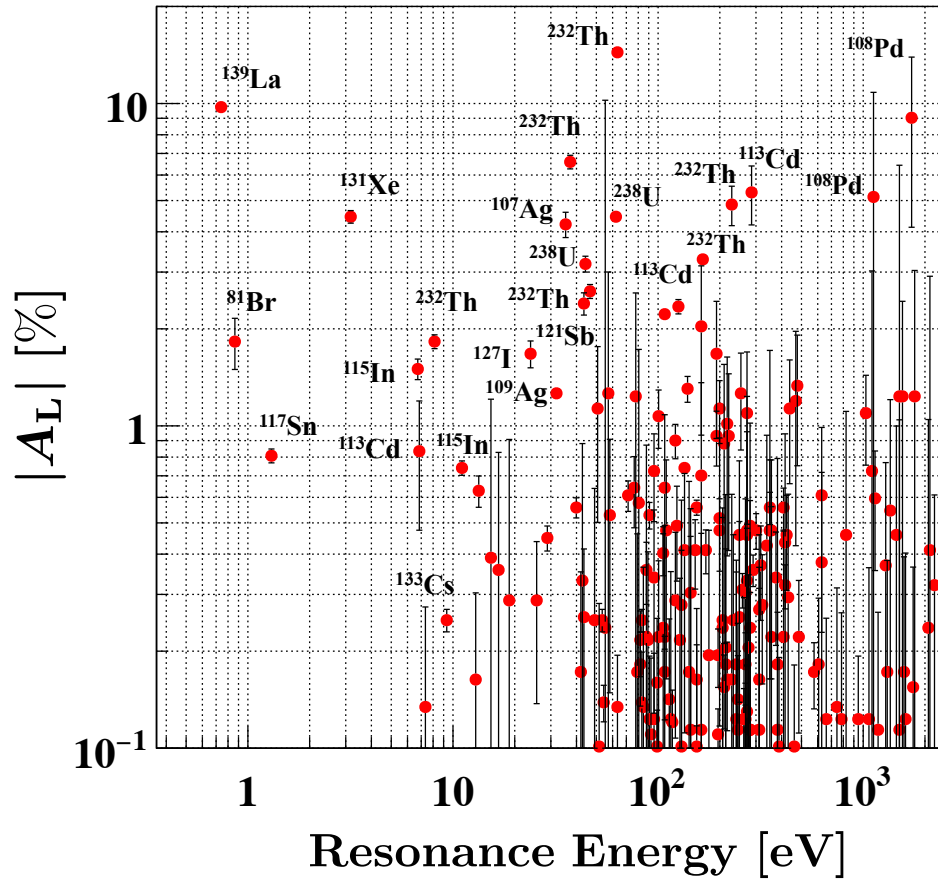


Figure 2.2: Longitudinal asymmetry of several nuclei.

$j = 1/2$ state. The neutron width of s-wave resonance Γ_s^n and p-wave resonance Γ_p^n can be written as

$$\Gamma_p^n = \Gamma_{p,j=\frac{1}{2}}^n + \Gamma_{p,j=\frac{3}{2}}^n, \quad \Gamma_s^n = \Gamma_{s,j=\frac{1}{2}}^n. \quad (2.6)$$

When the angular momentum of the compound state J is the same in the s-wave and the p-wave state, these two opposite parity amplitude: $j = 1/2$ states of the s-wave amplitude and $j = 1/2$ states of the p-wave amplitude can interfere with one another via the weak interaction. As nucleons can interact with each other for much longer time in a compound state than in a direct process, this parity mixing between two opposite parity amplitudes can be much larger in the compound state than in a direct process.

The value of A_L corresponding to the enhanced P-violation can be theoretically described as

$$A_L \simeq -\frac{2xW}{E_p - E_s} \sqrt{\frac{\Gamma_s^n}{\Gamma_p^n}}, \quad (2.7)$$

where E_s and E_p are the resonance energies of the s-wave and the p-wave resonance and W is the matrix element of the transition from the s-wave (p-wave) state to the p-wave (s-wave) state via the weak interaction. Here x is given as

$$x = \sqrt{\frac{\Gamma_{p,j=\frac{1}{2}}^n}{\Gamma_p^n}}. \quad (2.8)$$

The magnitude of A_L can be theoretically estimated as follows. The Hamiltonian of the compound state consists of a parity conserving part H_{PC} and a parity non-conserving part H_{NPC} . If the s-wave amplitude and p-wave amplitude are mixed, the mixed s-wave and p-wave amplitudes $|s'\rangle$, $|p'\rangle$ can be written as

$$|s'\rangle = |s\rangle - \frac{\langle s| H_{NPC} |p\rangle}{E_p - E_s} |p\rangle, \quad |p'\rangle = |p\rangle - \frac{\langle p| H_{NPC} |s\rangle}{E_p - E_s} |s\rangle, \quad (2.9)$$

where $|s\rangle$ and $|p\rangle$ are s-wave and p-wave amplitudes and E_s and E_p are the resonance energy of s-wave resonance and p-wave resonance, respectively. The weak matrix element W corresponds to $\langle s| H_{NPC} |p\rangle$. The s-wave and p-wave state can be described as an expansion in a number of single particle-hole states in the nuclear shell model as

$$|s\rangle = \sum_i^N a_i |i\rangle, \quad |p\rangle = \sum_j^N b_j |j\rangle, \quad (2.10)$$

where N is a number of states. The magnitude of a_i and b_i are on the order of $1/\sqrt{N}$ because of the normalization requirements of $|s\rangle$ and $|p\rangle$. N can be estimated as

$$N \sim \frac{\Delta E}{D}, \quad (2.11)$$

where ΔE is the energy required to excite one nucleus from the ground state and D is the energy difference between the states. If we use the typical values of $\Delta E \sim 10^6$ eV and $D \sim 10$ eV, we

obtain $N \sim 10^5$. Therefore the weak matrix element can be described as

$$\begin{aligned}
 |W| &= |\langle s | H_{\text{PNC}} | p \rangle| \\
 &= \left| \sum_{ij}^N a_i b_j \langle i | H_{\text{PNC}} | j \rangle \right| \\
 &\sim \frac{\overline{\langle i | H_{\text{PNC}} | j \rangle}}{N} \times \sqrt{N}.
 \end{aligned} \tag{2.12}$$

Here, the condition that the phase of a_i and b_j appear at random are used in Eq 2.12. Therefore $2W/E_p - E_s$ in Eq 2.7 can be written as

$$\frac{2W}{E_p - E_s} \sim \frac{|W|}{D} \sim \frac{\overline{\langle i | H_{\text{PNC}} | j \rangle}}{\Delta E} \sqrt{N}, \tag{2.13}$$

where $\overline{\langle i | H_{\text{PNC}} | j \rangle}/\Delta E$ is the magnitude of the P-violating effect in the single particle state which is order of $\sim 10^{-7}$, and $\sqrt{N} = 10^2 \sim 10^3$. The factor $2W/(E_p - E_s)$ is referred to as "dynamic enhancement".

On the other hand, $\sqrt{\Gamma_s^n/\Gamma_p^n}$ in Eq 2.7 is referred to as "structural enhancement". The neutron width is proportional to a factor of the centrifugal potential, $(kR)^{2l+1}$. If we use typical values of $k \sim 2 \times 10^{-4} \text{ fm}^{-1}$ and $R \sim 10 \text{ fm}$, this enhancement factor $\sqrt{\Gamma_s^n/\Gamma_p^n}$ is approximately 10^3 . If we assume that x is the order of 1, we can obtain $A_L \sim 10^{-1}$, and the large enhancement in the compound nucleus can be explained theoretically. However, x has not been determined experimentally.

2.2 Enhancement of T-violation in a compound nucleus

V. P. Gudkov predicted that CP-violation can be also enhanced through the same mechanism as in the enhancement of P-violation [44]. This effect can be studied by measuring the T-violating cross section of neutron absorption. The wave function $|lsI\rangle$ is transformed as $(-1)^l |lsI\rangle$ in a P transformation. On the other hand, the T transformed wave function becomes $(-1)^{i\pi S_y} K |lsI\rangle$. Here, I is the spin of the target nucleus, and the channel spin S is defined as $S = s + I$. The T-violation is caused by the interference between states which have different channel spin.

The T-violating cross section $\Delta\sigma_T$ is written as

$$\Delta\sigma_T = \kappa(J) \frac{W_T}{W} \Delta\sigma_P, \tag{2.14}$$

where $\Delta\sigma_P$ is the P-violating cross section, W_T and W are the T-violating and P-violating matrix elements, and $\kappa(J)$ is a spin factor. $\kappa(J)$ is represented by two channel spin components of $S = I + 1/2$ and $S = I - 1/2$ and the spin of the target nucleus I , and represented as

$$x^2 = \frac{\Gamma_{p,j=\frac{1}{2}}^n}{\Gamma_p^n}, \quad y^2 = \frac{\Gamma_{p,j=\frac{3}{2}}^n}{\Gamma_p^n}. \tag{2.15}$$

x and y satisfy

$$x^2 + y^2 = 1 \quad (2.16)$$

due to the relation $\Gamma_p^n = \Gamma_{p,j=\frac{1}{2}}^n + \Gamma_{p,j=\frac{3}{2}}^n$. A mixing angle ϕ of $j = 1/2$ and $j = 3/2$ components can then be defined as

$$x = \cos \phi, \quad y = \sin \phi. \quad (2.17)$$

$\kappa(J)$ is given as a function of x and y for the case of $J = I - \frac{1}{2}$ and $J = I + \frac{1}{2}$

$$\kappa(J) = \begin{cases} (-1)^{2I} \left(1 + \frac{1}{2} \sqrt{\frac{2I-1}{I+1}} \frac{y}{x} \right) & (J = I - \frac{1}{2}) \\ (-1)^{2I+1} \frac{I}{I+1} \left(1 - \frac{1}{2} \sqrt{\frac{2I+3}{I}} \frac{y}{x} \right) & (J = I + \frac{1}{2}) \end{cases}.$$

The formula indicates that the T-violation sensitivity strongly depends on the value of x and y or ϕ . As examples, ϕ dependencies of $\kappa(J)$ of ^{139}La , ^{131}Xe , ^{81}Br and ^{117}Sn are shown in Fig 2.3. The value of $\kappa(J)$ has not yet been measured in all nuclei, and it is necessary to determine $\kappa(J)$ to estimate the T-violating cross section by measuring x .

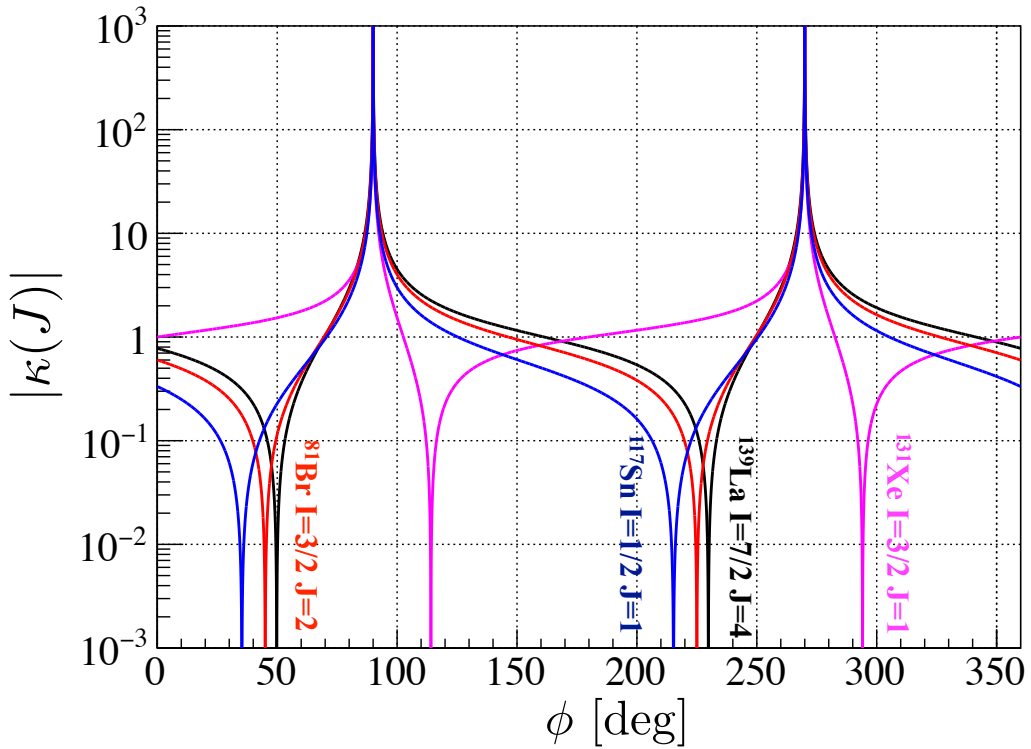


Figure 2.3: Comparison of the ϕ dependence of $\kappa(J)$ for ^{139}La (black line), ^{131}Xe (pink line), ^{117}Sn (blue line) and ^{81}Br (red line).

2.3 Experimental principle of the T-violation search

Since the T-violating effect can be enhanced in the nucleus similar to the enhanced P-violation as shown in the previous section, the T-violation can be searched for with high precision using a compound nucleus. The best method to search for the T-violating effect is a measurement of a neutron transmission. This method has the advantage that T-odd effects due to the final-state interaction are expected to be negligibly small because neutron propagation does not change in the process of passing through the target. In this section, the experimental principle to search for T-violation using the neutron transmission method is described.

If the polarization of the target nucleus is a pure vector polarization, the forward scattering amplitude f can be written as

$$f = A' + B'\boldsymbol{\sigma} \cdot \hat{\mathbf{I}} + C'\boldsymbol{\sigma} \cdot \hat{\mathbf{k}} + D'\boldsymbol{\sigma} \cdot (\hat{\mathbf{I}} \times \hat{\mathbf{k}}), \quad (2.18)$$

where $\boldsymbol{\sigma}$, $\hat{\mathbf{I}}$ and $\hat{\mathbf{k}}$ are the spin of incident neutron, the spin of the target nucleus and the momentum of the neutron, respectively. When the neutron goes through a material, the incoming neutron spin state U_i is transformed into the outgoing neutron spin state U_f given as

$$\begin{aligned} U_f &= \mathfrak{S}U_i, \\ \mathfrak{S} &= e^{i(n-1)kz}, \\ n &= 1 + \frac{2\pi\rho}{k^2}f, \end{aligned} \quad (2.19)$$

where z is the thickness of the target, ρ is the number density of the material and k is the neutron wave length. Here \mathfrak{S} is described as

$$\mathfrak{S} = A + B\boldsymbol{\sigma} \cdot \hat{\mathbf{I}} + C\boldsymbol{\sigma} \cdot \hat{\mathbf{k}} + D\boldsymbol{\sigma} \cdot (\hat{\mathbf{I}} \times \hat{\mathbf{k}}), \quad (2.20)$$

$$\begin{aligned} A &= e^{iZA'} \cos b, \\ B &= e^{iZA'} \frac{\sin b}{b} ZB', \\ C &= e^{iZA'} \frac{\sin b}{b} ZC', \\ D &= e^{iZA'} \frac{\sin b}{b} ZD', \\ Z &= \frac{2\pi\rho z}{k}, \\ b &= Z\sqrt{B'^2 + C'^2 + D'^2}. \end{aligned} \quad (2.21)$$

A is the spin independent (P-even, T-even) term corresponding to the neutron absorption cross section. B is the spin dependent (P-even, T-even) term corresponding to a neutron spin rotation through the

polarized target called "pseudo-magnetic effect". C is the P-violating (P-odd, T-even) term, which is enhanced for some nuclei discussed previously. D is the T-violating (P-odd, T-odd) term corresponding to the T-violating cross section in Eq. 2.14. Therefore a non-zero value of D implies T-violation. Note that Eq 2.18 is the formalism in the case of $I = 1/2$, and we need to add tensor terms to the forward scattering amplitude in the case of $I > 1/2$. However, contributions of the tensor terms are typically smaller than that of other terms and ignored in this thesis for the rough estimation of the D term. The explicit formalism of the higher rank terms will be published [45].

There are six possible ways to measure D experimentally as shown in Fig 2.4. A coordinate system defines the beam axis as z -axis, the vertical direction as y -axis and the x -axis is such that they form a right-handed coordinate system. D can be searched most sensitively by measuring the analyzing power A_x and the polarization P_x . The analyzing power is defined as the efficiency that the x component of neutrons initially polarized along the x -axis is transmitted through a y -polarized nuclear target, and can be written as

$$A_x \equiv \text{Tr} \left[\mathfrak{S}^\dagger \sigma_x \mathfrak{S} \right] = 4(\text{Re}A^*D + \text{Im}B^*C). \quad (2.22)$$

The polarization is the increase in the x component of initially unpolarized neutrons after passing through a y -polarized nuclear target, and can be written as

$$P_x \equiv \text{Tr} \left[\sigma_x \mathfrak{S}^\dagger \mathfrak{S} \right] = 4(\text{Re}A^*D - \text{Im}B^*C). \quad (2.23)$$

In this case, the experimental sensitivity is given as $8\text{Re}A^*D$, which is obtained by the sum of the analyzing power and the polarization. Note that K_x^x in Fig. 2.4 denotes a polarization in the x component of initially x -polarized neutrons after passing through a y -polarized nuclear target, and K_x^x and K_{-x}^{-x} are defined as

$$\begin{aligned} K_x^x &\equiv \text{Tr} \left[\frac{1 + \sigma_x}{2} \mathfrak{S}^\dagger \frac{1 + \sigma_x}{2} \mathfrak{S} \right] = |A|^2 + 2\text{Re}A^*D + |D|^2, \\ K_{-x}^{-x} &\equiv \text{Tr} \left[\frac{1 - \sigma_x}{2} \mathfrak{S}^\dagger \frac{1 - \sigma_x}{2} \mathfrak{S} \right] = |A|^2 - 2\text{Re}A^*D + |D|^2. \end{aligned} \quad (2.24)$$

Since D is proportional to $\Delta\sigma_T$, the experimental sensitivity can be estimated from the values of A , $\kappa(J)$, W_T/W and $\Delta\sigma_P$. The values of A and $\Delta\sigma_P$ have been measured as the neutron capture cross section and the longitudinal asymmetry, respectively. The upper limit of W_T/W has been given by the experimental search for the EDM. However, $\kappa(J)$ has not been measured yet in all of compound nuclei, and it is desirable to determine the value $\kappa(J)$ for the candidate nuclei of the T-violation search in order to estimate the experimental sensitivity.

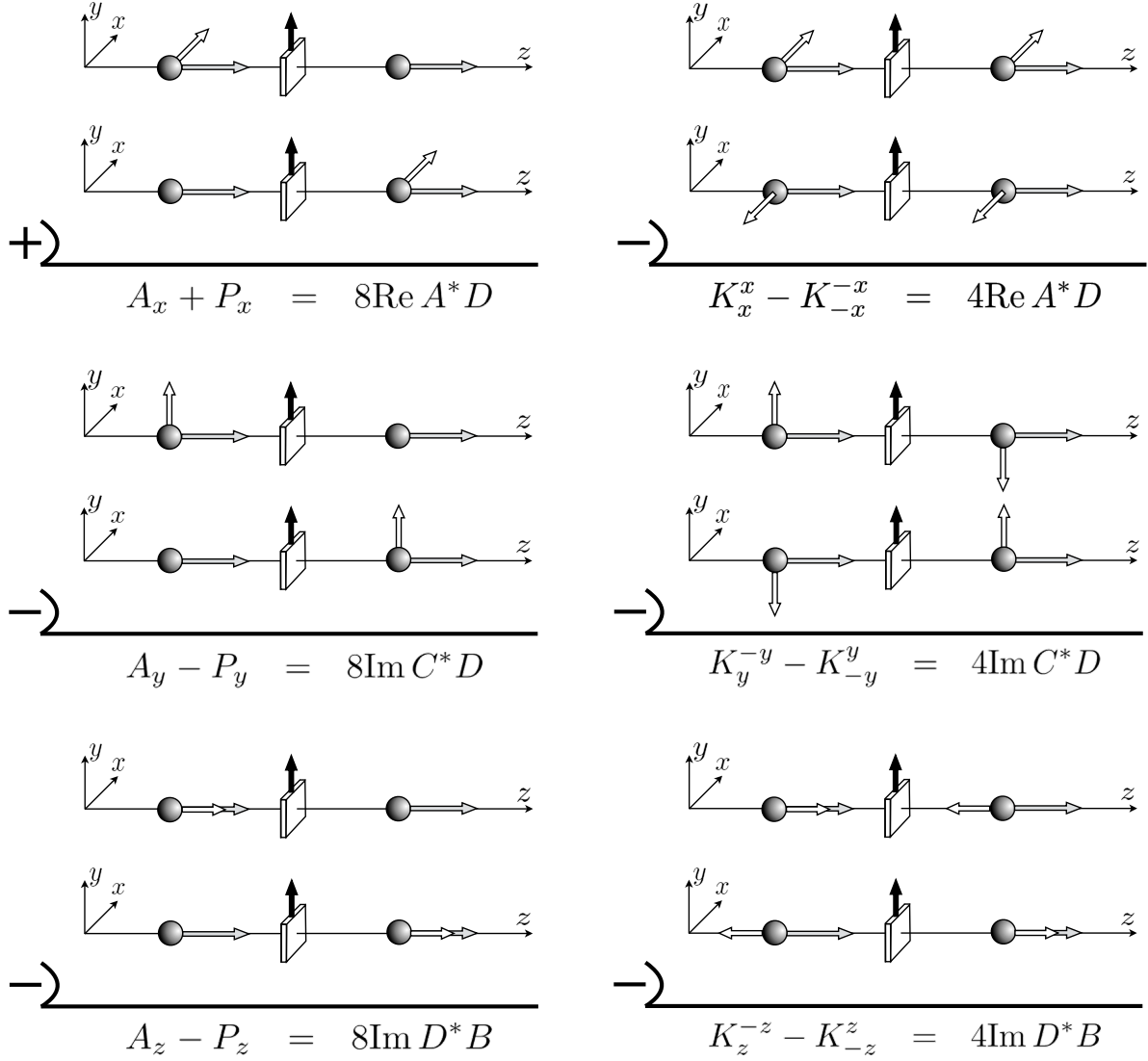


Figure 2.4: The combination of the observables to obtain the D term. The white, gray and black arrows denote the direction of the neutron spin, neutron momentum and target nuclear spin, respectively. $A_x + P_x$ gives us the largest measurement value.

2.4 The candidate nuclei for the T-violation search

First of all, it is necessary to find proper nuclei for the T-violation search. Needless to say, nuclei that have large $\Delta\sigma_T$ are better for the sensitive T-violation search. This means that nuclei that have large $\Delta\sigma_P$ and large $\kappa(J)$, which has not been measured in all nuclei, are advantageous. Additionally, lower resonance energy of the p-wave resonance is better in order to obtain high statistics as the intensity of a neutron beam from a typical neutron source increases in the lower energy region. The method for the nuclear polarization is also important. It has not been established for most of nuclei, and typically nuclei that have large spin are difficult to polarize due to the quadrupole coupling of the nuclear spin. Exceptionally, the polarization of ^{139}La , whose spin is $7/2$, has been studied well and high polarization was achieved.

The compound nuclei which have non-zero P-violation and less than 50 eV resonance energy are listed in Table 2.1 to select the realistic candidate nuclei. The target nuclei whose spin is zero are not listed because they cannot be polarized. Although any of these nuclei can in principle be a target nucleus for the T-violation search, possible candidate nuclei may be ^{139}La and ^{131}Xe , which are the nuclei whose P-violation is large, resonance energy is low, and polarization methods have been rather established. The detailed properties of these nuclei are explained as follows.

^{139}La

A very large P-violation of $9.8 \pm 0.2\%$ has been observed on the 0.758 eV p-wave resonance of ^{139}La , which is the lowest resonance energy among the nuclei which have the enhanced P-violation. The natural abundance is also large (99.911%). ^{139}La has a large nuclear spin of $7/2$. About 50% polarization has been achieved using a Neodymium doped LaAlO_3 crystal using the method of dynamic nuclear polarization in PSI [46]. In this experiment, a 2.35 T magnetic field was applied and the temperature of the sample was less than 0.3 K.

^{131}Xe

A large P-violation of $4.3 \pm 0.2\%$ has been observed on the 3.2 eV p-wave resonance of ^{131}Xe . There are nine isotopes of Xe, and the natural abundance of ^{131}Xe is 21.2%. The spin exchange optical pumping method can be used to polarize this nucleus [47]. However the spin relaxation time of ^{131}Xe is rather short compared to that of ^{129}Xe due to the quadrupole coupling of the $3/2$ nuclear spin of ^{131}Xe . Since the melting point is higher than that of nitrogen, it can be used as a solid nuclear target by using liquid nitrogen.

From this information, ^{139}La can be a good candidate nuclei. Hereafter we assume that a T-violation search experiment using ^{139}La is planned. The properties of the neutron absorption cross section of ^{139}La are described in next section.

In order to estimate the experimental sensitivity, $\kappa(J)$ needs to be determined by measuring ϕ , which can be obtained from the angular distribution of emitted γ -rays in $^{139}\text{La}(n,\gamma)$ reactions. The method to measure ϕ is discussed in next chapter.

	E_0 [eV]	A_L [%]	I	Abundance [%]	Polarization method
^{139}La	0.758	9.8 ± 0.2	7/2	99.911	DNP
^{81}Br	0.88	0.77 ± 0.33	3/2	49.31	-
^{117}Sn	1.33	0.79 ± 0.04	1/2	7.68	-
^{131}Xe	3.2	4.3 ± 0.2	3/2	21.2	SEOP
^{115}In	6.853	-1.45 ± 0.11	9/2	95.72	-
^{113}Cd	7.00	-0.80 ± 0.36	1/2	12.22	-
^{133}Cs	9.50	0.24 ± 0.02	7/2	100	-
^{115}In	13.46	0.61 ± 0.07	9/2	95.72	-
^{127}I	24.63	1.65 ± 0.16	5/2	100	-
^{115}In	29.68	0.44 ± 0.04	9/2	95.72	-
^{109}Ag	32.7	1.22 ± 0.02	1/2	48.16	-
^{117}Sn	34.04	-0.08 ± 0.02	1/2	7.68	-
^{107}Ag	35.84	-4.07 ± 0.38	1/2	51.84	-
^{115}In	40.68	-0.55 ± 0.04	9/2	95.72	-
^{103}Rh	44.47	2.33 ± 0.19	1/2	100	-

Table 2.1: The properties of the candidate nuclei for the T-violation search. The nuclei whose P-violation was observed with over 2σ , resonance energy is greater than 50 eV and target nuclei spin is non-zero are listed. The nuclear polarization method has not been established except for ^{139}La and ^{131}Xe .

2.5 Properties of the neutron absorption reaction of ^{139}La

Typical cross sections of ^{139}La with neutrons are shown in Fig 2.5. The reactions of ^{139}La with low energy neutrons are described by elastic scattering and absorption. The formalism of the neutron absorption reaction is summarized in Appendix A. The parameters of resonances in $^{139}\text{La}(n,\gamma)$ reactions whose

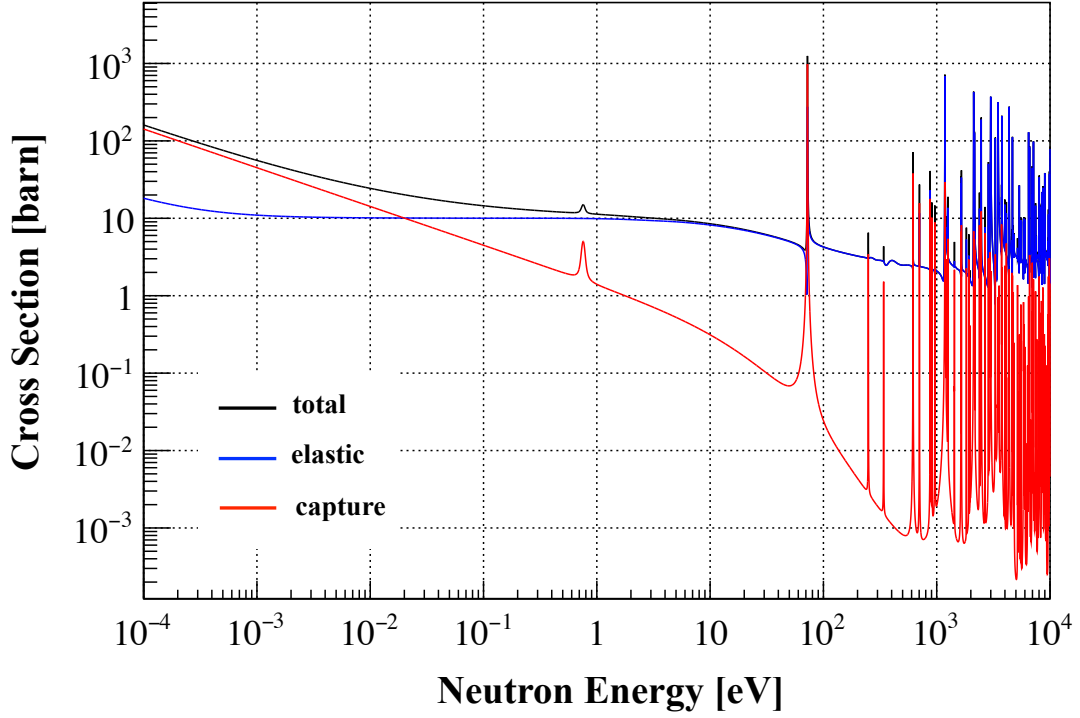


Figure 2.5: Cross sections of ^{139}La with neutron. The small peak at 0.75 eV is the p-wave resonance of the ^{139}La . The values of the cross sections were cited from Ref. [48]

resonance energy is less than 100 eV have been measured as shown in table 2.2. The $^{139}\text{La}+n$ state

r	E_r [eV]	J_r	l_r	Γ_r^γ [meV]	$g_r \Gamma_r^n$ [meV]	$g_r \Gamma_r^{nl_r}$ [meV]
1	$-48.63^{(a)}$	$4^{(a)}$	0	$62.2^{(a)}$		$82^{(a)}$
2	$0.758 \pm 0.001^{(b)}$		1	$40.11 \pm 1.94^{(c)}$	$(5.6 \pm 0.5) \times 10^{-5}^{(c)}$	
3	$72.30 \pm 0.05^{(b)}$		0	$75.64 \pm 2.21^{(c)}$	$11.76 \pm 0.53^{(c)}$	

Table 2.2: Resonance parameters of ^{139}La . (a) taken from Ref. [49]. (b) taken from Ref. [50]. (c) calculated from Refs. [51] and [50]. $g_r \Gamma_r^{nl_r}$ is the reduced neutron width.

decays to ^{140}La by γ -ray emission and the Q-value of this reaction is 5160.98 keV. The level scheme related to the $^{139}\text{La}(n,\gamma)^{140}\text{La}$ reaction is schematically shown in Fig. 2.6.

As shown in Table 2.2 and Fig. 2.5, there are large negative and positive s-wave resonances and a p-wave resonance located on the tails of these s-wave resonances. We assume the p-wave resonance interferes with the negative and/or positive s-wave resonance.

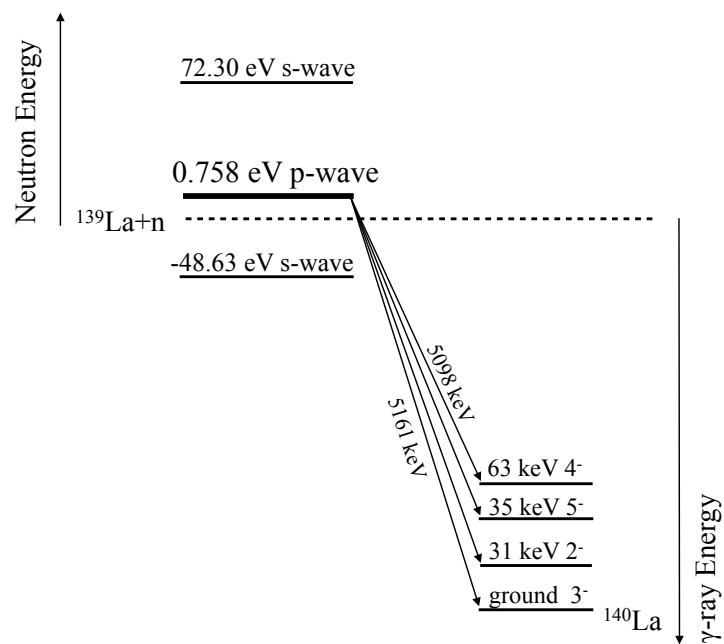


Figure 2.6: Transitions from $^{139}\text{La}+n$ to ^{140}La . ^{139}La has three neutron resonances in lower energy region, and the resonance state decays to the ^{140}La by emitting γ -rays.

Chapter 3

The angular distribution in (n,γ) reaction

As discussed in the previous section, $\kappa(J)$ needed to be determined in order to evaluate the T-violation sensitivity. In this section, the angular distribution of the (n,γ) reaction based on interference between s-wave resonances and p-wave resonances in order to measure ϕ , which is the parameter to decide $\kappa(J)$, is described.

3.1 The angular distributions in (n,γ) reactions

The amplitudes of the (n,γ) reaction can be described using Feynman diagrams as shown in Fig 3.1. The diagram 1 and 2 of Fig 3.1 correspond to the processes that a neutron is absorbed as an s-wave or a p-wave state as an entrance channel and a γ-ray is emitted from the same state as an exit channel. The diagram 3 and 4 of Fig 3.1 correspond to the processes that a neutron is absorbed as an s-wave or a p-wave state as an entrance channel, subsequently the states are mixed by the weak interaction, and a γ-ray is emitted from the different state as an exit channel. The amplitudes of these processes $V_1 - V_4$ are written as

$$\begin{aligned}
 V_1 &= - \sum_{r_s} \frac{1}{2k} \frac{\sqrt{g_{r_s} \Gamma_{r_s}^n \Gamma_{r_s f}^\gamma}}{E_n - E_{r_s} + i\Gamma_{r_s}/2}, \\
 V_2 &= - \sum_{r_p} \frac{1}{2k} \frac{\sqrt{g_{r_p} \Gamma_{r_p}^n \Gamma_{r_p f}^\gamma}}{E_n - E_{r_p} + i\Gamma_{r_p}/2}, \\
 V_3 &= - \sum_{r_s, r_p} \frac{1}{2k} \frac{\sqrt{g_{r_s} \Gamma_{r_s}^n} W \sqrt{\Gamma_{r_p f}^\gamma}}{(E_n - E_{r_p} + i\Gamma_{r_p}/2)(E_n - E_{r_s} + i\Gamma_{r_s}/2)}, \\
 V_4 &= - \sum_{r_s, r_p} \frac{1}{2k} \frac{\sqrt{g_{r_p} \Gamma_{r_p}^n} W \sqrt{\Gamma_{r_s f}^\gamma}}{(E_n - E_{r_s} + i\Gamma_{r_s}/2)(E_n - E_{r_p} + i\Gamma_{r_p}/2)},
 \end{aligned} \tag{3.1}$$

where k is the momentum of neutron, E_n is the kinetic energy of the neutron, Γ_r^n is the neutron width, Γ_{rf}^γ is the partial γ width to f -th final state, E_r is the resonance energy of the neutron resonance and W

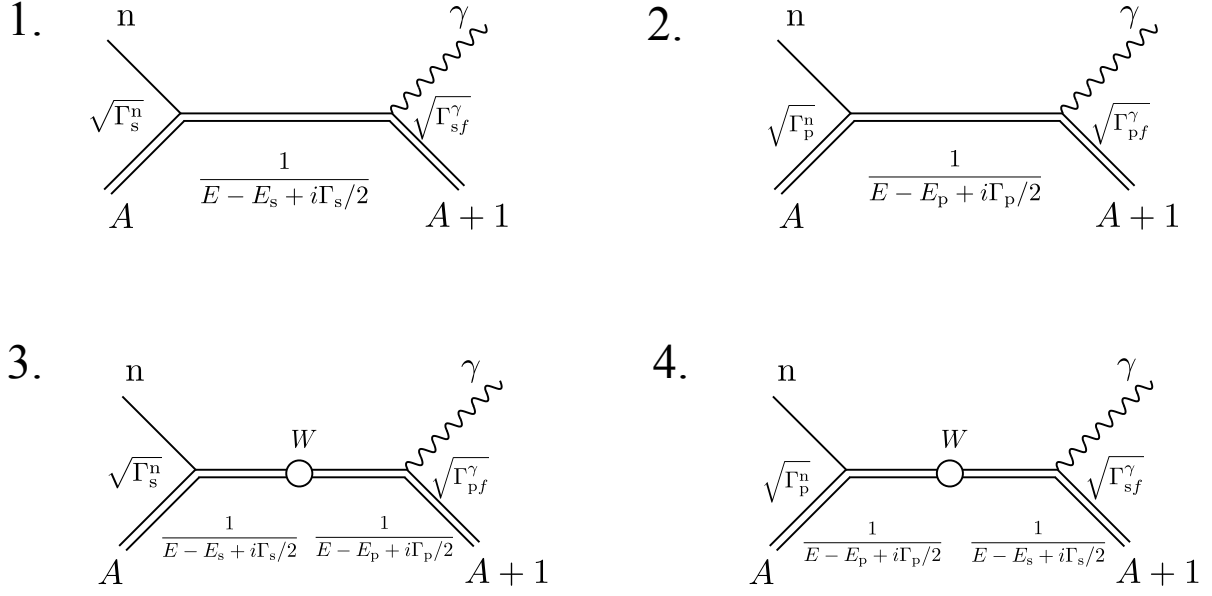


Figure 3.1: Feynman diagrams of amplitude of (n,γ) reactions through s-wave and p-wave state. The circle denotes the weak interaction.

is the weak matrix element. Here g_r is statistical weight factor and defined as

$$g_r = \frac{2J_r + 1}{2(2I + 1)}, \quad (3.2)$$

where J_r and I is the angular momentum of the compound status and spin of the target nucleus. When the interference between an s-wave and a p-wave amplitude is considered, $V_1 - V_4$ are given as follows.

$$\begin{aligned} V_1 &= -\frac{1}{2k} \frac{\sqrt{g_{r_s} \Gamma_{r_s}^n \Gamma_{r_{sf}}^\gamma} (1 + \alpha)}{E_n - E_{r_s} + i\Gamma_{r_s}/2}, \\ V_2 &= -\frac{1}{2k} \frac{\sqrt{g_{r_p} \Gamma_{r_p}^n \Gamma_{r_{pf}}^\gamma}}{E_n - E_{r_p} + i\Gamma_{r_p}/2}, \\ V_3 &= -\frac{1}{2k} \frac{\sqrt{g_{r_s} \Gamma_{r_s}^n} W \sqrt{\Gamma_{r_{pf}}^\gamma} (1 + \beta)}{(E_n - E_{r_p} + i\Gamma_{r_p}/2)(E_n - E_{r_s} + i\Gamma_{r_s}/2)}, \\ V_4 &= -\frac{1}{2k} \frac{\sqrt{g_{r_p} \Gamma_{r_p}^n} W \sqrt{\Gamma_{r_{sf}}^\gamma} (1 + \gamma)}{(E_n - E_{r_s} + i\Gamma_{r_s}/2)(E_n - E_{r_p} + i\Gamma_{r_p}/2)}. \end{aligned} \quad (3.3)$$

Here, the contributions of the other far s-wave resonances are taken into account as the correction term α , β and γ .

The differential cross section of the (n,γ) reaction induced by polarized and unpolarized neutrons can be

written as

$$\begin{aligned}
\frac{d\sigma_{n\gamma f}}{d\Omega_\gamma} = & \frac{1}{2} \left(a_0 + a_1 \hat{\mathbf{k}}_n \cdot \hat{\mathbf{k}}_\gamma + a_2 \boldsymbol{\sigma}_n \cdot (\hat{\mathbf{k}}_n \times \hat{\mathbf{k}}_\gamma) + a_3 \left((\hat{\mathbf{k}}_n \cdot \hat{\mathbf{k}}_\gamma)^2 - \frac{1}{3} \right) \right. \\
& + a_4 (\hat{\mathbf{k}}_n \cdot \hat{\mathbf{k}}_\gamma) (\boldsymbol{\sigma}_n \cdot (\hat{\mathbf{k}}_n \times \hat{\mathbf{k}}_\gamma)) + a_5 (\boldsymbol{\sigma}_\gamma \cdot \hat{\mathbf{k}}_\gamma) (\boldsymbol{\sigma}_n \cdot \hat{\mathbf{k}}_\gamma) \\
& + a_6 (\boldsymbol{\sigma}_\gamma \cdot \hat{\mathbf{k}}_\gamma) (\boldsymbol{\sigma}_n \cdot \hat{\mathbf{k}}_n) + a_7 (\boldsymbol{\sigma}_\gamma \cdot \hat{\mathbf{k}}_\gamma) \left((\boldsymbol{\sigma}_n \cdot \hat{\mathbf{k}}_\gamma) (\hat{\mathbf{k}}_\gamma \cdot \hat{\mathbf{k}}_n) - \frac{1}{3} \boldsymbol{\sigma}_n \cdot \hat{\mathbf{k}}_n \right) \\
& + a_8 (\boldsymbol{\sigma}_\gamma \cdot \hat{\mathbf{k}}_\gamma) \left((\boldsymbol{\sigma}_n \cdot \hat{\mathbf{k}}_n) (\hat{\mathbf{k}}_n \cdot \hat{\mathbf{k}}_\gamma) - \frac{1}{3} \boldsymbol{\sigma}_n \cdot \hat{\mathbf{k}}_\gamma \right) \\
& + a_9 \boldsymbol{\sigma}_n \cdot \hat{\mathbf{k}}_\gamma + a_{10} \boldsymbol{\sigma}_n \cdot \hat{\mathbf{k}}_n + a_{11} \left((\boldsymbol{\sigma}_n \cdot \hat{\mathbf{k}}_\gamma) (\hat{\mathbf{k}}_\gamma \cdot \hat{\mathbf{k}}_n) - \frac{1}{3} (\boldsymbol{\sigma}_n \cdot \hat{\mathbf{k}}_n) \right) \\
& + a_{12} (\boldsymbol{\sigma}_n \cdot \hat{\mathbf{k}}_n) \left((\hat{\mathbf{k}}_n \cdot \hat{\mathbf{k}}_\gamma) - \frac{1}{3} (\boldsymbol{\sigma}_n \cdot \hat{\mathbf{k}}_\gamma) \right) \\
& + a_{13} \boldsymbol{\sigma}_\gamma \cdot \hat{\mathbf{k}}_\gamma + a_{14} (\boldsymbol{\sigma}_\gamma \cdot \hat{\mathbf{k}}_\gamma) (\hat{\mathbf{k}}_n \cdot \hat{\mathbf{k}}_\gamma) \\
& + a_{15} (\boldsymbol{\sigma}_\gamma \cdot \hat{\mathbf{k}}_\gamma) \boldsymbol{\sigma}_n \cdot (\hat{\mathbf{k}}_n \times \hat{\mathbf{k}}_\gamma) + a_{16} (\boldsymbol{\sigma}_\gamma \cdot \hat{\mathbf{k}}_\gamma) \left((\hat{\mathbf{k}}_n \cdot \hat{\mathbf{k}}_\gamma)^2 - \frac{1}{3} \right) \\
& \left. + a_{17} (\boldsymbol{\sigma}_\gamma \cdot \hat{\mathbf{k}}_\gamma) (\hat{\mathbf{k}}_n \cdot \hat{\mathbf{k}}_\gamma) (\boldsymbol{\sigma}_n \cdot (\hat{\mathbf{k}}_n \times \hat{\mathbf{k}}_\gamma)) \right), \tag{3.4}
\end{aligned}$$

where \mathbf{k}_n is a unit vector parallel to the incident neutron momentum, \mathbf{k}_γ is a unit vector parallel to the emitted γ -ray momentum, $\boldsymbol{\sigma}_n$ is a unit vector parallel to the incident neutron spin and $\boldsymbol{\sigma}_\gamma$ is a unit vector parallel to the emitted γ -ray spin. Expressions of the coefficients a_0 - a_{17} are given by the products of amplitudes $V_1 - V_4$ as

$$\begin{aligned}
a_0 &= \sum_{r_s} |V_{1r_s}|^2 + \sum_{r_p} |V_{2r_p}|^2, \\
a_1 &= 2 \operatorname{Re} \sum_{r_s r_p j} V_{1r_s} V_{2r_p}^* P(J_{r_s} J_{r_p} \frac{1}{2} j 1 I F) z_{r_p j}, \\
a_2 &= -2 \operatorname{Im} \sum_{r_s r_p j} V_{1r_s} V_{2r_p}^* \beta_j P(J_{r_s} J_{r_p} \frac{1}{2} j 1 I F) z_{r_p j}, \\
a_3 &= 3\sqrt{10} \operatorname{Re} \sum_{r_p j r'_p j'} V_{2r_p} V_{2r'_p}^* P(J_{r_p} J_{r'_p} j j' 2 I F) \begin{Bmatrix} 2 & 1 & 1 \\ 0 & \frac{1}{2} & \frac{1}{2} \\ 2 & j & j' \end{Bmatrix} z_{r_p j} z_{r_p j'}, \\
a_4 &= -6\sqrt{5} \operatorname{Im} \sum_{r_p j r'_p j'} V_{2r_p} V_{2r'_p}^* P(J_{r_p} J_{r'_p} j j' 2 I F) \begin{Bmatrix} 2 & 1 & 1 \\ 1 & \frac{1}{2} & \frac{1}{2} \\ 2 & j & j' \end{Bmatrix} z_{r_p j} z_{r_p j'},
\end{aligned}$$

$$\begin{aligned}
a_5 &= -\text{Re} \sum_{r_s r'_s} V_{1r_s} V_{1r'_s}^* P(J_{r_s} J_{r'_s} \frac{1}{2} \frac{1}{2} 1IF) \\
&\quad - 6\text{Re} \sum_{r_p j r'_p j'} V_{2r_p} V_{2r'_p}^* P(J_{r_p} J_{r'_p} j j' 1IF) \begin{Bmatrix} 0 & 1 & 1 \\ 1 & \frac{1}{2} & \frac{1}{2} \\ 1 & j & j' \end{Bmatrix} z_{r_p j} z_{r_p j'}, \\
a_6 &= -2 \text{Re} \sum_{r_s} V_{1r_s} V_{2r_p}^* \delta_{J_{r_s} J_{r_p}} z_{r_p \frac{1}{2}}, \\
a_7 &= \sqrt{3} \text{Re} \sum_{r_s i_p j} V_{1r_s} V_{2r_p}^* P(J_{r_s} J_{r_p} \frac{1}{2} \frac{3}{2} 2IF) z_{r_p \frac{3}{2}}, \\
a_8 &= -18 \text{Re} \sum_{r_p j r'_p j'} V_{2r_p} V_{2r'_p}^* P(J_{r_p} J_{r'_p} j j' 1IF) \begin{Bmatrix} 2 & 1 & 1 \\ 1 & \frac{1}{2} & \frac{1}{2} \\ 2 & j & j' \end{Bmatrix} z_{r_p j} z_{r_p j'}, \\
a_9 &= -2 \text{Re} \sum_{r_s r'_s j} V_{1r_s} V_{3r'_s}^* P(J_{r_s} J_{r'_s} \frac{1}{2} \frac{1}{2} 1IF) \\
&\quad - 12 \text{Re} \sum_{r_p j r'_p j'} V_{2r_p} V_{4r'_p}^* P(J_{r_p} J_{r'_p} j j' 1IF) \begin{Bmatrix} 0 & 1 & 1 \\ 1 & \frac{1}{2} & \frac{1}{2} \\ 1 & j & j' \end{Bmatrix} z_{r_p j} z_{r_p j'}, \\
a_{10} &= -2 \text{Re} \sum_{r_s} [V_{2r_p} V_{3r_s}^* + V_{1r_s} V_{4r_p}^*] \delta_{J_{r_s} J_{r_p}} z_{r_p \frac{1}{2}}, \\
a_{11} &= \sqrt{3} \text{Re} \sum_{r_s r_p} [V_{2r_p} V_{3r_s}^* + V_{1r_s} V_{4r_p}^*] P(J_{r_s} J_{r_p} \frac{1}{2} \frac{3}{2} 2IF) z_{r_p \frac{3}{2}}, \\
a_{12} &= -36 \text{Im} \sum_{r_s i_p j} V_{2r_p} V_{4r_p}^* P(J_{r_p} J_{r_p} j j' 1IF) \begin{Bmatrix} 2 & 1 & 1 \\ 1 & \frac{1}{2} & \frac{1}{2} \\ 1 & j & j' \end{Bmatrix} z_{r_p j} z_{r_p j'}, \\
a_{13} &= 2 \text{Re} \sum_{r_s} V_{1r_s} V_{3r_s}^* + 2 \text{Re} \sum_{r_p} V_{2r_p} V_{4r_p}^*, \\
a_{14} &= 2 \text{Re} \sum_{r_s r_p j} [V_{2r_p} V_{3r_s}^* + V_{1r_s} V_{4r_p}^*] P(J_{r_s} J_{r_p} \frac{1}{2} j 1IF) z_{r_p j}, \\
a_{15} &= 2 \text{Im} \sum_{r_s r_p j} [V_{2r_p} V_{3r_s}^* - V_{1r_s} V_{4r_p}^*] P(J_{r_s} J_{r_p} \frac{1}{2} j 1IF) z_{r_p j}, \\
a_{16} &= 6\sqrt{10} \text{Re} \sum_{r_p j r'_p j'} V_{2r_p} V_{4r'_p}^* P(J_{r_p} J_{r'_p} j j' 2IF) \begin{Bmatrix} 2 & 1 & 1 \\ 0 & \frac{1}{2} & \frac{1}{2} \\ 2 & j & j' \end{Bmatrix} z_{r_p j} z_{r_p j'}, \\
a_{17} &= -12\sqrt{5} \text{Im} \sum_{r_p j r'_p j'} V_{2r_p} V_{4r'_p}^* P(J_{r_p} J_{r'_p} j j' 2IF) \begin{Bmatrix} 2 & 1 & 1 \\ 1 & \frac{1}{2} & \frac{1}{2} \\ 2 & j & j' \end{Bmatrix} z_{r_p j} z_{r_p j'}, \tag{3.5}
\end{aligned}$$

where

$$P(JJ'jjkIF) = (-1)^{J+J'+j'+I+F} \frac{3}{2} \sqrt{(2J+1)(2J'+1)(2j+1)(2J'+1)} \\ \times \left\{ \begin{matrix} k & j & j' \\ I & J' & J \end{matrix} \right\} \left\{ \begin{matrix} k & 1 & 1 \\ F & J & J' \end{matrix} \right\}, \quad (3.6)$$

$$\beta_j = \begin{cases} 1 & (j = \frac{1}{2}) \\ -\frac{1}{2} & (j = \frac{3}{2}) \end{cases}, \quad (3.7)$$

where J , j , I and F are the spin of the compound state, total angular momentum of the neutron, spin of the target nucleus and spin of the final state, respectively. The ratios of partial neutron widths to neutron widths of p-wave resonances are given as

$$z_{r_p j} = \begin{cases} x_{r_p} = \sqrt{\frac{\Gamma_{p,j=\frac{1}{2}}^n}{\Gamma_p^n}} & (j = \frac{1}{2}) \\ y_{r_p} = \sqrt{\frac{\Gamma_{p,j=\frac{3}{2}}^n}{\Gamma_p^n}} & (j = \frac{3}{2}) \end{cases}. \quad (3.8)$$

The a_0 term denotes the typical cross section of the neutron resonance described with the Breit-Wigner functions. The a_{10} term corresponds to the helicity dependence of the neutron absorption cross section, and A_L in Eq. 2.7 is derived from a_{10} in Eq. 3.5. The ratio of the P-violating cross section a_{10} to the p-wave cross section $a_{0p} = |V_{2rp}|^2$ is given as

$$\frac{a_{10}}{a_{0p}} = \frac{-2xW}{(E_n - E_s)^2 + \frac{\Gamma_s^2}{4}} \sqrt{\frac{\Gamma_s^n}{\Gamma_p^n}} \left((E_n - E_s) + \frac{\Gamma_s^\gamma}{\Gamma_p^\gamma} (E_n - E_p) \right). \quad (3.9)$$

Since $E_s - E_p \gg \Gamma_s$ when the s-wave resonance is far from the p-wave resonance, Eq. 3.10 at $E_n = E_p$ can be written as

$$\frac{a_{10}}{a_{0p}} \simeq -\frac{2xW}{E_p - E_s} \sqrt{\frac{\Gamma_s^n}{\Gamma_p^n}} = A_L. \quad (3.10)$$

3.2 The angular distributions in (n, γ) reactions for unpolarized neutrons

Hereinafter we assume that the γ -ray polarization is not measured and the incident neutrons are not polarized. In this case the differential cross section is written as

$$\frac{d\sigma_{n\gamma_f}}{d\Omega_\gamma} = \frac{1}{2} \left(a_0 + a_1 \cos \theta_\gamma + a_3 \left(\cos^2 \theta_\gamma - \frac{1}{3} \right) \right), \quad (3.11)$$

where θ_γ is the polar angle of the emitted γ -ray with respected to incident neutron momentum.

A value of ϕ can be extracted from a_1 and a_3 since these are both functions of x and y . The coefficients can be decomposed as a sum of terms containing x^2 , xy and y^2 or x and y as

$$\begin{aligned} a_1 &= a_{1x}x + a_{1y}y, \\ a_3 &= a_{3xy}xy + a_{3yy}y^2, \end{aligned} \quad (3.12)$$

where

$$\begin{aligned} a_{1x} &= 2 \operatorname{Re} \sum_{r_s r_p} V_{1r_s} V_{2r_p}^* P(J_{r_s} J_{r_p} \frac{1}{2} \frac{1}{2} 1IF), \\ a_{1y} &= 2 \operatorname{Re} \sum_{r_s r_p} V_{1r_s} V_{2r_p}^* P(J_{r_s} J_{r_p} \frac{1}{2} \frac{3}{2} 1IF), \\ a_{3xy} &= 3\sqrt{10} \operatorname{Re} \sum_{r_p r'_p} V_{2r_p} V_{2r'_p}^* P(J_{r_p} J_{r'_p} \frac{1}{2} \frac{3}{2} 2IF) \begin{Bmatrix} 2 & 1 & 1 \\ 0 & \frac{1}{2} & \frac{1}{2} \\ 2 & \frac{1}{2} & \frac{3}{2} \end{Bmatrix}, \\ a_{3yy} &= 3\sqrt{10} \operatorname{Re} \sum_{r_p r'_p} V_{2r_p} V_{2r'_p}^* P(J_{r_p} J_{r'_p} \frac{3}{2} \frac{3}{2} 2IF) \begin{Bmatrix} 2 & 1 & 1 \\ 0 & \frac{1}{2} & \frac{1}{2} \\ 2 & \frac{3}{2} & \frac{3}{2} \end{Bmatrix}. \end{aligned} \quad (3.13)$$

The coefficients a_{3xx} is not written in the above equations since the P coefficient is identically zero. As a_1 and a_3 are coefficients of the angular dependent term as shown in Eq 3.11, these can be obtained by measuring the angular distribution of individual γ -rays from the p-wave resonance as long as both the spin of the compound state (J) and the spin of the final state (F) are known.

As an example, neutron energy dependences of a_0 , a_{1x} , a_{1y} , a_{3xy} and a_{3yy} in the case of a p-wave resonance of the $^{139}\text{La}(n,\gamma)$ reaction for $F = 3$ assuming $J_1 = 4$, $J_2 = 4$ and $J_3 = 3$ are shown in Fig 3.2 using the resonance parameters of Table 2.2. As shown in Fig 3.2, the shape of the a_0 , which is described as a Breit-Wigner function, will be distorted due to the asymmetric shape of a_1 at an angle which is $\cos \theta_\gamma \neq 0$. The asymmetry of the a_1 and the height of the a_3 vary with the value of the ϕ , and therefore we should perform an experiment to measure the peak shape of the p-wave resonance gated with certain γ -rays at several angles in order to extract a value of ϕ .

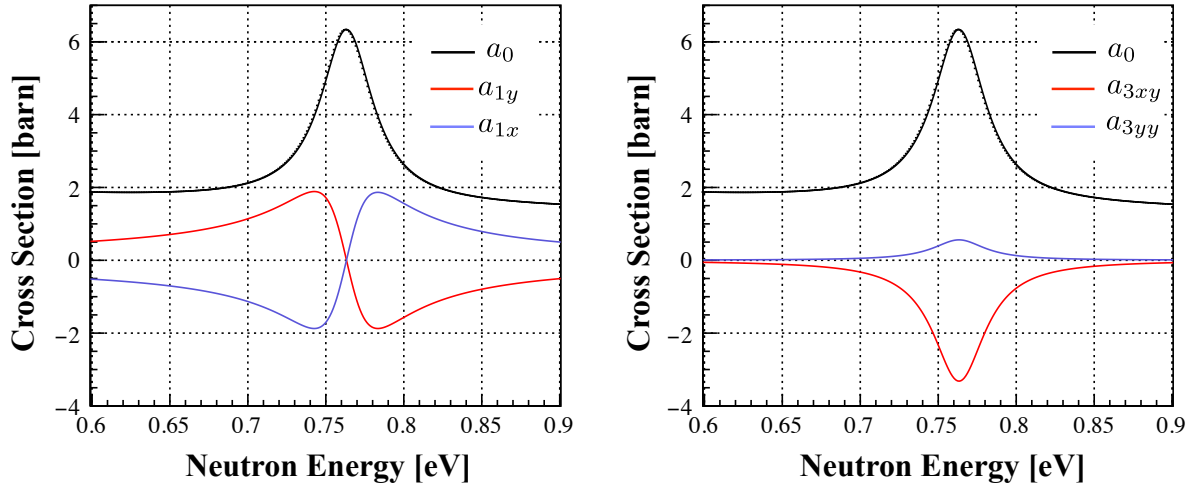


Figure 3.2: Neutron energy dependences of a_0 , a_{1x} , a_{1y} , a_{3xy} and a_{3yy} in $^{139}\text{La}(n,\gamma)$ reactions to the $F = 3$ final state in the case of $J_2 = 4$ and $J_3 = 3$ using the resonance parameters in Table 2.2. The a_0 is described by Breit-Wigner function. The a_1 and a_3 has a symmetric and an asymmetric shape at the peak of the p-wave resonance.

Chapter 4

Facilities and experimental setup

As shown in previous section, the T-violation sensitivity can be evaluated by measuring the angular dependence of γ -rays from a neutron induced compound nucleus. To perform this measurement, a high intensity neutron beam and a high resolution γ -ray detector is needed. These measurement were carried out at beamline 04 ANNRI (Accurate Neutron-Nucleus Reaction measurement Instrument) of the Material and Life science experimental Facility (MLF) of the Japan Proton Accelerator Research Complex (J-PARC). The facilities and the experimental setup are described in this section.

4.1 Facility for the neutron beam

J-PARC is a high-intensity proton accelerator facility in Tokai, Ibaraki, Japan. A bird's-eye view of the facilities of J-PARC is shown in Fig 4.1. In J-PARC, there are three accelerators: a linear accelerator (LINAC), a 3GeV Rapid Cycle Synchrotron (RCS), and a Main Ring (MR). The pulsed proton beam from those accelerators are injected to the three facilities: the Material and Life science experimental facility, the Neutrino facility, and the Hadron Experimental facility (Hadron-hall), and are used for various applications.

MLF is a facility for the materials and life science using the intense pulsed neutron and muon beams. The neutrons are generated in nuclear separation reactions in a liquid mercury target by using a 3 GeV proton beam. The high energy neutrons generated from the mercury target are moderated by a light water moderator and a hydrogen moderator at 20 K and 1.5 MPa flow, and guided to 23 neutron beam ports of MLF. The energy range of the neutron beam is from cold to epithermal energies. There are three types of moderators: a coupled moderator, a decoupled moderator and a poisoned moderator. The coupled moderator provides the most intense neutron beam among the moderators and is used for the experiment in this thesis. The characteristics of the moderators are summarized in Table 4.2.

The primary proton beams were supplied at a repetition rate of 25Hz and in single-bunch mode, which in which the pulsed protons consist of a bunches of 100 ns. During typical operation, double-bunch mode, in which the pulsed protons consist of two bunches of 100 ns width on intervals of 600 ns, is used. An advantage of this mode of operation is that the neutron beam intensity increases in the



Figure 4.1: A bird's view of the J-PARC accelerators [52].

Type of moderator	number of beam ports	Time-integrated thermal neutron flux [$\text{n/s}\cdot\text{cm}^2$]	Peak neutron flux at 10 meV [$\text{n/eV}\cdot\text{s}\cdot\text{cm}^2$]	Pulse width in FWHM at 10 meV [μs]
Coupled	11	4.6×10^8	6.0×10^{12}	92
Decoupled	6	0.95×10^8	3.0×10^{12}	33
Poisoned (thicker side)	3	0.65×10^8	2.4×10^{12}	22
Poisoned (thin side)	3	0.38×10^8	1.4×10^{12}	14

Table 4.1: Design characteristics of the moderators at 10 m from the moderator surface at 1 MW of beam power at J-PARC [53].

thermal and cold energy regions where the structure of the double bunch pulse is negligible due to the moderation process. However, double-bunch mode makes the time resolution of the neutron beam worse in epi-thermal region. Therefore, single-bunch mode is better for the experiments where high time resolution of the neutron beam is important such as measurements of neutron absorption cross sections. The average proton beam power generating spallation neutrons is 150 kW during the measurement.

Parameter	Value
Designed beam power	1 MW
Operated beam power	150 kW
Extraction energy	3 GeV
Repetition rate	25 Hz
Bunch width of the proton beam (single bunch)	100 ns

Table 4.2: Parameters of RCS [53].

4.2 Beam Line 04 at MLF

The schematics of the ANNRI installed in beam line 04 (BL04) is shown in Fig. 4.2. The z -axis is defined in the beam direction, the y -axis is the vertical upward axis, and the x -axis is perpendicular to them, thus x , y and z forms a right-handed frame.

The germanium detector assembly, a sodium iodide (NaI) scintillator detector and lithium-6 and -7 glass scintillators can be used at ANNRI on beam line 04. The angular distribution of the γ -ray was measured by using the germanium detector assembly. The nuclear target was placed at the center of the detector assembly and the length from the moderator surface to the target was 21.5 m. The neutron beam from the moderator goes through the T_0 -chopper, the neutron filters, double disk chopper and the rotary collimator, which were used for the adjustment of the experimental conditions, and is stopped by a beam stopper made from iron. The material of the neutron filter can be selected from manganese, cobalt, aluminum, silver, indium, lead, and cadmium. Since the energy dependences of the neutron absorption cross section in each nucleus are different, these filters are used to suppress the neutron beam in unnecessary energy regions. The lead filter is mainly used to suppress the γ -ray background from the upper stream. In our measurement, only the lead filter (thickness: 37.5 mm) was used. The T_0 -chopper was a semi-circular plate whose surface was painted by 95 wt% isotopically enriched boron carbide. It was operated synchronously with the proton injection to suppress the slow neutron (less than 3 meV) to avoid frame overlap.

Five collimators between the moderator and the germanium detector assembly were installed. The sizes of collimator holes become smaller as the collimators become closer to the germanium detector assembly. The collimator consisted of an upper-stream collimator and down-stream collimator and were used for the adjustment of the intensity and the size of the neutron beam. The collimator closing to the germanium detector assembly decides the spatial distribution of the neutron beam [54]. This collimator is called "rotary collimator" and the hole size can be selected from 4 sizes of 6 mm, 7 mm, 15 mm and 22 mm. The collimator of 22 mm size was primarily used in our experiments.

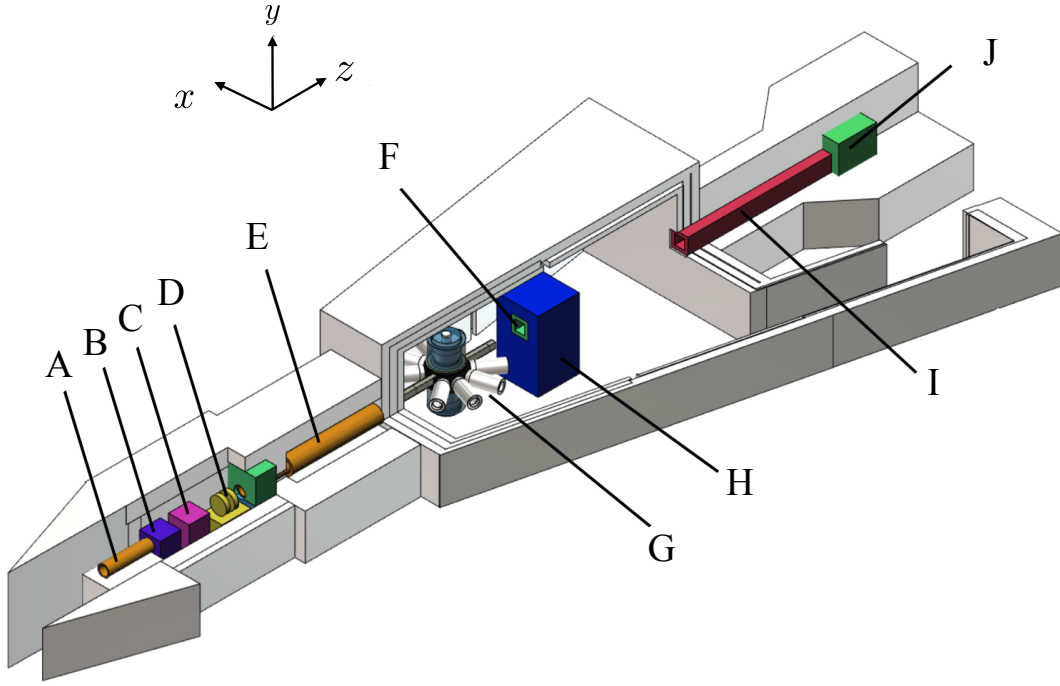


Figure 4.2: Schematic of the ANNRI installed at the beamline 04 of J-PARC/MLF. (A) Collimator, (B) T_0 -chopper, (C) Neutron filter, (D) Disk chopper, (E) Collimator, (F) Iron, (G) Germanium detector assembly, (H) Concrete, (I) Boron resin, and (J) Beam stopper (Iron).

4.2.1 Spatial distribution of the neutron beam

The spatial distributions of the neutron beam at ANNRI were measured by K.Kino et al [54]. They measured the spatial distribution of the neutron beam by putting a position sensitive Li-glass scintillation detector at a 21.5 m sample position. The detector has 256 Li-6 enriched glass scintillator pixels of size $2.1 \times 2.1 \text{ mm}^2$ and thickness of 1mm. The scintillation light generated from ${}^6\text{Li} + n \rightarrow \alpha + t$ reaction in the scintillators are detected by a position sensitive photo-multiplier tube. Since position and TOF are measured simultaneously, a TOF versus position intensity plot can be obtained. Figure 4.3 shows the measured spatial distributions for the 22 mm-diameter beam.

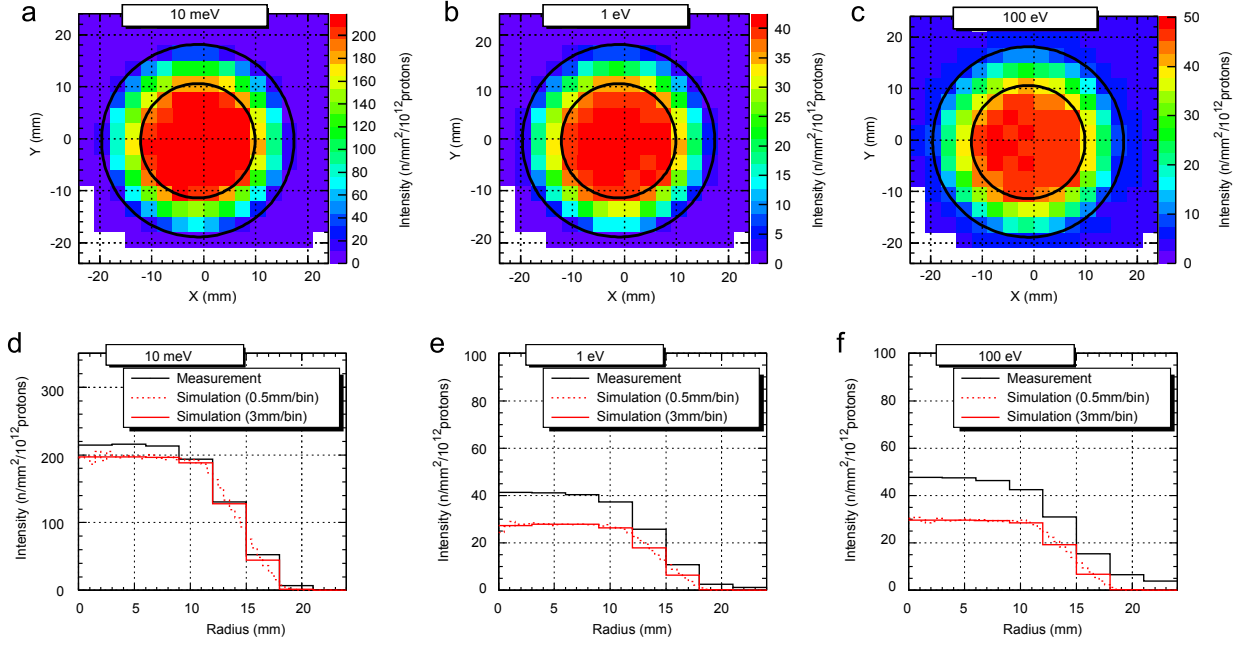


Figure 4.3: Spatial distributions of the neutron beam in ANNRI for 22 mm-diameter beam [54].

4.2.2 Energy resolution of the neutron beam

The neutron energy is calculated from the time of flight from the moderator to the nuclear target. However the pulsed neutron beam has a time structure and it makes the energy resolution of the neutron beam worse. One origin of the time structure is moderation process of the neutrons in the moderator. Another is the time structure of the incident proton beam to the mercury target. The time structure can be negligible in thermal and cold energy regions. However it cannot be ignored in the epithermal region which is used for the measurement of the neutron resonances. In our experiment, the evaluation of the time structure is important to measure a_1 and a_3 in Fig. 6.3 accurately.

Some functions to describe the pulse structure of the neutron beam were proposed. Typically, Ikeda-Carpenter function [55], Cole-Windsor function [56], Günsing function [57, 58], Gauss function [59, 60] and so on are used, and we need to select the function that can reproduce the pulse structure for each moderator. The pulse structure of the neutron beam at beam line 04 was evaluated by K.Kino et al [54]. They adopted Ikeda-Carpenter function to reproduce the pulse structure of beam line 04 and the double differential of the flux of the pulsed neutron beam I_n can be described as a function of E_n and the time measured from the primary proton beam injection t as

$$\frac{\partial^2 I_n}{\partial E_n \partial t}(E_n, t) = \frac{\alpha C}{2} \left\{ (1 - R)(\alpha t)^2 e^{-\alpha t} + 2R \frac{\alpha^2 \beta}{(\alpha - \beta)^3} \right. \\ \left. \times \left[e^{-\beta t} - e^{-\alpha t} \left(1 + (\alpha - \beta)t + \frac{(\alpha - \beta)^2}{2} t^2 \right) \right] \right\}, \quad (4.1)$$

where parameters α , β , C , R depend on E_n . The Ikeda–Carpenter function was originally proposed by S. Ikeda and J. M Carpenter to describe the pulse structure of the neutron beam from the polyethylene moderator in room temperature at the Intense Pulsed Neutron Source of the Argonne National Laboratory [55]. The double differential of the neutron beam flux on the moderator surface of the J-PARC spallation source was calculated using MCNPX [61], and was fitted with the Ikeda–Carpenter function. The examples of the simulated time structure and fitting result from the Ikeda–Carpenter function are shown in Fig 4.4.

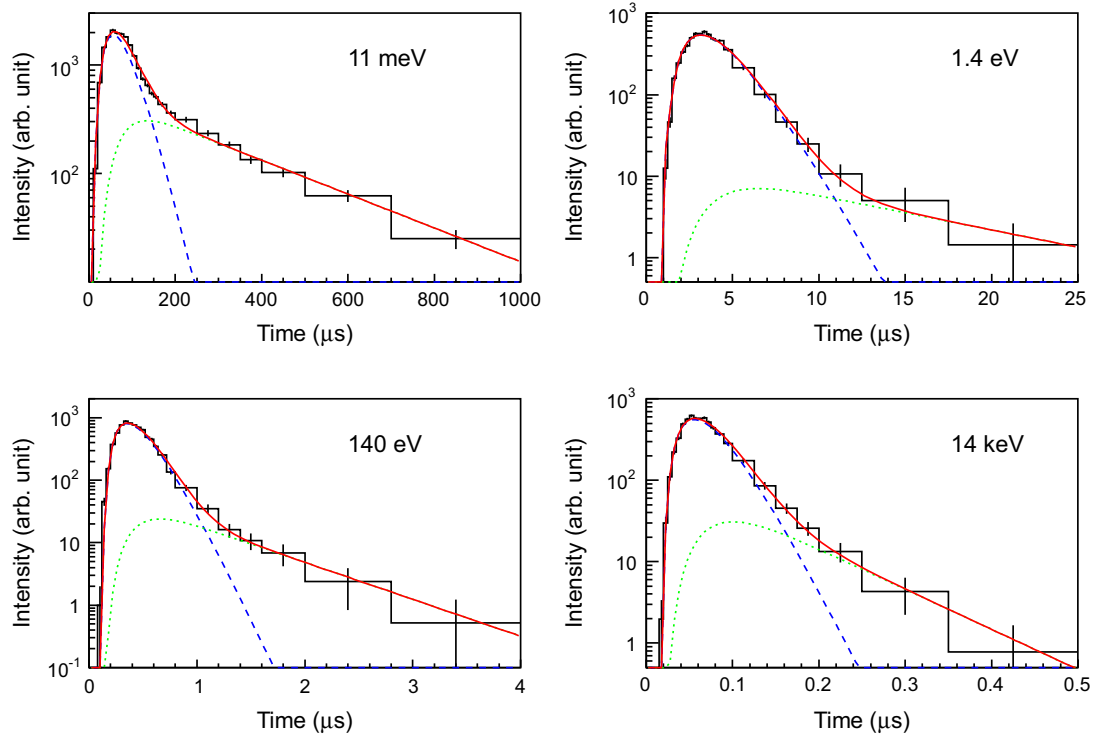


Figure 4.4: Examples of the simulated time structure of the neutron beam and fitting results [54].

The dependence of neutron energy on the fitting parameters t_0 , α , β , R , and C were obtained by fitting the pulse shape of neutron beam with a polynomial function[54] as shown in Fig 4.5. The neutron energy dependence of the FWHM of the time structure is shown in Fig 4.6, and the simulated results are confirmed by comparing with experimental results. In the thermal region, the time structure can be obtained by measuring Bragg's peaks. When the neutron beam goes through a crystal, only neutrons that satisfy Bragg's law are scattered. Since the scattered neutrons have the same energy, the time structure of the neutron beam can be obtained from the time structures of the Bragg's peaks. A mica target with dimensions of $50 \times 50 \text{ mm}^2$ and a thickness of 5 mm were used in their measurement. In the epithermal region, the time structure can be obtained from the neutron resonances. Since the resonance width of the neutron capture reaction is broadened by the time structure of the neutron beam, the times structures can be evaluated by measuring the width of well known neutron resonances. Tantalum foils were used in their measurements.

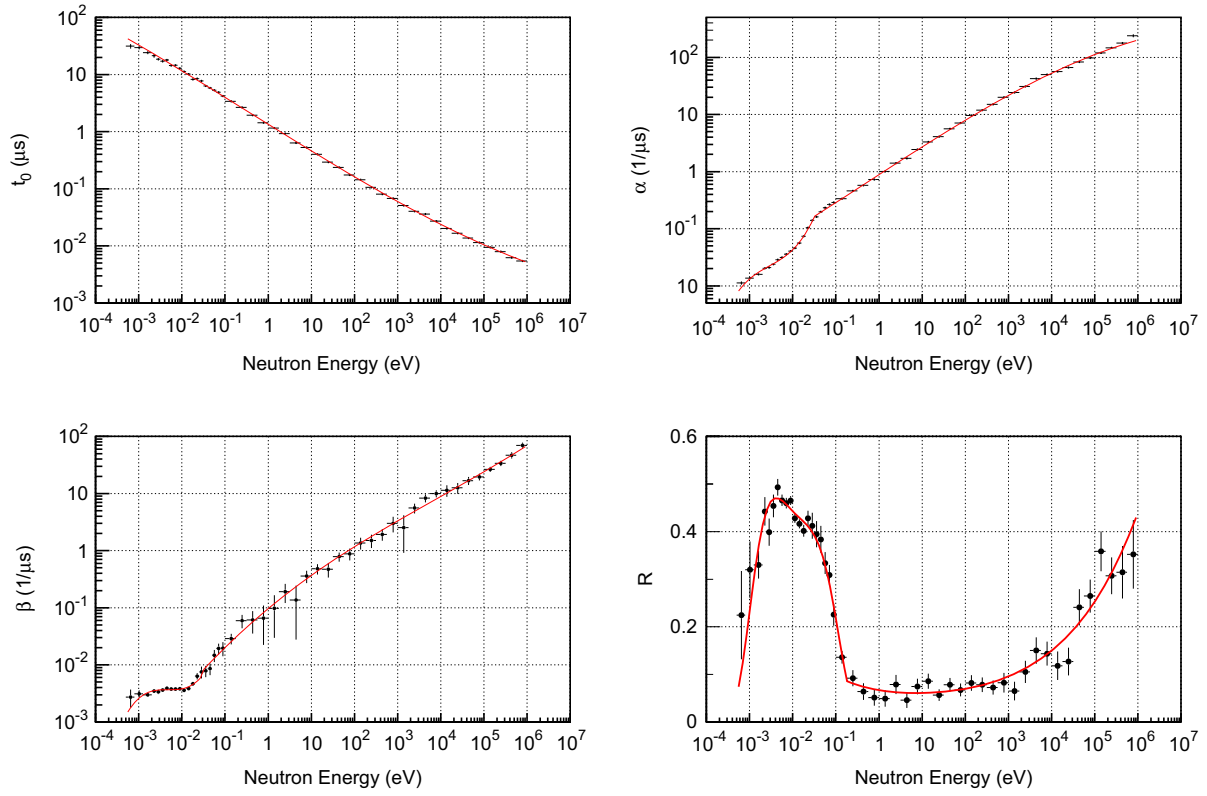
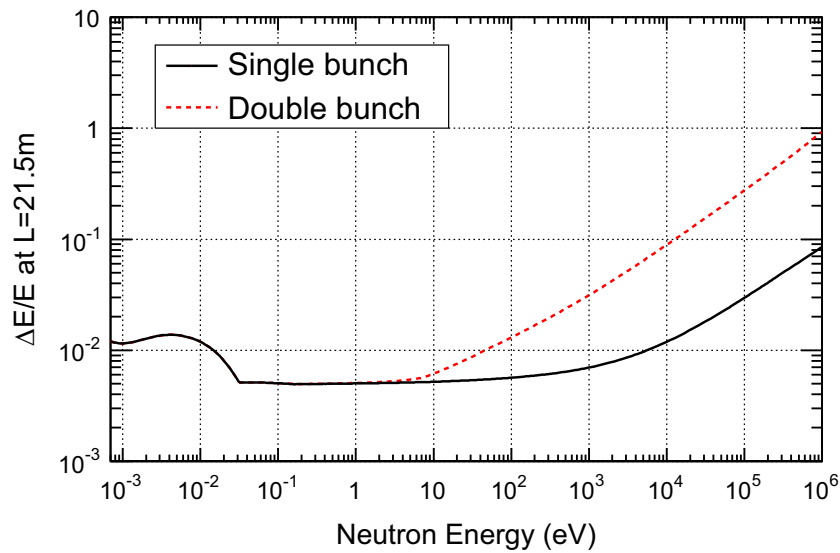
Figure 4.5: Energy dependence of α , β , C and R in Ikeda-Carpenter function [54].

Figure 4.6: Energy resolution of the neutron beam at ANNRI [54].

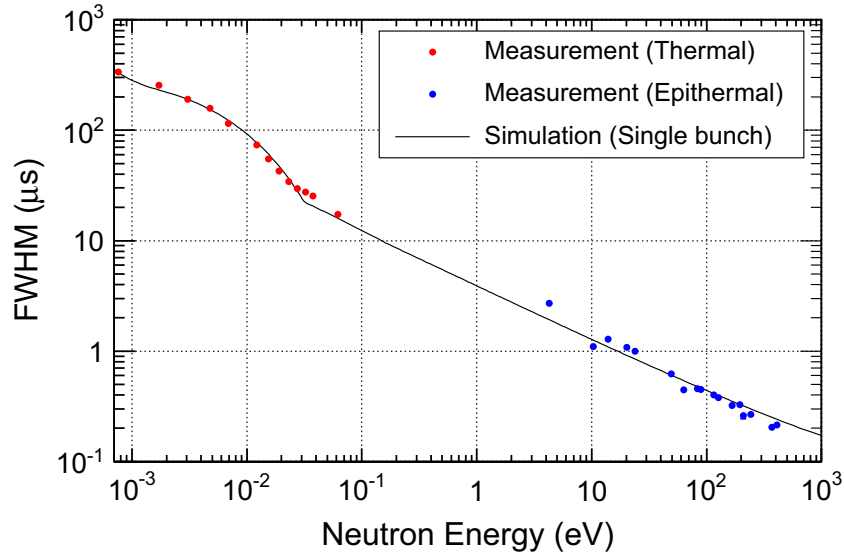


Figure 4.7: The simulation and measured value of the energy resolution of the neutron beam at ANNRI [54].

4.3 Germanium detector assembly

The germanium spectrometer at ANNRI is a γ -ray detector assembly which has high resolution and large solid angle. It was originally developed to measure neutron absorption cross sections of minor actinides and long-lived-fission products with the time of flight (TOF) method. The configuration of the germanium detector assembly is shown in Fig. 4.8. A coordinate system defines the beam axis as z -axis, the vertical direction as y -axis and the x -axis is such that they form a right-handed coordinate system. The origin was taken as the center of the nuclear target. The polar angle in spherical coordinates is denoted by θ and the azimuthal angle as ϕ .

The assembly consisted of two types of detector units: Type-A (Fig. 4.9) and Type-B (Fig. 4.10). Two combinations of seven Type-A detectors were placed above and below the target. The shape of the Type-A detector is hexagonal to enable clustering as shown in (Fig. 4.9). Germanium crystals are protected by neutron shields against damages resulting from scattered neutrons; shield-1 and shield-3 are made from LiH with a thickness of 22.3 mm and 17.3 mm, respectively. Shield-2 is made from LiF and the thickness is 5 mm. Lead plates are placed between shield-2 and shield-3 in order to eliminate low energy γ -rays, which were not used in our experiment. The crystal surfaces facing the target were $\theta = 71^\circ, 90^\circ$, and 109° . The side and back of the cluster is surrounded by bismuth germanate (BGO) scintillators.

Eight type-B detectors were placed on the xz -plane at $\theta = 36^\circ, 72^\circ, 108^\circ$, and 144° , as shown in Fig. 4.10. The central crystals of the upper and lower type-A detectors are denoted as d1 and d8, respectively, and the other surrounding six detectors are denoted d2-d7 (d9-d14). The names of Type-B detectors are shown in Fig. 4.10.

The crystal shape of the type-A detector and type-B detector are also shown in Fig 4.12.

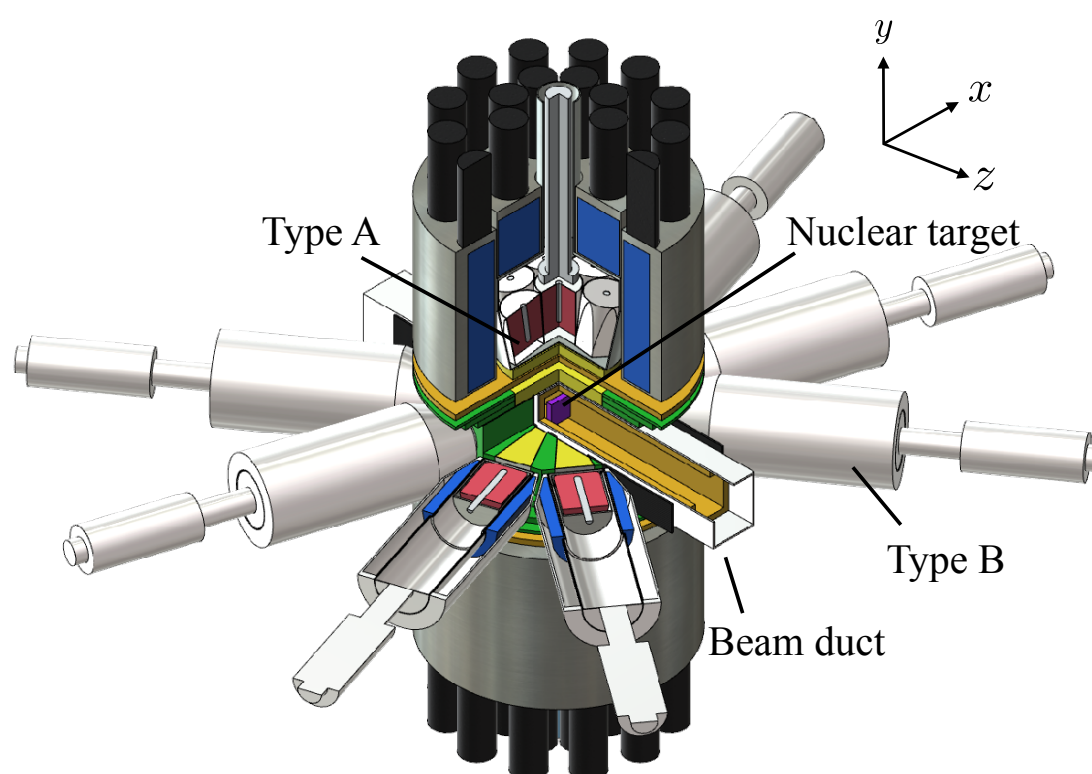


Figure 4.8: Configuration of the germanium spectrometer assembly.

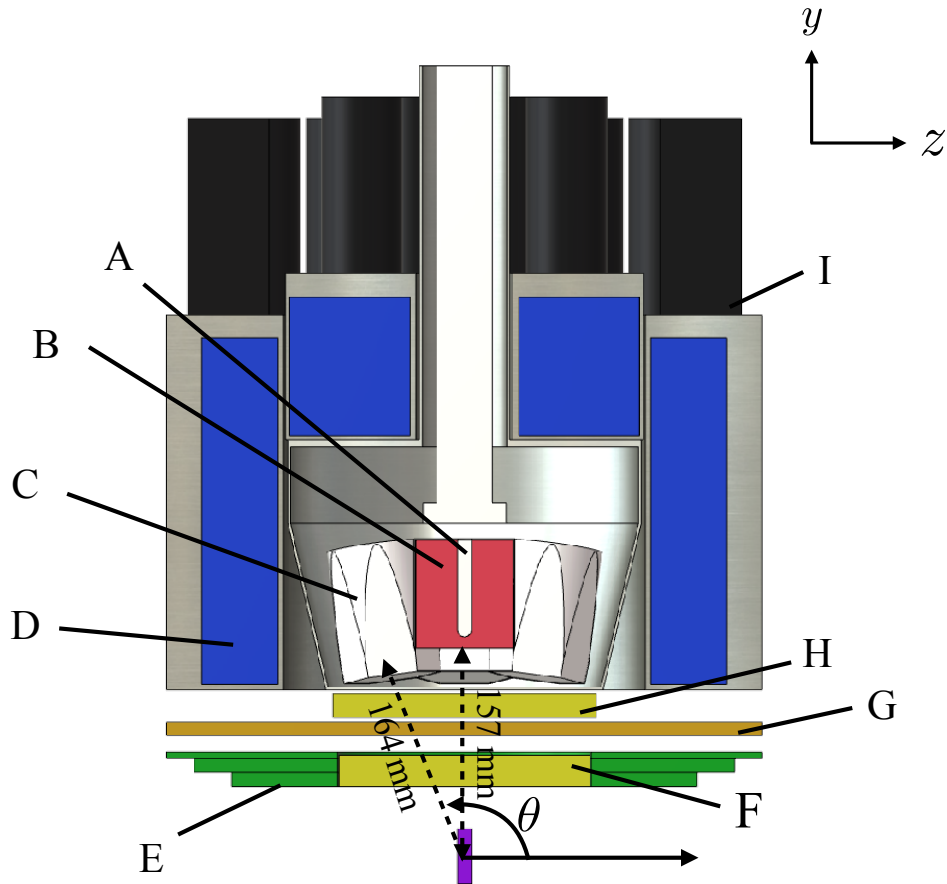


Figure 4.9: Schematics of the upper seven Type-A detectors. (A) Electrode, (B) Germanium crystal, (C) Aluminum case, (D) BGO crystal, (E) γ -ray shield (Pb collimator), (F) Neutron shield-1 (22.3 mm LiH), (G) Neutron shield-2 (5 mm LiF), (H) Neutron shield-3 (17.3 mm LiH), and (I) Photomultiplier tube for BGO crystal.

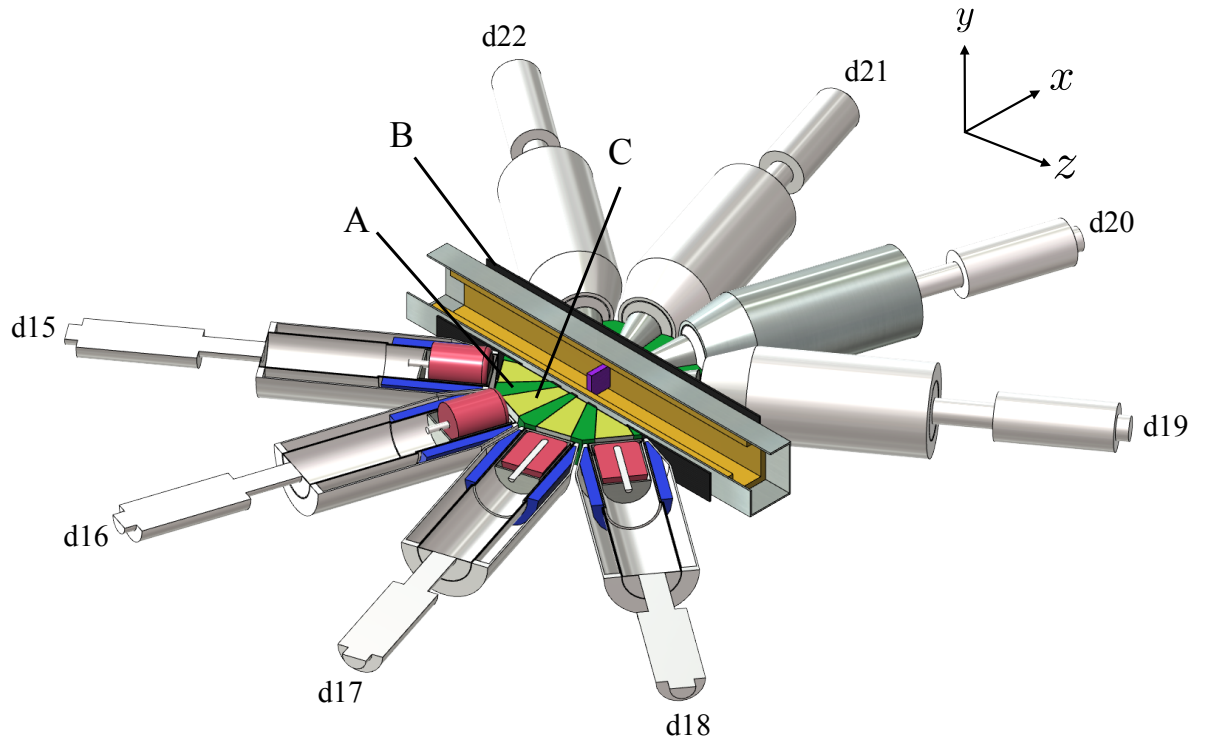


Figure 4.10: Schematics of Type-B detectors. (A) Pb collimator, (B) Carbon board, and (C) LiH powder.

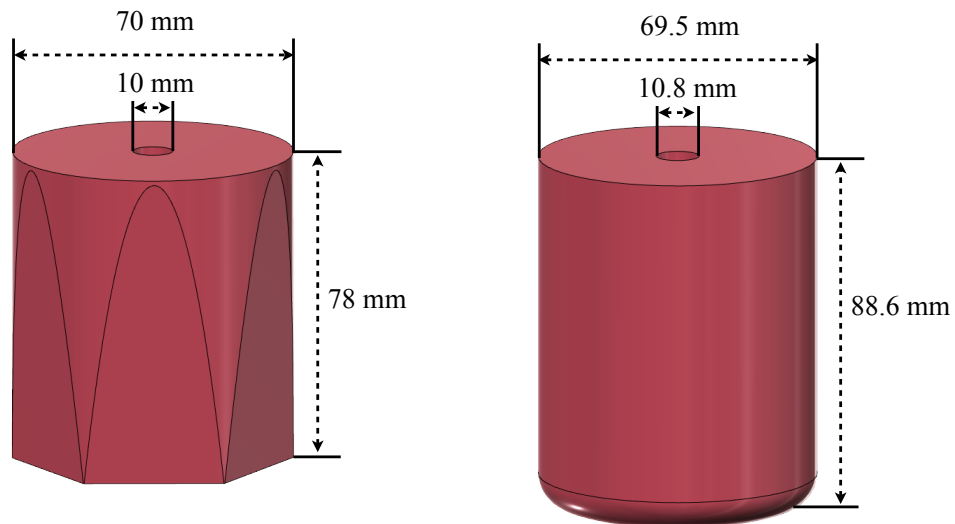


Figure 4.11: The crystal shapes of type-A detector (left) and Type-B detector (right)

The BGO scintillators surrounding the germanium detectors can be used as detectors to veto Compton-scattering events from the germanium detectors back to the BGO scintillators. All detectors are surrounded by a shielding made of borax resin, lead, and iron. Generally, it is difficult to use semiconductor detectors with a neutron beam since performance of the semiconductor detectors decrease as a result of neutron scattering. On the other hands, the careful shielding of LiF and ${}^6\text{LiH}$ from scattered neutrons enable the germanium detectors of ANNRI for use with the high intensity neutron beam of J-PARC.

The germanium detector assembly is surrounded by lead and iron shielding. Type-B detectors are inserted to the side holes of the shielding and fixed.

The beam duct consists of two layers. The outer layer is made from 3 mm-thick aluminum with a cross-sectional dimensions of 86 mm \times 96 mm. The inner layer is made from 10.5 mm-thick LiF as a shielding for scattered neutron. The beam duct can be removed by moving the lead and iron shielding.

The nucleus target was placed inside of the beam duct and was drawn out from the beam pipe with an automatic target changer without moving the lead and iron shielding.

The germanium crystals were kept at a temperature of 77 K during operation. Type-A detectors and Type-B detectors are cooled by liquid nitrogen and refrigerators X-COOLER II of ORTEC, respectively. In our measurement, d16 and d17 were not used since these were not cooled sufficiently. The typical energy resolution for the 1.332 MeV γ -rays was 2.4 keV when the neutron beam was off. it became 5.4 keV when the beam was on as a result of electronic noise from the accelerators [62].

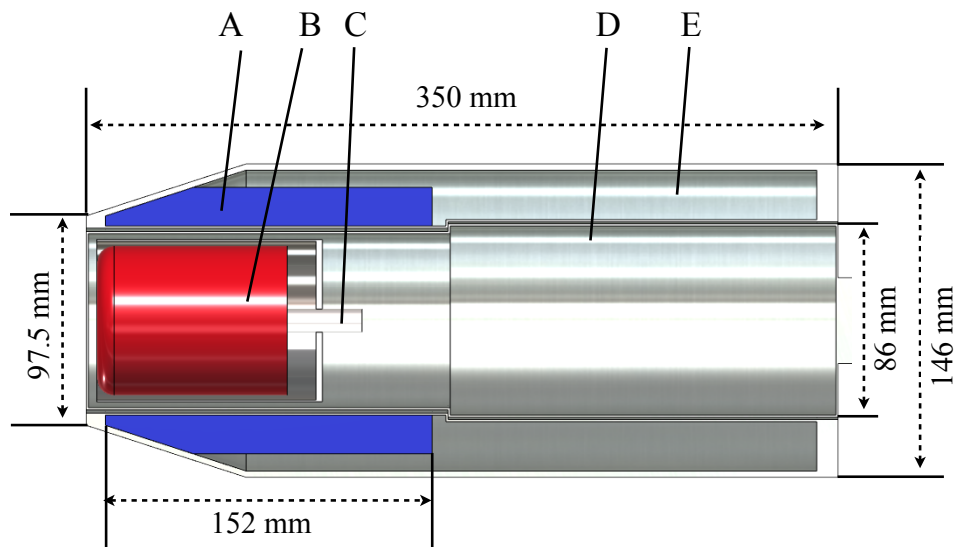


Figure 4.12: The schematics of a unit of type-B detector. (A) BGO crystal, (B) Germanium crystal, (C) Electrode, (D) and (E) Aluminum case.

4.3.1 Energy calibration and linearity of pulse height

The relationship between the pulse height of the germanium detector signal and deposited γ -ray energy of γ -ray into the germanium crystal was obtained by utilizing the 511 keV photo-peak due to pair creation of electron and positron and the 7724.03 keV photo-peak as the maximum energy of $^{27}\text{Al}(n,\gamma)$ reaction. Since the energy of these γ -rays are well-known, they can be used for the energy calibration. Additionally the linearity of pulse height is also ensured using intense photo-peaks from $^{27}\text{Al}(n,\gamma)$ reaction, and good linearity is confirmed up to 7724.03 eV as shown in Fig 4.13. Since the relationship can changed according to the temperature of the amplifiers, it was measured every day during the experiment.

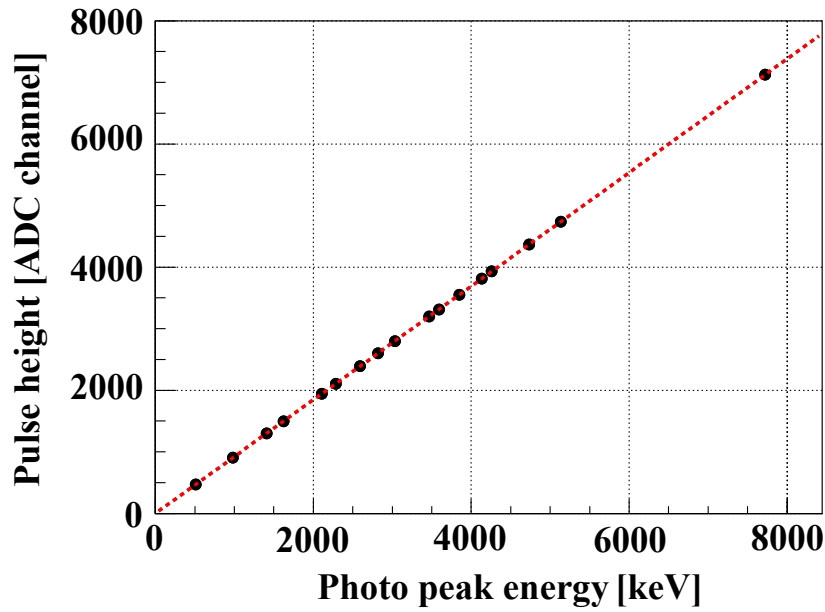


Figure 4.13: The relationship between the pulse height and the photo-peak energy. The Black dots and the dashed line show measured peak values of the full absorption peak and best fit by a linear function.

4.3.2 Definitions of symbols describing detector characteristics

We define the symbols to describe the detector characteristics in this section. We use $\psi_d(E_\gamma, \Omega_\gamma, (E_\gamma^m)_d)$ to denote the probability of the case where an energy of $(E_\gamma^m)_d$ is deposited in the d -th detector when a γ -ray with an energy of E_γ is emitted in the direction of $\Omega_\gamma = (\theta_\gamma, \varphi_\gamma)$. The polar angle and the azimuthal angle of the direction of the emitted γ -ray is denoted by θ_γ and φ_γ , respectively. $\psi_d(E_\gamma, \Omega_\gamma, (E_\gamma^m)_d)$ satisfies

$$\int_0^{E_\gamma} \psi_d(E_\gamma, \Omega_\gamma, (E_\gamma^m)_d) d(E_\gamma^m)_d = 1. \quad (4.2)$$

We define the distribution of the deposited energy as

$$\bar{\psi}_d(E_\gamma, (E_\gamma^m)_d) = \int_{\Omega_d} \psi_d(E_\gamma, \Omega_\gamma, (E_\gamma^m)_d) d\Omega_\gamma, \quad (4.3)$$

where Ω_d is the geometric solid angle of the d -th detector. The photo-peak efficiency of d -th detector for γ -rays with energy E_γ is defined as

$$\epsilon_d^{\text{pk},w}(E_\gamma) = \int_{(E_\gamma^m)_d^{w-}}^{(E_\gamma^m)_d^{w+}} \bar{\psi}_d(E_\gamma, (E_\gamma^m)_d) d(E_\gamma^m)_d, \quad (4.4)$$

where $(E_\gamma^m)_d^{w+}$ and $(E_\gamma^m)_d^{w-}$ are the upper and lower limits of the region of the energy deposited, used to defined the photo-peak region, as schematically shown in Fig. 4.14. The relative photo-peak efficiency

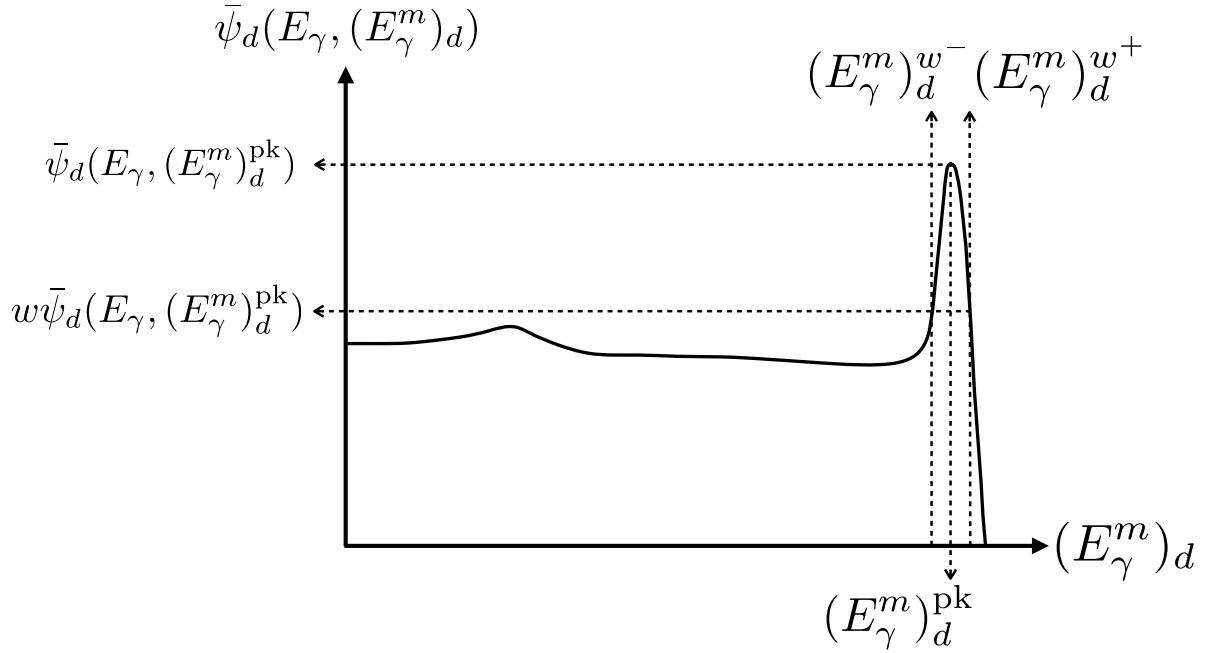


Figure 4.14: Schematic of the definition of the photo-peak in the pulse height spectrum.

is also defined as

$$\bar{\epsilon}_d^{\text{pk},w}(E_\gamma) = \frac{\epsilon_d^{\text{pk},w}(E_\gamma)}{\epsilon_1^{\text{pk},w}(E_\gamma)}. \quad (4.5)$$

In the case of angular distribution of γ -rays this is expanded using Legendre polynomials as $\sum_{p=0}^{\infty} c_p P_p(\cos \theta_\gamma)$, and the photo-peak count of the d -th detector can be written as

$$N_d(E_\gamma) = N_0 \sum_{p=0}^{\infty} c_p \bar{P}_{d,p},$$

$$\bar{P}_{d,p} = \frac{1}{4\pi} \int_{(E_\gamma^m)_d^-}^{(E_\gamma^m)_d^+} d(E_\gamma^m)_d \int d\Omega_\gamma P_p(\cos \theta_\gamma) \bar{\psi}_d(E_\gamma, \Omega_\gamma).$$
(4.6)

4.3.3 Simulation of the germanium detectors

Simulations using GEANT4.9.6 were performed to obtain response functions of each detector. The experimental data of γ -ray spectra from the radioactive source of ^{137}Cs ($E_\gamma=0.662\text{ MeV}$), ^{60}Co at $E_\gamma=1.173\text{ MeV}$, 1.332 MeV and ^{22}Na at $E_\gamma=1.275\text{ MeV}$ was obtained in each detector, and we reproduce these data by the simulation. The experimental data and the simulated result of the γ -ray spectrum of ^{137}Cs is shown in Fig. 4.15, and we can confirm that the simulation can reproduce the γ -ray spectrum for low energy γ -rays. Subsequently, we compared the experimental data and simulation results by using $^{14}\text{N}(n,\gamma)$ reactions with a Melamine target (see Section 4.5.2) to check the reproducibility of the simulation for high energy γ -rays. The reasons why $^{14}\text{N}(n,\gamma)$ reactions are used is that there are over ten kinds of γ -rays from 2000 keV to 11000 keV in $^{14}\text{N}(n,\gamma)$ reactions. The results are shown in Fig. 4.16. The simulated response functions for individual γ -rays in $^{14}\text{N}(n,\gamma)$ reactions are generated and normalized by the integral of the full absorption peak to that of experimental value. Since background γ -rays from $\text{Li}(n,\gamma)$, $\text{F}(n,\gamma)$, $\text{Al}(n,\gamma)$, $\text{Fe}(n,\gamma)$ and $\text{Ni}(n,\gamma)$ exist, these are also taken into account. The reproducibility of the simulation is evaluated by using Chi-squared test as shown in table 4.3 for each detector, and we finally confirm that the simulation can reproduce the experimental data.

From the results, it is shown that the simulation can reproduce the detector characteristics sufficiently. The photo-peak efficiency of the detector assembly is evaluated as approximately 4%.

The determined values of $\bar{P}_{d,p}$ are listed in Table 4.4 for $p = 0, 1, 2$. The quantity \bar{P}_0 corresponds to $\epsilon_d^{\text{pk},w}$. The table also contains the weighted average of the viewing angle of each detector $\bar{\theta}_d$ determined as $P_p(\cos \bar{\theta}_d) = \bar{P}_{d,p}/\bar{P}_{d,0}$.

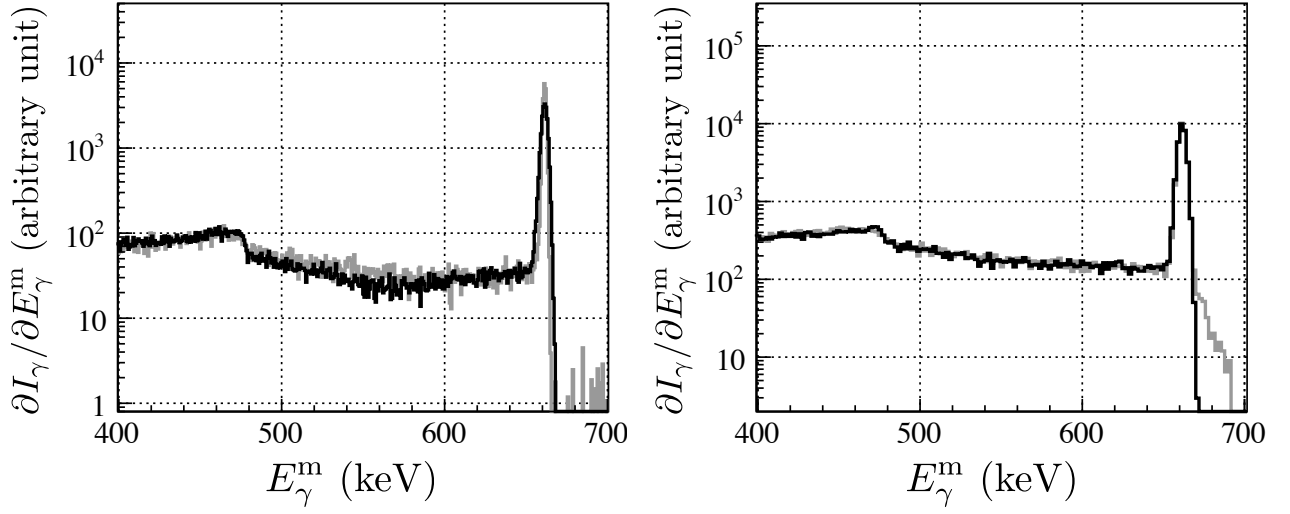


Figure 4.15: Comparison of the pulse height spectrum for γ -rays from a radioactive Cs source (gray line) and the numerical simulation (black line) for a type-B detector unit (left) and a type-A detector unit (right). As the simulation reproduces the experimental data faithfully, these almost overlap.

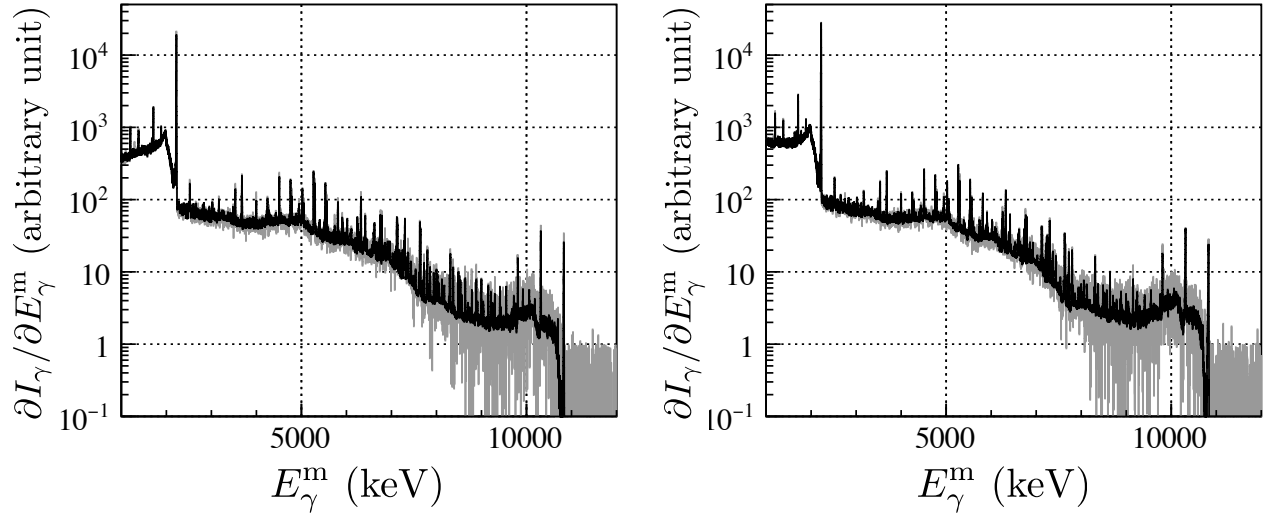


Figure 4.16: Comparison of pulse height spectrum for prompt γ -rays emitted in $^{14}\text{N}(n,\gamma)$ reaction (gray line) and the numerical simulation (black line) for a type-A detector unit (left) and a type-B detector unit (right). As the simulation reproduces the experimental data faithfully, these almost overlap.

detector ID	χ^2/ndf
d1	1.63
d2	1.93
d3	1.23
d4	1.52
d5	0.28
d6	1.29
d7	1.54
d8	0.79
d9	1.00
d10	2.47
d11	1.85
d12	1.40
d13	1.09
d14	1.35
d15	1.89
d16	2.22
d17	1.26
d18	2.34
d19	1.55
d20	-
d21	-
d22	1.92

Table 4.3: Summary of χ^2/ndf between γ -ray spectrum of the melamine target and the simulated response function for each germanium detector.

	$E_\gamma = 0.662 \text{ MeV}$			$E_\gamma = 5.262 \text{ MeV}$		
	$P_{d,1}/P_{d,0}$	$P_{2,d}/P_{d,0}$	θ_d	$P_{d,1}/P_{d,0}$	$P_{2,d}/P_{d,0}$	θ_d
1	-0.0021 ± 0.0002	-0.488 ± 0.002	90.00 ± 0.11	-0.0022 ± 0.0004	-0.490 ± 0.003	90.00 ± 0.19
2	-0.0024 ± 0.0002	-0.488 ± 0.002	90.00 ± 0.11	-0.002 ± 0.0004	-0.491 ± 0.003	90.00 ± 0.19
3	0.301 ± 0.001	-0.354 ± 0.001	72.30 ± 0.10	0.297 ± 0.002	-0.359 ± 0.003	72.55 ± 0.16
4	0.301 ± 0.001	-0.354 ± 0.001	72.31 ± 0.10	0.296 ± 0.002	-0.3560 ± 0.003	72.56 ± 0.16
5	-0.0022 ± 0.0002	-0.489 ± 0.002	90.00 ± 0.11	-0.0020 ± 0.0004	-0.491 ± 0.003	90.00 ± 0.19
6	-0.306 ± 0.0001	-0.350 ± 0.001	107.71 ± 0.14	-0.301 ± 0.002	-0.355 ± 0.003	107.45 ± 0.24
7	0.305 ± 0.001	-0.350 ± 0.001	107.70 ± 0.14	-0.302 ± 0.002	-0.355 ± 0.003	107.45 ± 0.24
8	-0.0018 ± 0.0002	-0.488 ± 0.002	90.00 ± 0.11	-0.0020 ± 0.0004	-0.490 ± 0.003	90.00 ± 0.19
9	-0.0019 ± 0.0003	-0.489 ± 0.002	90.00 ± 0.11	-0.0025 ± 0.0004	-0.491 ± 0.003	90.00 ± 0.19
10	-0.301 ± 0.0001	-0.354 ± 0.001	72.30 ± 0.10	0.297 ± 0.002	-0.360 ± 0.003	72.56 ± 0.16
11	0.301 ± 0.001	-0.355 ± 0.001	72.30 ± 0.10	0.297 ± 0.002	-0.360 ± 0.003	72.55 ± 0.16
12	-0.0019 ± 0.0003	-0.489 ± 0.002	90.00 ± 0.11	-0.0022 ± 0.0004	-0.491 ± 0.003	90.00 ± 0.19
13	-0.306 ± 0.0001	-0.350 ± 0.001	107.70 ± 0.14	-0.302 ± 0.002	-0.355 ± 0.003	107.44 ± 0.24
14	-0.305 ± 0.0001	-0.351 ± 0.001	107.70 ± 0.14	-0.301 ± 0.002	-0.356 ± 0.003	107.46 ± 0.24
15	-0.806 ± 0.001	0.479 ± 0.002	143.82 ± 0.19	-0.806 ± 0.006	0.478 ± 0.003	143.78 ± 0.31
16	-0.311 ± 0.0003	-0.348 ± 0.002	108.00 ± 0.20	-0.310 ± 0.003	-0.350 ± 0.004	107.97 ± 0.35
17	0.304 ± 0.001	-0.352 ± 0.002	72.05 ± 0.10	0.305 ± 0.002	-0.352 ± 0.002	72.06 ± 0.15
18	0.804 ± 0.0003	0.474 ± 0.002	36.18 ± 0.05	0.804 ± 0.005	0.474 ± 0.003	36.22 ± 0.08
19	0.804 ± 0.001	0.474 ± 0.002	36.18 ± 0.05	0.804 ± 0.005	0.473 ± 0.003	36.22 ± 0.08
20	0.304 ± 0.0003	-0.352 ± 0.002	72.06 ± 0.10	0.305 ± 0.002	-0.352 ± 0.002	72.07 ± 0.15
21	-0.311 ± 0.001	-0.345 ± 0.002	107.93 ± 0.15	-0.311 ± 0.002	-0.346 ± 0.002	107.95 ± 0.23
22	-0.806 ± 0.0003	0.479 ± 0.002	143.83 ± 0.19	-0.806 ± 0.005	0.478 ± 0.003	143.77 ± 0.31

Table 4.4: Values of $\bar{P}_{d,p}/\bar{P}_{d,0}$ for $p = 0, 1, 2$ are shown for all detectors together with the weighted average angle of each detector $\bar{\theta}_d$ at $E_\gamma=0.662$ MeV and $E_\gamma=5.262$ MeV. The relative peak efficiency of the d1 detector: $\varepsilon_d^{\text{pk},1/4}$ was measured using $^{14}\text{N}(n,\gamma)$.

4.4 Data acquisition system

Cross section measurements of minor actinides and long-lived-fission products have been performed using the existing germanium detector assembly and data acquisition system. This system consists of three main ADC modules, five fast timing modules, and a coincidence module. It can detect coincident γ -ray events from the germanium crystals and BGO crystals. Therefore germanium detector Compton-scattering events may be distinguished as those which reach either the other germanium crystals or the BGO crystals. Although this system was useful for the precise measurement of cross sections, it is not suitable for measurements with high count rate.

A data taking system employing CAEN V1724 modules was recently installed to achieve high count rate acquisition capabilities. Since the signals from the germanium crystals are processed independently, a count rate increase by more than a factor of 10 can be realized. However, a method to detect coincident events has not yet been established. As we need to obtain high statistics in the vicinity of the p-wave resonance in order to resolve the infrequently emitted gamma rays from the p-wave resonance to a particular final state, our experiment was performed using this system.

The output signal is processed by using four CAEN V1724 modules [63]. The output signal from each germanium detector is amplified by the preamplifier, and the information of the timing and the pulse height of the signal is extracted by CAEN V1724 as shown in Fig 4.17. The signal fed into CAEN V1724 is divided into two branches: one is for the timing and triggering and the other for the pulse height. In the timing and triggering branch, the signal is converted to a bipolar signal with a trigger and timing filter. A signal over threshold triggers a time of zero crossing measurement, used as the time of signal detection with a resolution of 10 ns. In the pulse height branch, the signal is converted to a trapezoidal signal with a trapezoidal filter and the height of the flat top of the signal from a baseline determines the pulse height. A signal scheme for the triggering and the timing and the pulse height is shown in Fig 4.18.

The CAEN V1724 has a sampling rate of 100 Msample/s and a resolution of 14 bit, which is approximately 137 μ V due to the maximum input voltage of 2.25 V peak-to-peak. The CAEN V1724 transferred the stored data to the computer during each 4 ms when 1024 event data are accumulated in the local buffer. In the case that the speed accumulating the data in the local buffer exceeds the speed to write the data to the computer, whose counting rate is around 300 kcount/s, there is a possibility that CAEN V1724 can stop. The origin of the timing is determined by the signal of the injection of the proton pulse to the mercury, which is generated in 25 Hz. In the case that the accelerator is stopped for a long time, the timing is reset in each 10.7374 s since the data recoding region of the timing is 32 bit.

Two signals temporarily closer than approximately 0.4 μ s were processed as a single event, which is called as dead event. On the other hand, their pulse heights were recorded as a zero when their time difference was in the range of approximately 0.4 μ s to 3.2 μ s and these events called as pile up events. These events are generated in the measurement with a high counting rate. If these events cannot be negligible, the correction is needed for the analysis.

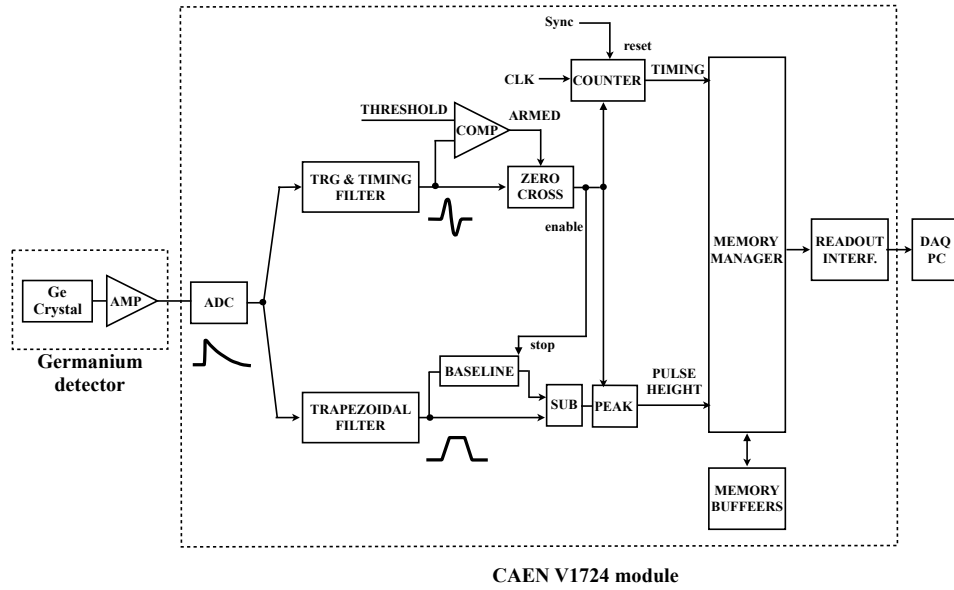


Figure 4.17: Block diagram of the signal processing. A signal from the germanium detector is divided into two branches: one for the timing and triggering and the other for the pulse height. In the branch of timing and triggering, the signal is converted to a bipolar signal. Signals over a threshold are triggered and the time of zero crossing determines the timing of the signal. In the branch of the pulse height, the signal is converted to a trapezoidal signal and the height of the trapezoidal from a baseline determines the pulse height of the signal.

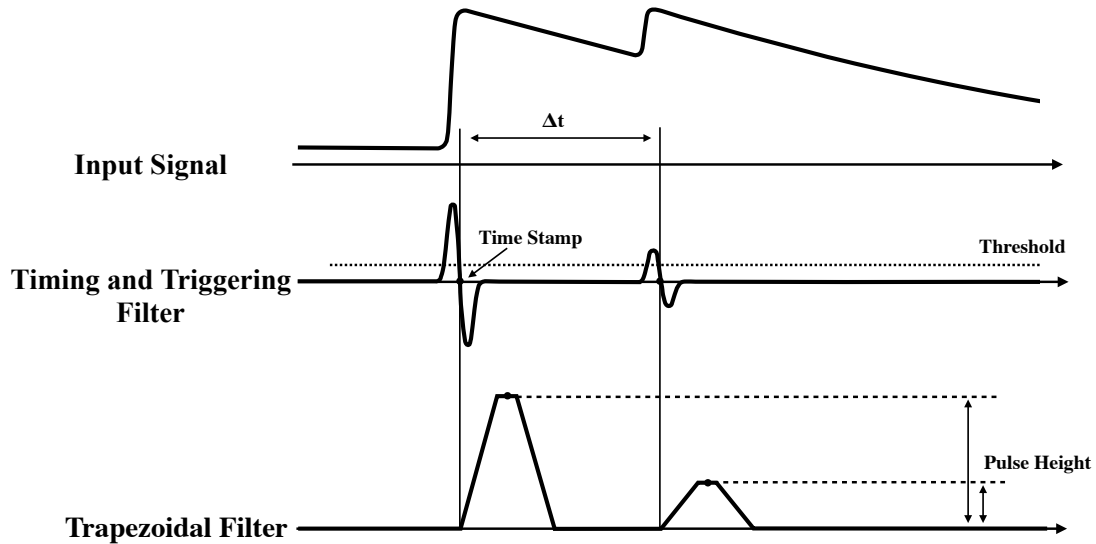


Figure 4.18: Schematic of the signal processing when two signals are detected. The input signals fed into the timing and triggering filter and the trapezoidal filter are converted to bipolar signal and trapezoidal signal. The bipolar signal over the threshold determines the timing, and then the pulse height is determined using the height of the trapezoidal signal.

4.5 Nuclear targets

Lanthanum, boron carbide and melamine targets were used for our experiment. Properties of the targets are described in this section. The targets were sealed by polytetrafluoroethylene with a thickness of $10\ \mu\text{m}$ due to the regulations at MLF.

4.5.1 Lanthanum target

A $^{\text{nat}}\text{La}$ target with dimensions of $40\ \text{mm} \times 40\ \text{mm} \times 1\ \text{mm}$ was used in this experiment to measure the angular dependence of γ -rays. The target thickness such that multiple scattering of incident neutrons in the target are sufficiently small was determined by Monte-Carlo simulations.

The purity of the $^{\text{nat}}\text{La}$ target was 99.9%. Contamination of the target was evaluated by inductively coupled plasma spectroscopy and given in table 4.5.

contamination	quantity (ppm)
Cerium	200
Praseodymium	120
Neodymium	200
Samarium	200
Dysprosium	200
Yttrium	200
Iron	227
Silicon	120
Aluminum	110
Carbon	100
Sulfur	100
Chlorine	150

Table 4.5: The contaminations of the lanthanum target.

4.5.2 Boron carbide target

The boron carbide target was used to measure the neutron beam intensity. The chemical formula of boron carbide is B_4C and γ -rays from $^{10}\text{B}(\text{n},\alpha\gamma)^7\text{Li}$ reactions were used for the measurement. Boron carbide powder made from 95% enriched ^{10}B was diluted with 20 times as much carbon powder and pressed into a tablet with dimensions of $0.59\ \text{mm} \times \phi 5.08\ \text{mm}$ and mass of 20.1 mg.

The reasons why $^{10}\text{B}(\text{n},\alpha\gamma)^7\text{Li}$ reactions are used to measure the neutron beam intensity are that its reaction cross section is large (3837 barns for thermal neutrons [49]) and it is easy to separate background γ -rays from contamination of the target and the detector material since only single energy γ -ray (477.6 keV) is emitted in the reactions.

4.5.3 Melamine target

The melamine target was used to correct the detection efficiency and the solid angle coverage of each detector. The chemical formula of melamine is $\text{C}_3\text{H}_6\text{N}_6$ and the $^{14}\text{N}(\text{n},\gamma)$ reaction was used for the correction. A tablet-shaped melamine target with dimensions of $1.0 \text{ mm} \times \phi 5.08 \text{ mm}$ was used.

The reasons why $^{14}\text{N}(\text{n},\gamma)$ reactions are used for this correction are that the γ -rays in the reactions are emitted isotropically and the correction for a wide range of the γ -ray energies are possible since there are over ten kinds of γ -rays from 2000 keV to 11000 keV in the reaction. It can be reasonably assumed that the γ -rays are emitted isotropically, as the ^{14}N does not have any resonance below 400 eV and p-wave or higher angular momentum components of the incident neutron are negligibly small in this energy region.

Chapter 5

Measurement

In this section, the results of the angular distribution and corrections for the measurement are described.

5.1 Definitions of the symbols describing the measurement results

Neutron energies are measured using the Time-of-Flight (TOF) method. Here, the corresponding neutron energy E_n^m is defined as

$$E_n^m = \frac{m_n}{2} \left(\frac{L}{t_m} \right)^2, \quad (5.1)$$

where m_n is the neutron mass, L is the distance between the target and the moderator surface and t_m is the time between γ -ray detection and the timing pulse of the injection of the proton beam bunch. The deposited γ -ray energy E_γ^m obtained by the calibration of the pulse height using $\text{Al}(n, \gamma)$ as shown in Section 4.3.1 is also defined.

The neutron energy in the center-of-mass system E is described as

$$E = \frac{m_n m_A}{m_n + m_A} \left(\frac{\mathbf{p}_n}{m_n} - \frac{\mathbf{p}_A}{m_A} \right)^2, \quad (5.2)$$

where \mathbf{p}_n is the momentum of the incident neutron in the laboratory system, \mathbf{p}_A is momentum of the target nucleus, and m_A is the mass of the target nucleus.

The divergence of the neutron beam is sufficiently small and the following can be assumed:

$$\mathbf{p}_n = \sqrt{2m_n E_n} \mathbf{e}_z, \quad (5.3)$$

where \mathbf{e}_z is the unit vector parallel to the beam axis.

The total number of γ -rays is denoted as I_γ .

5.2 Measurement of the beam intensity spectrum

The beam spectrum was obtained by measuring the γ -rays via $^{10}\text{B}(\text{n},\alpha\gamma)^7\text{Li}$ reactions with the boron carbide target placed at the center of the germanium detector assembly. The measurement was performed for 4.7 hours (4.3×10^5 shots) with $\phi 22$ mm beam size. An energy spectrum of γ -rays and the TOF spectrum are shown in Fig 5.1 and Fig 5.2, respectively. The TOF spectrum was drawn with the gate at $E_n=477.6$ keV photo-peak to select events from the $^{10}\text{B}(\text{n},\alpha\gamma)^7\text{Li}$ reaction. Neutrons over 27 ms were suppressed by the disk chopper to avoid frame overlap as shown in Fig 5.2.

The number of the γ -ray events I_γ is described as

$$I_\gamma(E_n) = F(E_n)\epsilon^{\text{pk}}(E_\gamma)S(1 - \exp(-\rho d\sigma(E_n))), \quad (5.4)$$

where $F(E_n)$ is the beam intensity, $\epsilon^{\text{pk}}(E_\gamma)$ is the detection efficiency of the germanium detector assembly for 477.6 keV γ -rays, S is the area ratio of the target size to the beam size, ρ is the number density of ^{10}B , d is the thickness of the boron carbide target and $\sigma(E_n)$ is the cross section of the $^{10}\text{B}(\text{n},\alpha\gamma)^7\text{Li}$ reaction.

The beam intensity spectrum $F(E_n)$ was obtained by the division of $I_\gamma(E_n)$ by $(1 - \exp(-\rho d\sigma(E_n)))$ as shown in 5.3. Here, the effect of the multiple scattering of neutrons in the target was taken into account by using a Monte Carlo simulation. The cross section of the $^{10}\text{B}(\text{n},\alpha\gamma)^7\text{Li}$ reaction is referred to from JNDLE-4.0 [48].

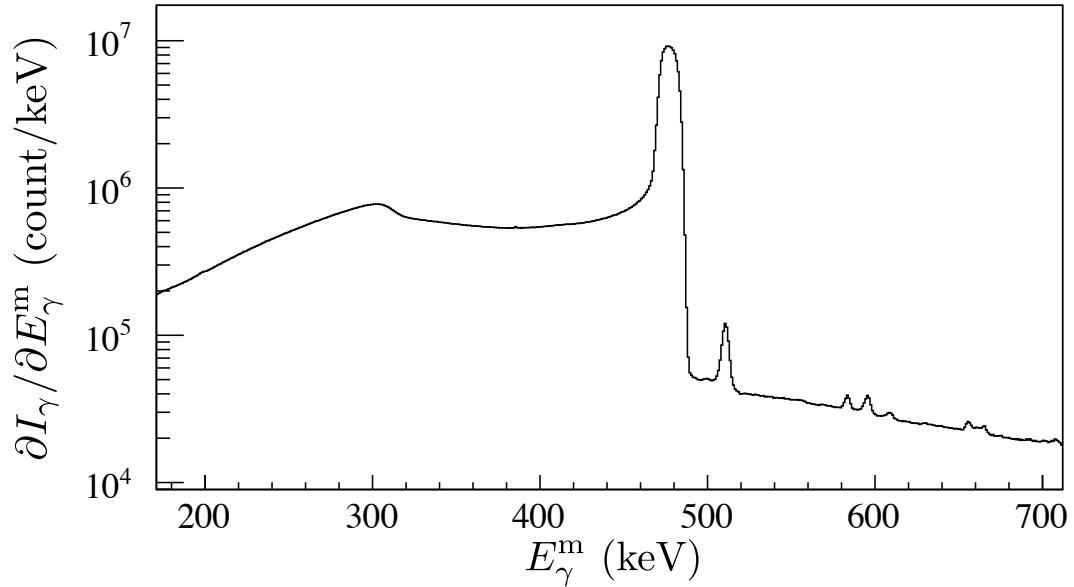


Figure 5.1: γ -ray spectrum with the boron carbide target. The largest photo-peak at 477 keV is a full absorption peak from the $^{10}\text{B}(\text{n},\alpha\gamma)^7\text{Li}$ reaction.

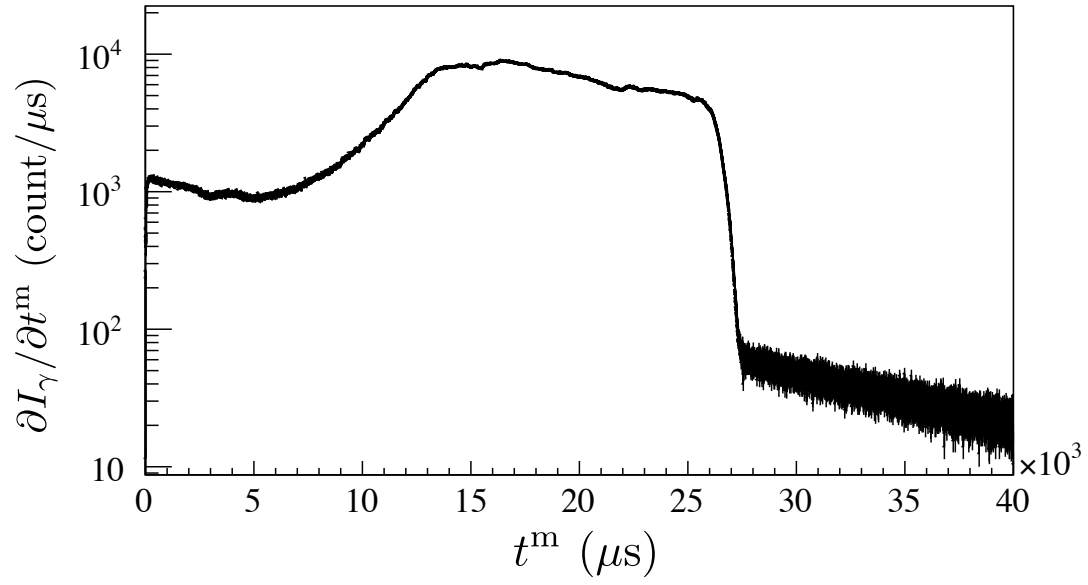


Figure 5.2: TOF spectrum gated with the 477 keV photo-peak with the boron carbide target.

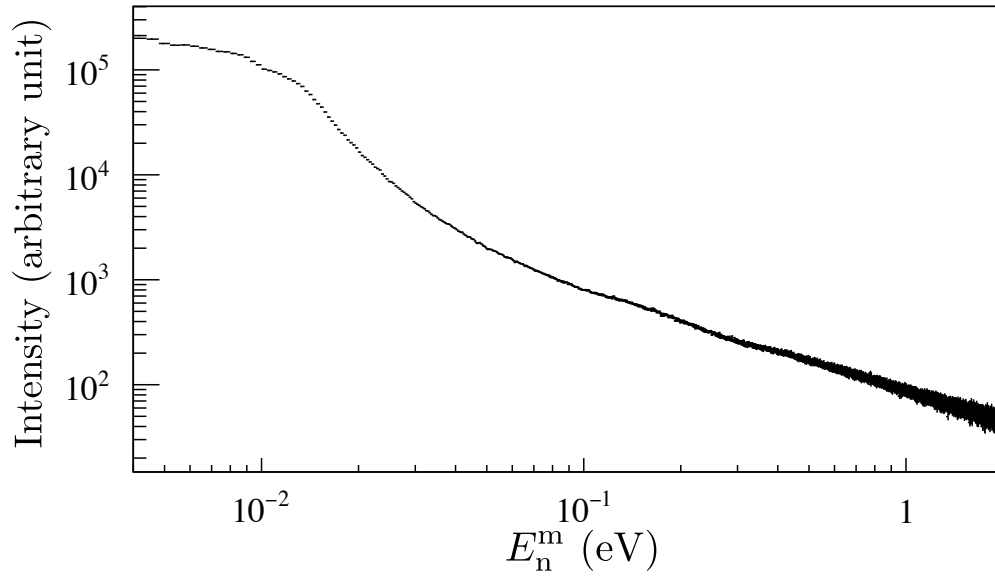


Figure 5.3: Beam intensity spectrum measured with the boron carbide target.

5.3 Measurement of the angular distribution in $^{139}\text{La}(n, \gamma)$ reactions

5.3.1 γ -ray spectrum and TOF spectrum

The measurement for the angular distribution in $^{139}\text{La}(n, \gamma)$ reactions was carried out using the lanthanum target for 60 hours (5.4×10^7 shots) with $\phi 22$ mm beam size. We obtained 2-dimensional data of γ -ray energy and TOF, and the results are shown as a 2-dimensional histogram corresponding to $\partial^2 I_\gamma / \partial t^m \partial E_\gamma^m$ in Fig. 5.4. The γ -ray spectrum and the TOF spectrum can be obtained by projecting

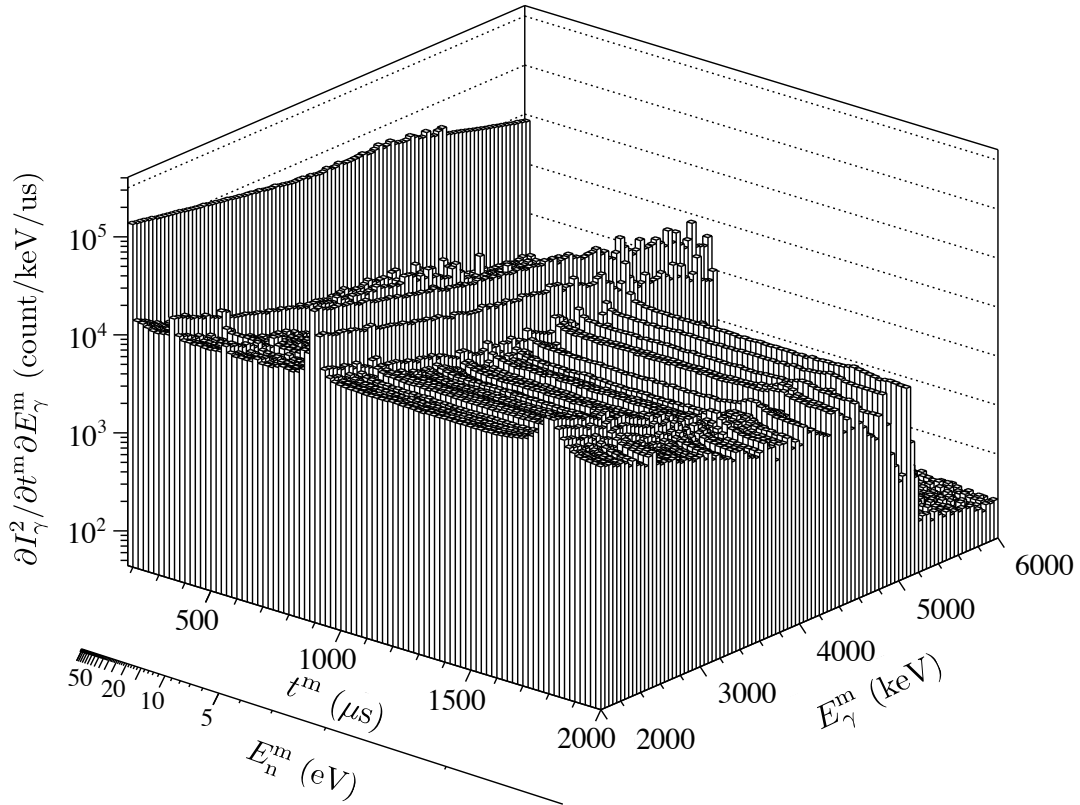


Figure 5.4: $\partial^2 I_\gamma / \partial t^m \partial E_\gamma^m$ 2-dimensional histogram of γ -rays with the lanthanum target as a function of leading-edge timing t^m and photo-peak γ -ray energy E_γ^m . The corresponding neutron energy E_n^m is also shown.

the 2-dimensional histogram on E_n^m and E_γ^m as shown in Fig. 5.5 and Fig. 5.7, respectively. Figure 5.7 shows the TOF spectrum integrated the γ -ray energy over 2 MeV to eliminate the delayed γ -rays and normalized by the incident beam intensity spectrum measured with the boron carbide target. The p-wave resonance is observed at $t^m \sim 1800 \mu\text{s}$, and the $1/v$ component is the tail of the negative s-wave resonance as listed in Table 2.2. The positive s-wave resonances of ^{139}La and ^{138}La are also observed.

The level scheme related to $^{139}\text{La}(n, \gamma)^{140}\text{La}$ reaction is schematically shown in Fig. 2.6. The γ -ray transitions to the ground state and low excited states of ^{140}La are observed and the spins and the parities of the excited state were identified as shown in the expanded $\partial I_\gamma / \partial E_\gamma^m$ (Fig. 5.6). The highest

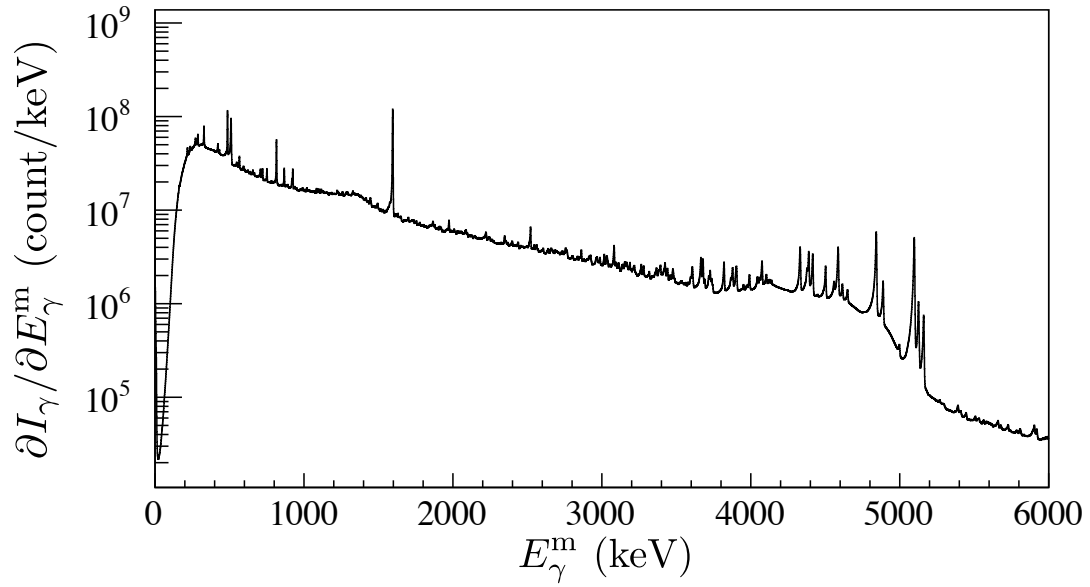


Figure 5.5: Pulse height spectrum of γ -rays $\partial I_\gamma / \partial E_\gamma^m$ from the (n, γ) reaction with lanthanum target as a function of E_γ^m .

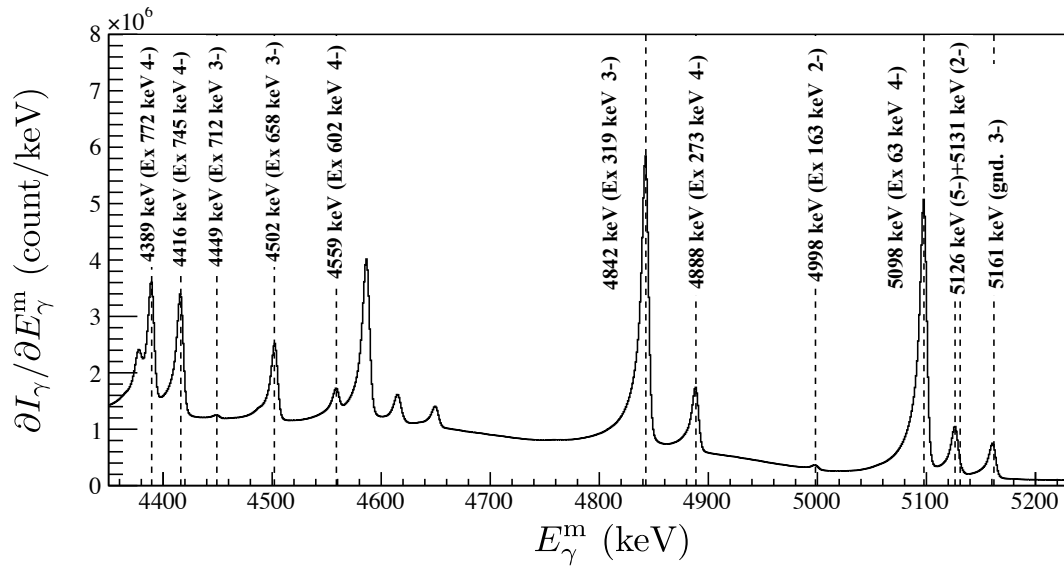


Figure 5.6: Expanded pulse height spectrum of $\partial I_\gamma / \partial E_\gamma^m$ from the (n, γ) reaction with lanthanum target as a function of E_γ^m . The full absorption peaks from the γ -ray transitions to the ground state and low excited state of ^{140}La were observed and the spins and the parities of the final state were identified. Three peaks around 4600 keV are single escape peaks of the three peaks around 5100 keV.

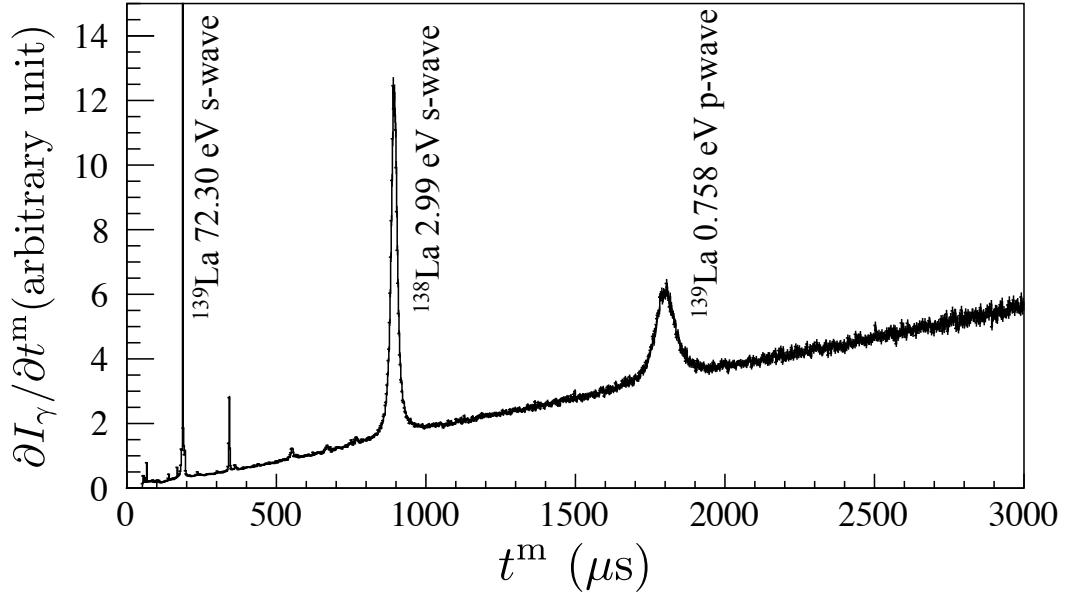


Figure 5.7: γ -ray count normalized by the incident beam intensity as a function of t^m for $E_\gamma^m \geq 2$ MeV, which is referred to as $\partial I_\gamma / \partial t^m$.

peak at $E_\gamma^m = 5161$ keV corresponds to the γ -ray transition to the ground state of ^{140}La (spin of the final state: $F=3$), the second highest peak corresponds to the overlap of two transitions at $E_\gamma^m = 5131$ keV and 5126 keV to the first and second excited states at excited energy 31 keV ($F=5$), 35 keV ($F=2$), and the third highest peak at $E_\gamma^m = 5098$ keV corresponds to the fourth excited state at 63 keV ($F=4$). Figure 5.8 shows the magnified 2-dimensional histogram of $\partial^2 I_\gamma / \partial t^m \partial E_\gamma^m$ in the vicinity of the p-wave resonance and the γ -ray transition to the ground state of ^{140}La . The p-wave resonance was selectively observed only for two ridges corresponding to the transition at $E_\gamma^m = 5161$ keV and the sum of transitions at $E_\gamma^m = 5131$ keV, 5126 keV, but not for the ridge at $E_\gamma^m = 5098$ keV. According to the dependence of $\partial^2 I_\gamma / \partial t^m \partial E_\gamma^m$ on t^m , and therefore on the incident neutron energy, the negative s-wave resonance contributes to all three γ -ray transitions, and the p-wave resonance contributes to the 5161 keV transition and 5131 keV and/or 5126 keV transitions.

Since the second highest peak corresponds the overlap of two transitions, hereafter we consider the angular distribution of the 5161 keV γ -rays corresponding to the transition to the ground state of ^{140}La , in order to study the interference between the s- and p-wave amplitudes.

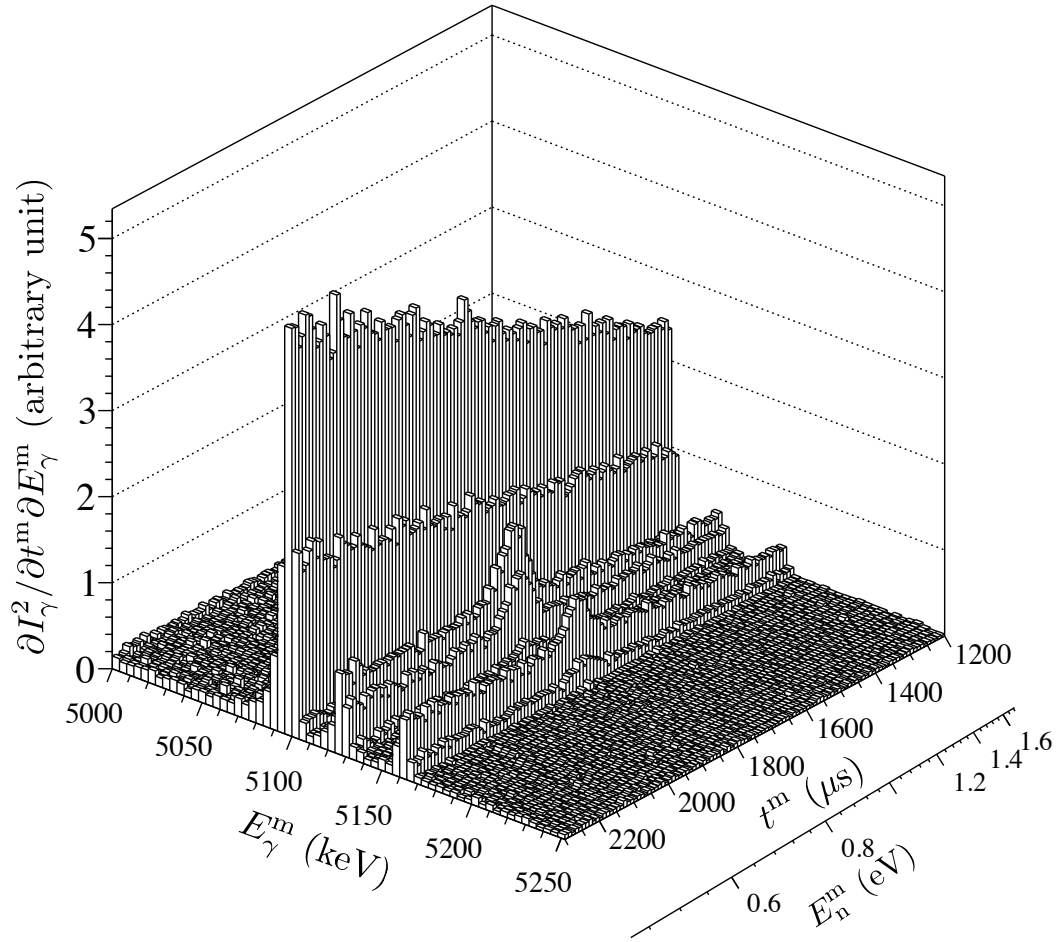


Figure 5.8: Magnified 2-dimensional histogram. The p-wave resonance is observed at only 5161 keV and 5131 keV and/or 5126 keV photo-peaks.

5.3.2 Fitting to obtain the resonance parameters

The resonance energy E_r and the total width Γ_r of the r -th resonance were obtained by fitting $I_\gamma(t^m)$ normalized by the beam spectrum with functions of the neutron absorption cross section with convolutions of the pulse shape of the neutron beam and the doppler effect of the target nucleus. The formalism of the neutron absorption cross section is described in Appendix A. The Ikeda–Carpenter function as shown in Eq 4.1 is used to describe the pulse shape. The energy spectrum at a given time t^m at a distance of L from the moderator surface is given as

$$\frac{\partial I_n}{\partial t^m}(t^m) = \int dE' \frac{\partial^2 I_n}{\partial E_n \partial t} \left(E', t^m - L \sqrt{\frac{m_n}{2E'}} \right). \quad (5.5)$$

The free gas model is adopted to describe the thermal motion of the target nuclei, which leads to the γ -ray yield in the form of

$$\begin{aligned} \frac{\partial I_\gamma}{\partial t^m}(t^m) = & I_0 \int dE' d^3p_A \frac{\partial^2 I_n}{\partial E_n \partial t} \left(E', t^m - L \sqrt{\frac{m_n}{2E'}} \right) \\ & \times \frac{1}{(2\pi m_A k_B T)^{3/2}} e^{-p_A^2/2m_A k_B T} \\ & \times \frac{\sigma_{n\gamma}(E_n)}{\sigma_t(E_n)} \left(1 - e^{-n\sigma_t(E) \Delta z} \right), \end{aligned} \quad (5.6)$$

as long as the target is sufficiently thin, such that multiple scattering is negligible. I_0 is the normalization constant, Δz is the target thickness, n is the number density of target nuclei, k_B is the Boltzmann constant, and T is the effective temperature of the target, which can be used as a fitting parameter. The neutron spectrum, which does not include γ -rays less than 2 MeV to eliminate radio active γ -rays from excited ^{140}La , was fitted by Eq. 5.6 whose fitting parameters is E_2 , Γ_γ , T and I_0 as shown in Fig. 5.9. The obtained resonance parameters are shown in Table 5.1, together with the published values. As the neutron width of the p-wave resonance is negligibly smaller than γ -ray width of the p-wave resonance, the total width of p-wave resonance was used as the γ -ray width of p-wave resonance.

published values			this work	
E_r [eV]	Γ_r^γ [meV]	$g_r \Gamma_r^n$ [meV]	E_r [eV]	Γ_r^γ [meV]
$0.758 \pm 0.001^{(b)}$	$40.11 \pm 1.94^{(c)}$	$(5.6 \pm 0.5) \times 10^{-5(c)}$	0.7404 ± 0.002	40.41 ± 0.76

Table 5.1: Resonance parameters of ^{139}La of the published value and the measured value in this work. (b) taken from Ref. [50]. (c) calculated from Refs. [51] and [50].

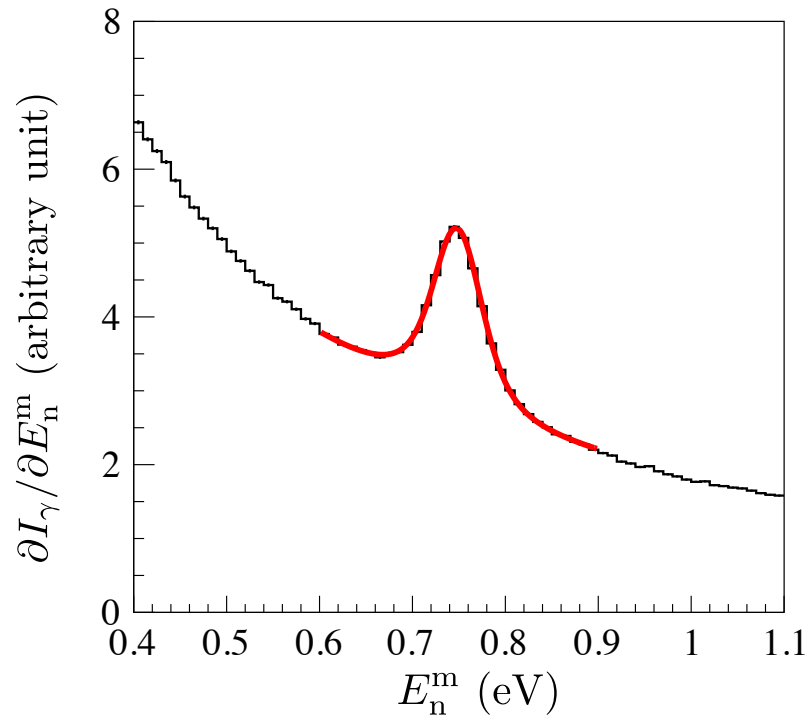


Figure 5.9: Fitted result of the p-wave resonance. The solid line shows the best fit. The Breit-Wigner functions of the s-wave and the p-wave resonance with the convolutions of the pulse shape of the neutron beam and the thermal motion of the target nucleus is adopted as the fitting function.

5.3.3 Correction for the relative photo-peak efficiency

In order to obtain the angular distribution of γ -rays, the correction for the relative photo-peak efficiencies of all germanium crystals is needed. The relative photo-peak efficiency, including both the detection efficiency and the solid angle coverage, was measured using the photo-peak counts of the γ -rays from the $^{14}\text{N}(\text{n},\gamma)$ reaction measured with the melamine target placed at the center of the germanium detector assembly.

The measurement was performed for 7.7 hours (7.0×10^5 shots) with $\phi 22$ mm beam size. The γ -ray spectrum is shown in Fig 5.10. The intense γ -ray peaks from $^{14}\text{N}(\text{n},\gamma)$, $^{12}\text{C}(\text{n},\gamma)$ and $^1\text{H}(\text{n},\gamma)$ reactions were observed in the spectrum.

The photo-peak counts of the γ -rays at $E_\gamma^{\text{m}}=5262$ keV from the $^{14}\text{N}(\text{n},\gamma)$ reaction are used to evaluate the relative photo-peak efficiencies for 5161 keV γ -rays from $^{139}\text{La}(\text{n},\gamma)$. An enlarged γ -ray $\partial I_\gamma / \partial E_\gamma^{\text{m}}$ of d7 detector is also shown in Fig. 5.11. The γ -ray background at $E_\gamma^{\text{m}}=5262$ keV is evaluated by a best-fit third polynomial of E_γ^{m} . The fitting regions are $5320 \text{ keV} \leq E_\gamma^{\text{m}} \leq 5360 \text{ keV}$ and $5200 \text{ keV} \leq E_\gamma^{\text{m}} \leq 5240 \text{ keV}$. The photo-peak counts are obtained by subtracting the background for all detectors and the relative efficiencies $\bar{\epsilon}_d^{\text{pk},1/4}(E_\gamma^{\text{m}} = 5262 \text{ keV})$ are obtained as shown in Table 5.2.

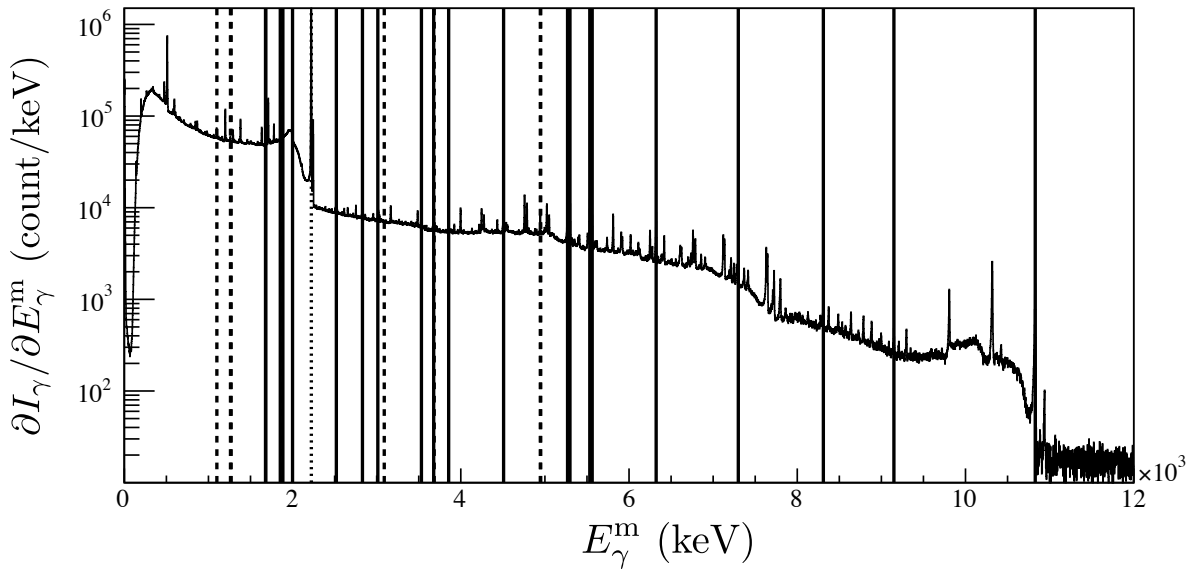


Figure 5.10: Pulse height spectrum of γ -rays $\partial I_\gamma / \partial E_\gamma^{\text{m}}$ from the (n,γ) reaction with the melamine target as a function of E_γ^{m} . Solid lines shows the energies of the intense photo-peaks which can be used for the correction for the relative photo-peak efficiency. Dashed lines and dotted lines show the γ -ray energies from $^{12}\text{C}(\text{n},\gamma)$ and $^1\text{H}(\text{n},\gamma)$, respectively.

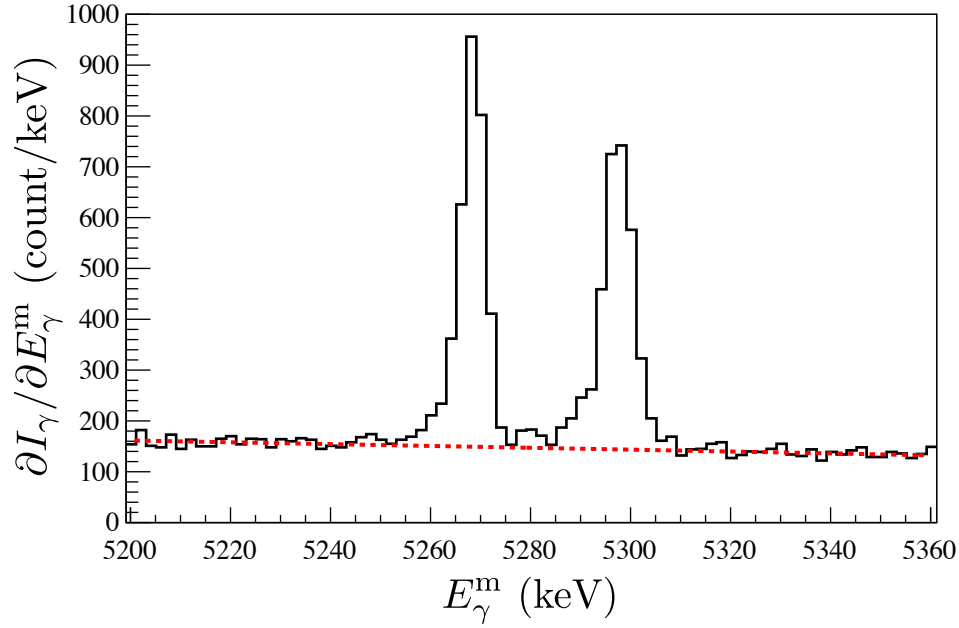


Figure 5.11: Expanded pulse height spectrum of γ -rays $\partial I_\gamma / \partial E_\gamma^m$ from the (n, γ) reaction with the melamine target as a function of E_γ^m . The dotted line shows the fitting result of the background γ -rays caused by Compton scattering of higher energy γ -rays.

detector	$\bar{\epsilon}_d^{\text{pk}, 1/4}(E_\gamma^m = 5262 \text{ keV})$
1	1
2	0.997 ± 0.027
3	0.920 ± 0.026
4	1.041 ± 0.028
5	1.025 ± 0.028
6	1.092 ± 0.029
7	0.999 ± 0.027
8	0.923 ± 0.026
9	0.915 ± 0.026
10	0.998 ± 0.027
11	0.945 ± 0.026
12	0.979 ± 0.027
13	1.046 ± 0.028
14	1.142 ± 0.030
15	0.892 ± 0.025
16	0.356 ± 0.014
17	0.945 ± 0.026
18	1.170 ± 0.031
19	0.917 ± 0.026
20	-
21	-
22	1.113 ± 0.030

Table 5.2: The relative photo-peak efficiencies $\bar{\epsilon}_d^{\text{pk}, 1/4}$ for all detectors. d20 and d22 detectors were not used.

5.3.4 Correction for the background γ -rays

The photo-peak counts of the 5161 keV transition were determined by subtracting the background counts caused by Compton scattering of the more energetic γ -rays from targets other than the lanthanum target. In order to evaluate the background, two energy regions were used: (I) $5200 \text{ keV} \leq E_\gamma^m \leq 5290 \text{ keV}$ and (II) $4900 \text{ keV} \leq E_\gamma^m \leq 4980 \text{ keV}$. The contribution of Compton scattering of γ -rays corresponding to the three photo-peaks are contained in region (II). The amount of this contribution from Compton scattering was estimated using the response function $\bar{\psi}$ given in Eq. 4.3 and obtained by simulation. The background in region (II) was estimated by subtracting the Compton contribution from the γ -ray counts in region (II). The background was estimated using a best-fit third-order polynomial of E_γ^m in regions (I) and (II).

There still remains a possible contamination of prompt γ -rays from impurities overlapping with the 5161 keV photo-peak. The possible contamination was examined over the entire pulse height spectrum, and was determined to be less than 0.08% of the photo-peak. The possibility of contamination was neglected as the determined upper limit of 0.08% is smaller than the statistical error of the photo-peak.

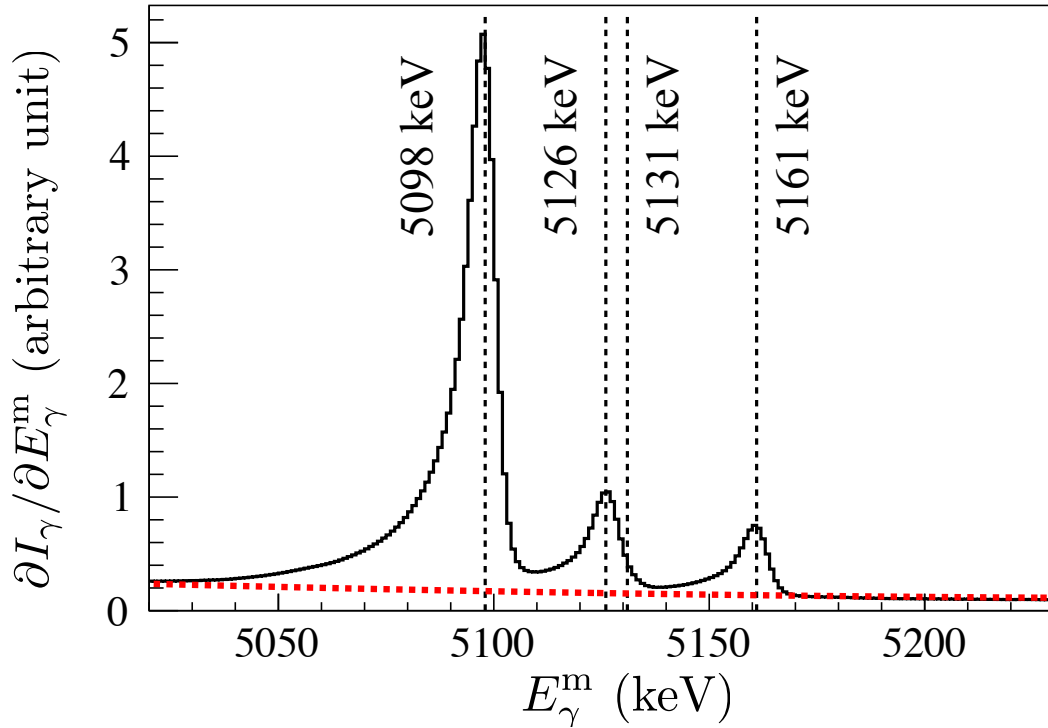


Figure 5.12: Expanded $I_\gamma(E_\gamma^m)$. The broken line shows the background determined by the simulation.

5.3.5 Correction for the pileup of the detector signals

Due to the data acquisition system design, the pulse heights of the events were recorded as a zero when their time difference was in the range of approximately $0.4 \mu\text{s}$ to $3.2 \mu\text{s}$. These pileup events are amounted to 2% of the total γ -ray counts in the vicinity of the p-wave resonance. The dead events, which occurred when two events are closer than approximately $0.4 \mu\text{s}$, are 0.2%, which can be ignored following analysis since it is sufficiently small compared to the statistical error of the total γ -ray counts. As the pileup events do not have the information of the pulse height, the neutron spectrum gated with 5161 keV photo-peak is needed the correction for the pileup events. The number of the events gated with the γ -ray energy is corrected as

$$N_{\text{gated}} = N'_{\text{gated}} \frac{N_{\text{total}}}{N_{\text{total}} - N_{\text{pileup}}}, \quad (5.7)$$

where N_{gated} is corrected number of the events gated with the γ -ray, N'_{gated} is the number of the events gated with the γ -ray energy before the correction, N_{pileup} is the number of pileup events and N_{total} is the number of the total events. The neutron spectra gated with 5161 keV at $\bar{\theta}_d = 90^\circ$ before and after the correction for pileup events are shown in Fig. 5.13.

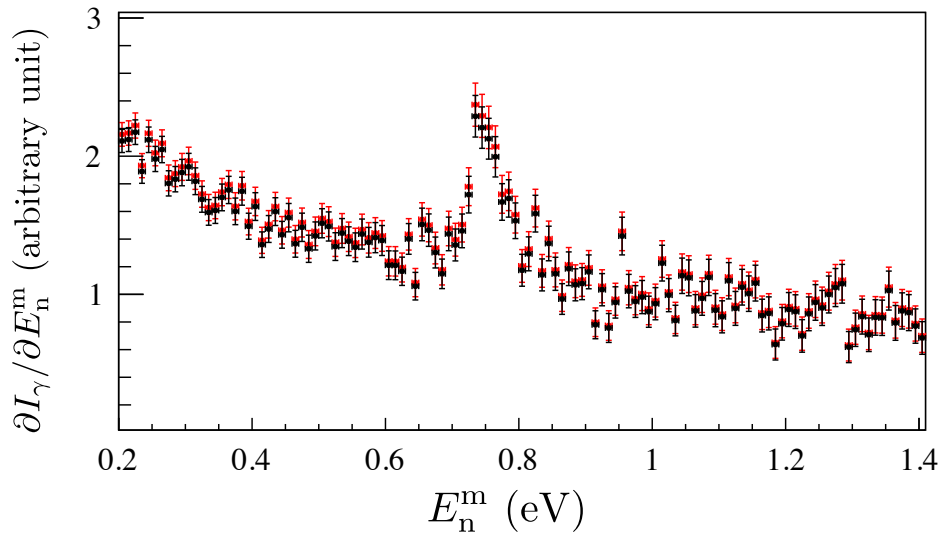


Figure 5.13: The neutron spectra in the vicinity of the p-wave resonance gated with 5161 keV at $\bar{\theta}_d = 90^\circ$ before (black points) and after (red points) the correction for pileup events. The correction amount is approximately 2% at the peak of the p-wave resonance.

5.3.6 Angular Distribution

Equation 5.6 was extended to describe the angular distribution of γ -rays as

$$\begin{aligned} \frac{\partial^2 I_\gamma}{\partial t^m \partial \Omega_\gamma}(t^m, \Omega_\gamma) &= I_0 \int dE' d^3 p_A \Phi(t^m, E', \mathbf{p}_A) \frac{d\sigma_{n\gamma}}{d\Omega_\gamma}(E, \Omega_\gamma), \\ \Phi(t^m, E', \mathbf{p}_A) &= \frac{\partial^2 \phi}{\partial E_n \partial t} \left(E', t^m - L \sqrt{\frac{m_n}{2E'}} \right) \\ &\quad \times \frac{1}{(2\pi m_A k_B T)^{3/2}} e^{-p_A^2/2m_A k_B T} \\ &\quad \times \frac{1}{\sigma_t(E)} \left(1 - e^{-n\sigma_t(E) \Delta z} \right). \end{aligned} \quad (5.8)$$

The γ -ray count to be measured by the d -th detector can be written as

$$\begin{aligned} \frac{\partial N}{\partial t^m}(t^m, \bar{\theta}_d) &= \int_{\Omega_d} d\Omega_\gamma \int_{(E_\gamma^m)_d^{w+}}^{(E_\gamma^m)_d^{w-}} d(E_\gamma^m)_d \\ &\quad \times \frac{\partial^2 I_\gamma}{\partial t^m \partial \Omega_\gamma}(t^m, \Omega_\gamma) \psi_d(E_\gamma, \Omega_\gamma, (E_\gamma^m)_d), \end{aligned} \quad (5.9)$$

where the photo-peak region is taken as the full-width at quarter-maximum, which implies $w = 1/4$. Figure 5.14 shows the $\partial N(t^m, \bar{\theta}_d)/\partial t^m$ at the vicinity of the p-wave resonance for 5161 keV γ -rays after all corrections. It can clearly be seen that the peak shape of the p-wave resonance varies according to $\bar{\theta}_d$.

The angular distribution of $N(t^m, \bar{\theta}_\gamma)$ is expanded using Legendre polynomials as

$$\frac{\partial N}{\partial E_n^m}(E_n^m, \bar{\theta}_d) = c_0(E_n^m) + c_1(E_n^m) \cos \bar{\theta}_d + c_2(E_n^m) \frac{1}{2} (3 \cos^2 \bar{\theta}_d - 1). \quad (5.10)$$

The neutron energy dependence of c_0 , c_1 and c_2 corresponding to a_0 , a_1 and a_3 , respectively, are shown in Fig 5.15. It is found that c_1 and c_2 has a clear asymmetric and symmetric shape respectively such as a_1 and a_3 in Fig. 3.2.

Here, we define N_L and N_H to evaluate the angular dependence as

$$\begin{aligned} N_L(\theta_\gamma) &= \int_{E_p - 2\Gamma_p}^{E_p} \frac{\partial N}{\partial t^m}(t', \bar{\theta}_\gamma) dt^m \frac{dt^m}{dE} dE, \\ N_H(\theta_\gamma) &= \int_{E_p}^{E_p + 2\Gamma_p} \frac{\partial N}{\partial t^m}(t', \bar{\theta}_\gamma) dt^m \frac{dt^m}{dE} dE, \\ \frac{\partial N}{\partial E_n} &= \frac{dt^m}{dE_n} \frac{\partial N}{\partial t^m}. \end{aligned} \quad (5.11)$$

The angular dependence of N_L and N_H is shown in Fig. 5.17. As N_L and N_H have an angular dependence in Fig. 5.17, we define an asymmetry between N_L and N_H to evaluate the angular dependence of

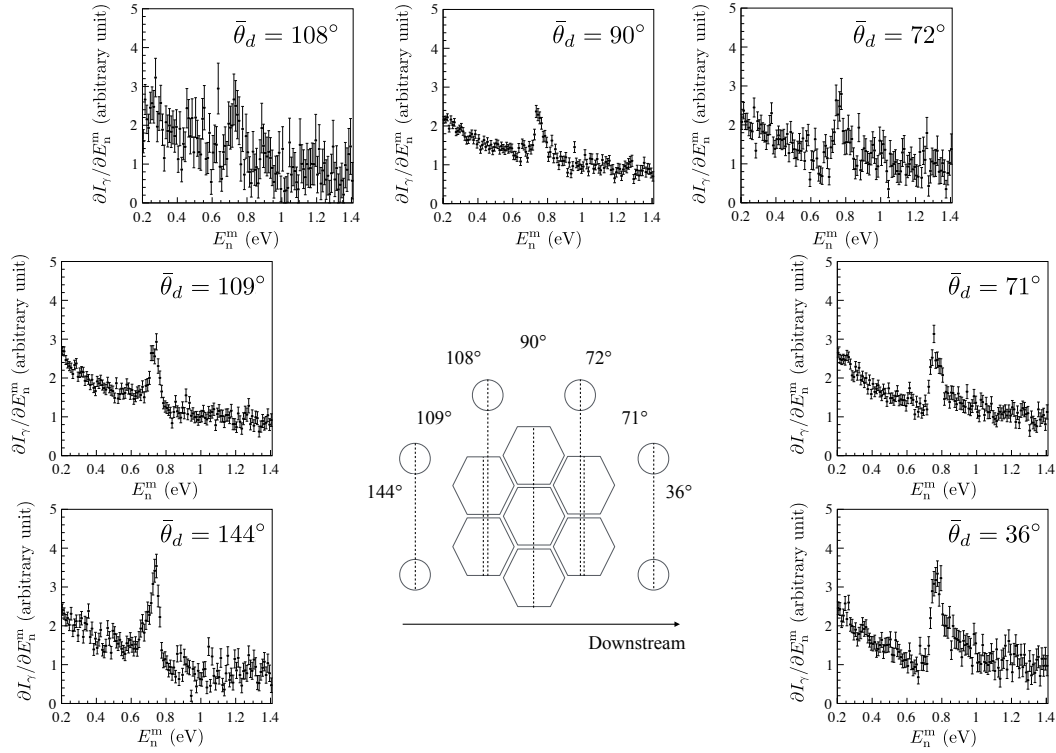


Figure 5.14: $\partial N/\partial t^m$ in the vicinity of p-wave resonance for each $\bar{\theta}_\gamma$. The central figure shows degrees in the direction of neutron momentum of the type-A detectors and the type-B detectors. The hexagons and the circles in the center of the figure denote each crystal of the type-A detector and the type-B detector, respectively. These are normalized with the number of the detectors in each angle. We can see that the peak shapes vary gradually.

the shape of the p-wave resonance as

$$A_{\text{LH}} = \frac{N_{\text{L}} - N_{\text{H}}}{N_{\text{L}} + N_{\text{H}}}. \quad (5.12)$$

The angular dependence of A_{LH} is shown in Fig. 5.18. The asymmetry A_{LH} has a correlation with $\cos \bar{\theta}_\gamma$ as

$$A_{\text{LH}} = (A \cos \bar{\theta}_\gamma + B), \quad (5.13)$$

where

$$A = -0.3881 \pm 0.0236, \quad B = -0.0747 \pm 0.0105, \quad (5.14)$$

which is a best fit result in Fig. 5.17. This non-zero value of A implies that there is a clear angular distribution of γ -rays from the p-wave resonance of ^{139}La to the ground state of ^{140}La . This angular distribution is discussed and interpreted in the context of s-p mixing in Section 6 and 7.

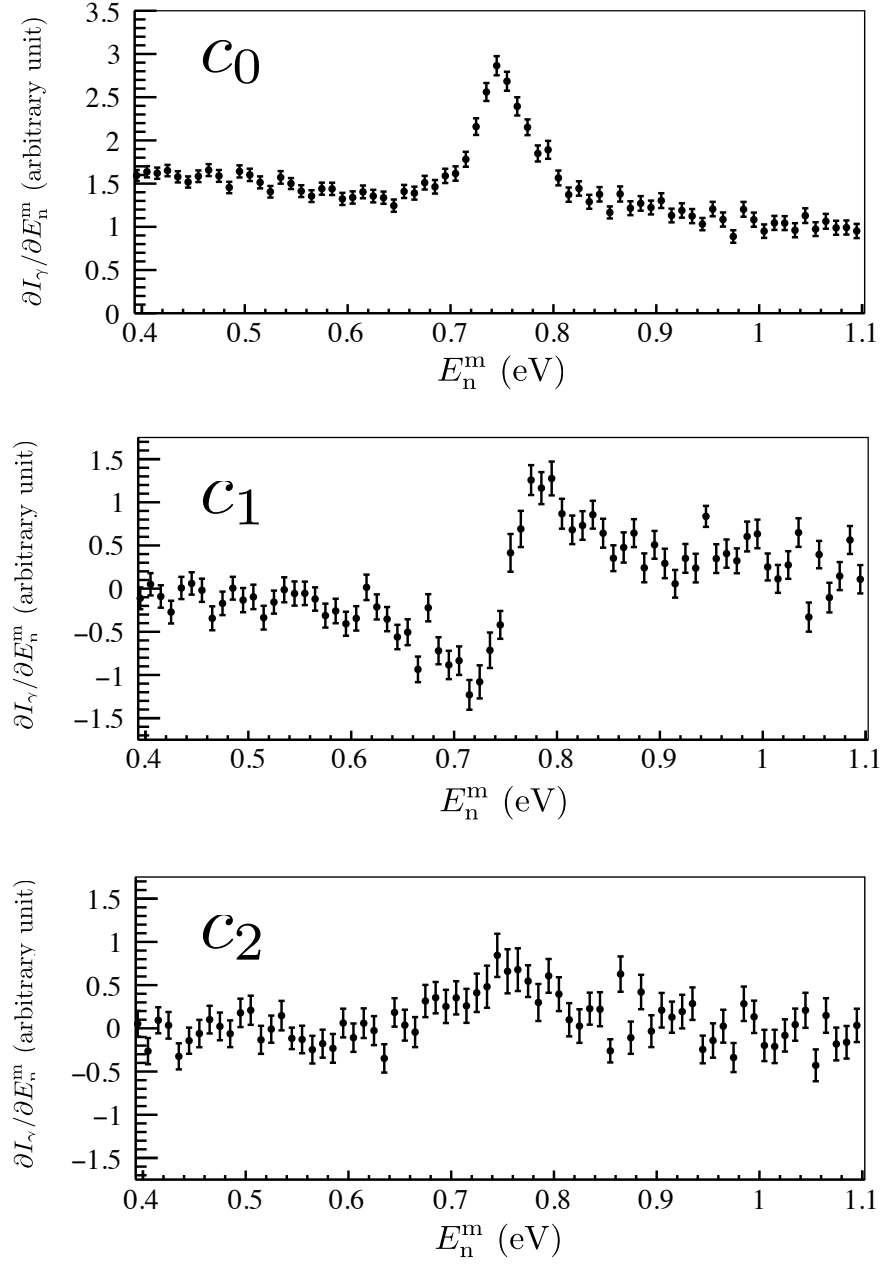


Figure 5.15: The neutron energy dependence of the Legendre polynomial c_0 , c_1 and c_2 . c_0 , c_1 and c_2 corresponds to a_0 , a_1 and a_3 respectively. It can clearly be seen that c_1 and c_2 have asymmetric and symmetric shapes respectively such as a_1 and a_3 in Fig. 3.2.

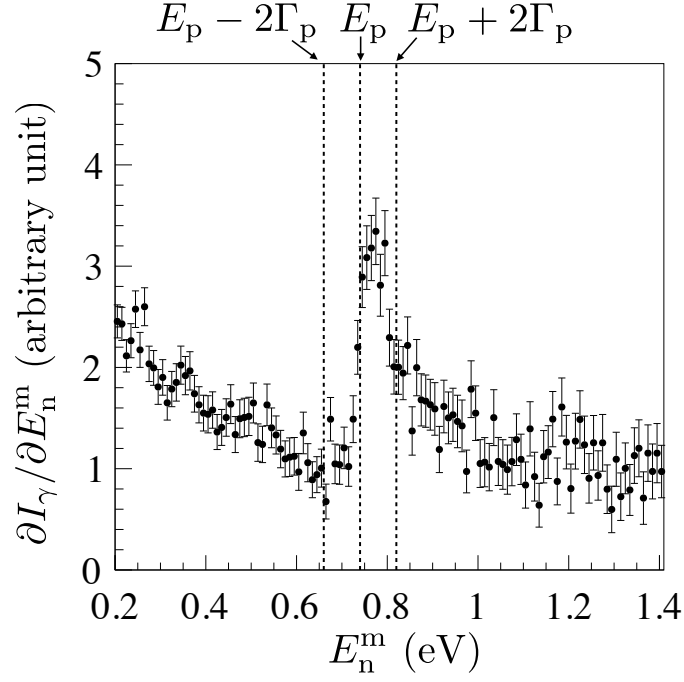


Figure 5.16: Visualization of the definition of N_L and N_H . N_L and N_H are defined as the number of events in the regions of $E_p - 2\Gamma_p \leq E_n^m \leq E_p$ and $E_p \leq E_n^m \leq E_p + 2\Gamma_p$ of the neutron spectrum, respectively.

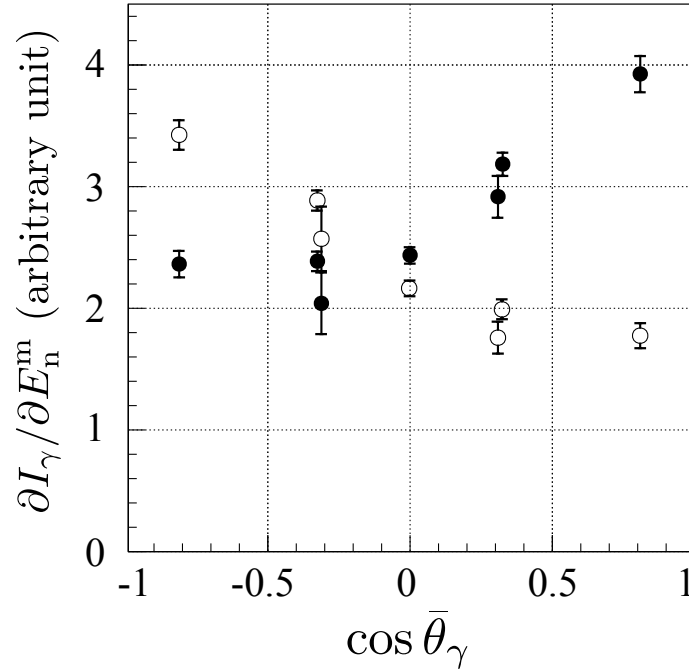


Figure 5.17: Angular dependences of N_L and N_H . The white points and black points show N_L and N_H , respectively.

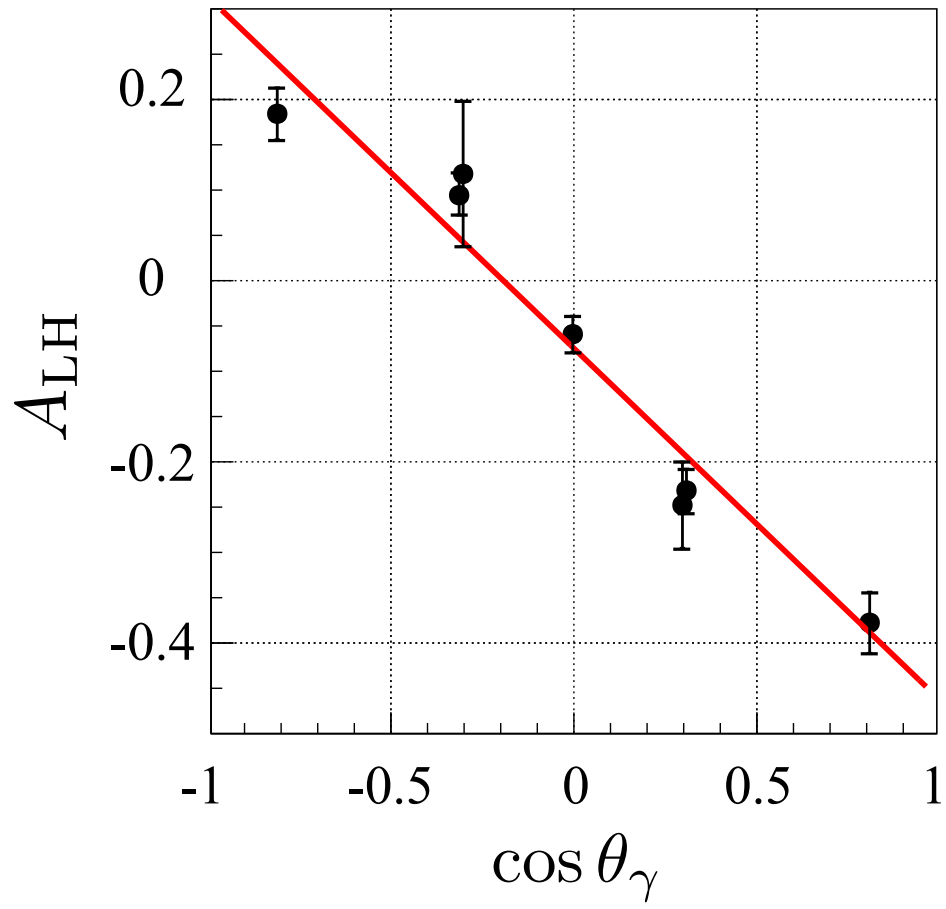


Figure 5.18: Angular dependences of A_{LH} with the fitting results of a linear function. It is found that A_{LH} has a clear angular dependence.

Chapter 6

Analysis

In this section, our experimental results from the previous section are analyzed by using the formalism of possible angular correlations of individual γ -rays emitted in (n, γ) reactions induced by low energy neutrons according to s-wave and p-wave amplitudes in order to determine ϕ , x and $\kappa(J)$.

6.1 Analysis to determine the partial γ width

The p-wave resonance and two neighboring s-wave resonances in the negative and positive energy region, listed in Table 6.1 are taken into account in the following analysis. The resonance energy and

r	E_r [eV]	J_r	l_r	Γ_r^γ [meV]	$g_r \Gamma_r^n$ [meV]	
1	-48.63	4	0	62.2	571.8	s ₁
2	0.7404 ± 0.002	4	1	40.41 ± 0.76	$(5.6 \pm 0.5) \times 10^{-5}$	p
3	72.30 ± 0.05	3	0	75.64 ± 2.21	11.76 ± 0.53	s ₂

Table 6.1: Resonance parameters of ^{139}La used in the analysis. $g_1 \Gamma_1^n$ is calculated from the reduced neutron width Γ_1^{n0} in Table 5.1.

resonance width measured in this work is used to the p-wave resonance ($r=2$) and the values in Ref. [49] for the negative resonance and positive s-wave resonance($r=1, r=3$). The compound nuclear spin of the negative s-wave resonance was determined as $J_1=4$ [49].

Figure 6.1 shows a comparison of γ -ray spectra gated in the vicinities of the negative s-wave resonance ($E_n^m = 0.2-0.4$ eV), the p-wave resonance ($E_n^m = 0.6-0.9$ eV) and the positive s-wave resonance($E_n^m = 70-75$ eV). As both negative s-wave and p-wave components were observed in the 5161 keV γ -ray peak, which is the transition to the ground state of ^{140}La whose spin is $F = 3$, the nuclear spin of the p-wave resonance is assumed to be the same as that of the negative s-wave resonance. This implies that $J_2=4$.

On the other hand, only the 5126 keV (transition to the $F = 5$ state) and 5131 keV (transition to the $F = 2$ state) γ -ray peak, which cannot be separated due to the energy resolution of the germanium detector, was observed in the γ -ray spectrum gated with the vicinity of the positive s-wave resonance,

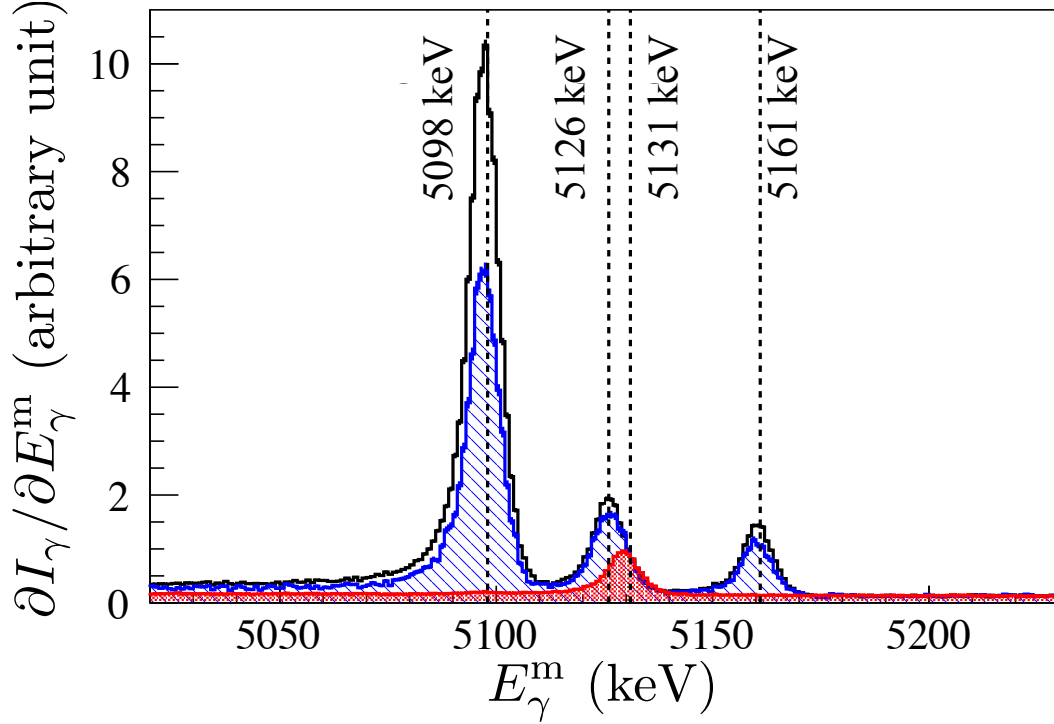


Figure 6.1: Comparison of the expanded $I_\gamma(E_\gamma^m)$ gated in the vicinities of s_1 -wave resonance ($E_n^m = 0.2$ - 0.4 eV: black line), the p-wave resonance ($E_n^m = 0.6$ - 0.9 eV: shaded area with diagonal line), and the s_2 -wave resonance ($E_n^m = 70$ - 75 eV : shaded area with dot).

and it is completely different from that of the negative s-wave resonance and p-wave resonance as shown in Fig. 6.1. Therefore the compound nuclear spin of the positive s-wave resonance is different from 4, and this means $J_3=3$.

The contributions of far s-wave resonances are assumed to be negligibly small, that is, $\alpha = 0$. In order to calculate the angular distribution theoretically, the ratios of the partial γ width Γ_{rf}^γ need to be determined for the three resonances. The ratios of the partial γ width from each resonance to the ground state can be obtained by a comparison of the peak height ratio of the neutron resonance gated in the 5161 keV photo-peak between s_1 -wave, p-wave, and s_2 -wave. Fig 6.2 is a TOF spectrum gated by the 5161 keV photo-peak with corrections for the neutron beam spectrum, the background γ -rays and the pile up of signals. The TOF spectrum is fitted by the following function of the p-wave resonance and the negative s-wave resonance using the formalism of the neutron capture cross section in Appendix A.

$$f(E_n^m) = \sigma_{s_1\gamma_{\text{gnd}}}(E_n^m) \frac{\Gamma_{s_1}^\gamma}{\Gamma_{s_1,\text{gnd}}^\gamma} P_{s_1} + \sigma_{p\gamma_{\text{gnd}}}(E_n^m) \frac{\Gamma_p^\gamma}{\Gamma_{p,\text{gnd}}^\gamma} P_p \quad (6.1)$$

Here P_{s_1} and P_p are fitting parameters and correspond to $\Gamma_{s_1,\text{gnd}}^\gamma/\Gamma_{s_1}^\gamma$ and $\Gamma_{p,\text{gnd}}^\gamma/\Gamma_p^\gamma$, respectively.

The ratios of the partial γ width from positive s_2 -wave resonance to the ground state are also obtained by a similar method. The measurement result taken using the lanthanum target with the thickness of 0.3 mm and neutron beam size of $\phi 15$ mm is used for this analysis because excess dead time occurred

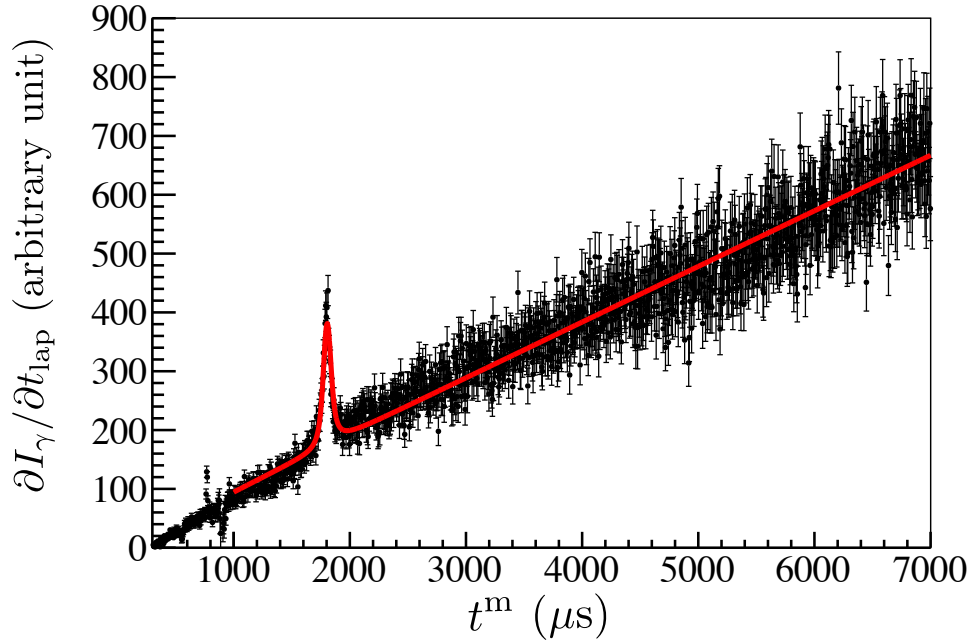


Figure 6.2: TOF spectrum gated with the 5161 keV photo-peak with corrections of neutron beam spectrum, background γ -rays and pile up of the signals. The solid line shows the best fit results. A dip at 900 μ s is a effect of the 2.99 eV resonance of ^{138}La .

in the positive s_2 -wave resonance due to its large cross section. Since it is difficult to fit the spectrum gated with the 5161 keV photo-peak due to the small statistics, the parameters of P_{s1} and P_{s2} , which are proportional to $\Gamma_{s1,\text{gnd}}^\gamma / \Gamma_{s1}^\gamma$ and $\Gamma_{s2,\text{gnd}}^\gamma / \Gamma_{s2}^\gamma$ respectively, are evaluated by the integral of the negative s_1 -wave resonance region and negative s_2 -wave resonance region. The ratio of P_p and P_{s2} to P_{s1} are obtained as

$$\frac{\Gamma_{s1,\text{gnd}}^\gamma}{\Gamma_{s1}^\gamma} : \frac{\Gamma_{p,\text{gnd}}^\gamma}{\Gamma_p^\gamma} : \frac{\Gamma_{s2,\text{gnd}}^\gamma}{\Gamma_{s2}^\gamma} = 1 : 0.796 \pm 0.020 : 0.009 \pm 0.006. \quad (6.2)$$

As shown in Fig. 6.1 and in Eq. 6.2, the branching ratio from the s_2 -wave resonance to the ground state is very small.

6.2 Analysis using the formalism of the differential cross section of γ -rays in $^{139}\text{La}(n,\gamma)$ reactions

The results of Eq 5.14 are analyzed using the formalism of the differential cross section of (n,γ) reactions. The formalism of the differential cross section of the $^{139}\text{La}(n,\gamma)$ reaction induced by unpolarized neutrons

can be written by using the resonance parameters in table 6.1 as follows.

$$\frac{d\sigma_{n\gamma f}}{d\Omega_\gamma} = \frac{1}{2} \left(a_0 + a_1 \cos \theta_\gamma + a_3 \left(\cos^2 \theta_\gamma - \frac{1}{3} \right) \right). \quad (6.3)$$

The negative s-wave amplitude V_1 , p-wave amplitude V_2 , and positive s-wave amplitude V_3 are given as

$$\begin{aligned} V_{1f} &= -\lambda_{1f} \left(\frac{|E_1|}{E_n} \right)^{\frac{1}{4}} \frac{\Gamma_1/2}{E_n - E_1 + i\Gamma_1/2}, \\ V_{2f} &= -\lambda_{2f} \left(\frac{E_n}{E_2} \right)^{\frac{1}{4}} \frac{\Gamma_2/2}{E_n - E_2 + i\Gamma_2/2}, \\ V_{3f} &= -\lambda_{3f} \left(\frac{E_3}{E_n} \right)^{\frac{1}{4}} \frac{\Gamma_3/2}{E_n - E_3 + i\Gamma_3/2}, \end{aligned} \quad (6.4)$$

where the absolute value of E_1 is adopted simply to avoid the imaginary neutron width.

The terms a_0 , a_1 , and a_3 can be written as

$$\begin{aligned} a_0 &= \lambda_{1f}^2 \sqrt{\frac{|E_1|}{E_n}} \frac{\Gamma_1^2/4}{(E_n - E_1)^2 + \Gamma_1^2/4} \\ &\quad + \lambda_{2f}^2 \sqrt{\frac{E_n}{E_2}} \frac{\Gamma_2^2/4}{(E_n - E_2)^2 + \Gamma_2^2/4} \\ &\quad + \lambda_{3f}^2 \sqrt{\frac{E_3}{E_n}} \frac{\Gamma_3^2/4}{(E_n - E_3)^2 + \Gamma_3^2/4} \\ a_1 &= \lambda_{1f} \lambda_{2f} \left(\frac{|E_1|}{E_2} \right)^{\frac{1}{4}} \\ &\quad \times \frac{\Gamma_1 \Gamma_2 (E_n - E_1)(E_n - E_2) + \Gamma_1^2 \Gamma_2^2/4}{2((E_n - E_1)^2 + \Gamma_1^2/4)((E_n - E_2)^2 + \Gamma_2^2/4)} \frac{5}{8} \left(-x + \sqrt{\frac{7}{5}} y \right) \\ &\quad + \lambda_{3f} \lambda_{2f} \left(\frac{E_3}{E_2} \right)^{\frac{1}{4}} \\ &\quad \times \frac{\Gamma_3 \Gamma_2 (E_n - E_3)(E_n - E_2) + \Gamma_3^2 \Gamma_2^2/4}{2((E_n - E_3)^2 + \Gamma_3^2/4)((E_n - E_2)^2 + \Gamma_2^2/4)} \frac{3\sqrt{3}}{8} \left(x + \sqrt{\frac{5}{7}} y \right) \\ a_3 &= \lambda_{2f}^2 \sqrt{\frac{E_n}{E_2}} \frac{\Gamma_2^2/4}{(E_n - E_2)^2 + \Gamma_2^2/4} \frac{33}{280} \left(-\sqrt{35} xy + y^2 \right). \end{aligned} \quad (6.5)$$

It can be assumed that the energy dependence of the neutron width of the r -th resonance is given as

$$\Gamma_r^n = (k_n R)^{2l_r} \sqrt{\frac{E_n}{1 \text{ eV}}} \Gamma_r^{nl_r} \quad (6.6)$$

where R is the radius of the target nuclei and Γ_r^{nl} is the reduced neutron width. This energy dependence is implemented as

$$\Gamma_r^n = \left(\frac{E_n}{|E_r|} \right)^{l_r + \frac{1}{2}} \overline{\Gamma}_r^n, \quad (6.7)$$

where $\overline{\Gamma}_r^n$ is a constant independent of the energy. As the phase shift due to the optical potential is negligibly small, each amplitude can be written as

$$V_{rf} = -\lambda_{rf} \left(\frac{E_n}{|E_r|} \right)^{\frac{l_r}{2} - \frac{1}{4}} \frac{\Gamma_r/2}{E_n - E_r + i\Gamma_r/2}, \quad (6.8)$$

where λ_{rf} is defined as

$$\lambda_{rf} = \frac{\hbar}{2} \sqrt{\frac{2g_r \overline{\Gamma}_r^n \Gamma_{rf}^\gamma}{m_n |E_r| \Gamma_r^2}}. \quad (6.9)$$

Γ_{rf}^γ is the γ -width from the r -th resonance to the final state.

We define

$$\begin{aligned} (\overline{a}_{0,1,3})_L &= \int_{E_p - 2\Gamma_p}^{E_p} dE' \int d^3p_A a_{0,1,3} \Phi(t^m, E', \mathbf{p}_A), \\ (\overline{a}_{0,1,3})_H &= \int_{E_p}^{E_p + 2\Gamma_p} dE' \int d^3p_A a_{0,1,3} \Phi(t^m, E', \mathbf{p}_A). \end{aligned} \quad (6.10)$$

Here, the a_3 term is ignored as it is proportional to λ_{2f}^2 and it is suppressed relative to the s-wave neutron width, according to the centrifugal potential by the factor $(kR)^2$. Under this approximation, Eq. 3.5 is reduced to

$$\frac{d\sigma_{n\gamma f}}{d\Omega_\gamma} = \frac{1}{2} (a_0 + a_1 \cos \theta_\gamma). \quad (6.11)$$

Substituting Eq. 6.11 into Eq. 5.8, the angular dependence of the γ -ray count in the neutron energy regions $E_p - 2\Gamma_p \leq E \leq E_p$ and $E_p \leq E \leq E_p + 2\Gamma_p$ can be written as

$$\left(\frac{\partial^2 I_\gamma}{\partial t^m \partial \Omega_\gamma} (t^m, \Omega_\gamma) \right)_{L,H} = \frac{I_0}{2} ((\overline{a}_0)_{L,H} + (\overline{a}_1)_{L,H} P_1(\cos \theta_\gamma)). \quad (6.12)$$

By convoluting with Eq. 5.9, the γ -ray count to be measured by the d -th detector can be written as

$$(I_{\gamma,d})_{L,H} = \frac{I_0}{2} ((\overline{a}_0)_{L,H} \overline{P}_{d,0} + (\overline{a}_1)_{L,H} \overline{P}_{d,1}). \quad (6.13)$$

As the energy dependence of x and y is negligibly small in the vicinity of the p-wave resonance ($r = 2$),

$(\overline{a_1})_{L,H}$ is a linear function of x and y , thus a function of ϕ . The value of ϕ is determined by comparing $((I_{\gamma,d})_L - (I_{\gamma,d})_H) / ((I_{\gamma,d})_L + (I_{\gamma,d})_H)$ with the measured values A_{LH} in Eq. 5.14.

$$\begin{aligned} \frac{(I_{\gamma,d})_L - (I_{\gamma,d})_H}{(I_{\gamma,d})_L + (I_{\gamma,d})_H} &= \frac{(\overline{a_1})_L - (\overline{a_1})_H}{(\overline{a_0})_L + (\overline{a_0})_H} \\ &= 0.295 \cos \phi - 0.345 \sin \phi \\ &= 0.295x - 0.345y. \end{aligned} \quad (6.14)$$

Two solutions can be obtained as

$$\phi = (99.2^{+6.3}_{-5.3})^\circ, \quad (161.9^{+5.3}_{-6.3})^\circ. \quad (6.15)$$

We also obtain x from Eq. 6.15 as

$$x = -0.16^{+0.09}_{-0.11}, \quad -0.95^{+0.03}_{-0.04}. \quad (6.16)$$

To visualize the solutions, Eq. 6.14 is drawn in the xy -plane and the crossing points of the Eq. 6.14 and a unit circle imply the solutions.

The value of W , which is given in Eq. 2.7, is also obtained as

$$W = (13.2^{+18.1}_{-5.3}) \text{ meV}, \quad (2.21^{+0.10}_{-0.06}) \text{ meV}. \quad (6.17)$$

The published value of $A_L = (9.56 \pm 0.35) \times 10^{-2}$ in Ref. [64] and the parameters in Table. 5.1 are used in the calculation.

The $J = I + \frac{1}{2}$ case corresponds to the p-wave of the ^{139}La at $E = E_2$. Finally, the value of $|\kappa(J)|$ corresponding to the ϕ obtained is determined as

$$\kappa(J) = 4.84^{+5.58}_{-1.69}, \quad 0.99^{+0.08}_{-0.07}, \quad (6.18)$$

and $|\kappa(J)|$ is shown in Fig. 6.4. The experimental sensitivity for the T-violation search is discussed using this $\kappa(J)$ of ^{139}La in Section 7.3.

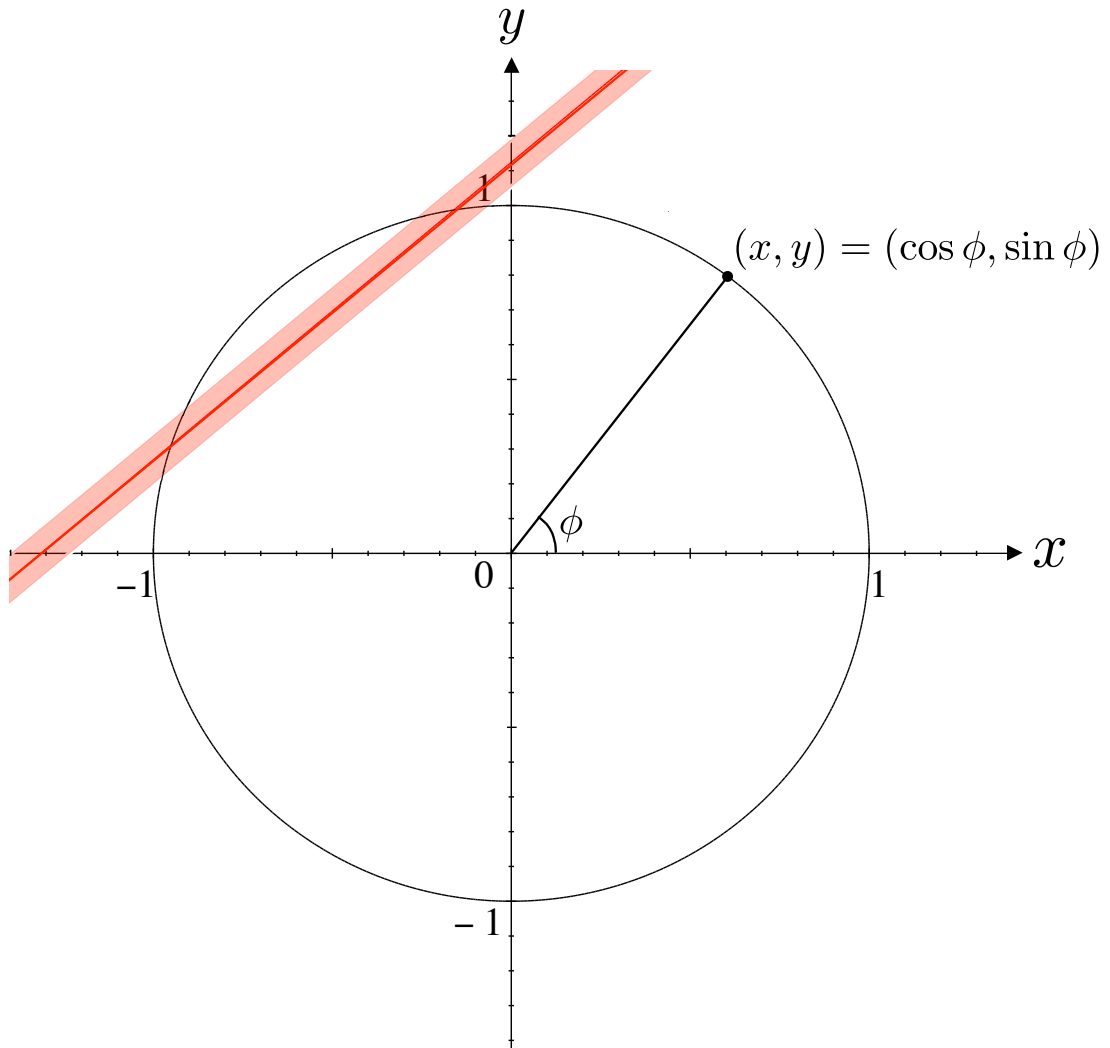


Figure 6.3: Visualization of the value of ϕ on the xy -plane. The solid line and shaded area show the central values of ϕ and the 1σ area, respectively. The angle of a point on a unit circle denotes ϕ . The crossing point of the red line shows the solutions.

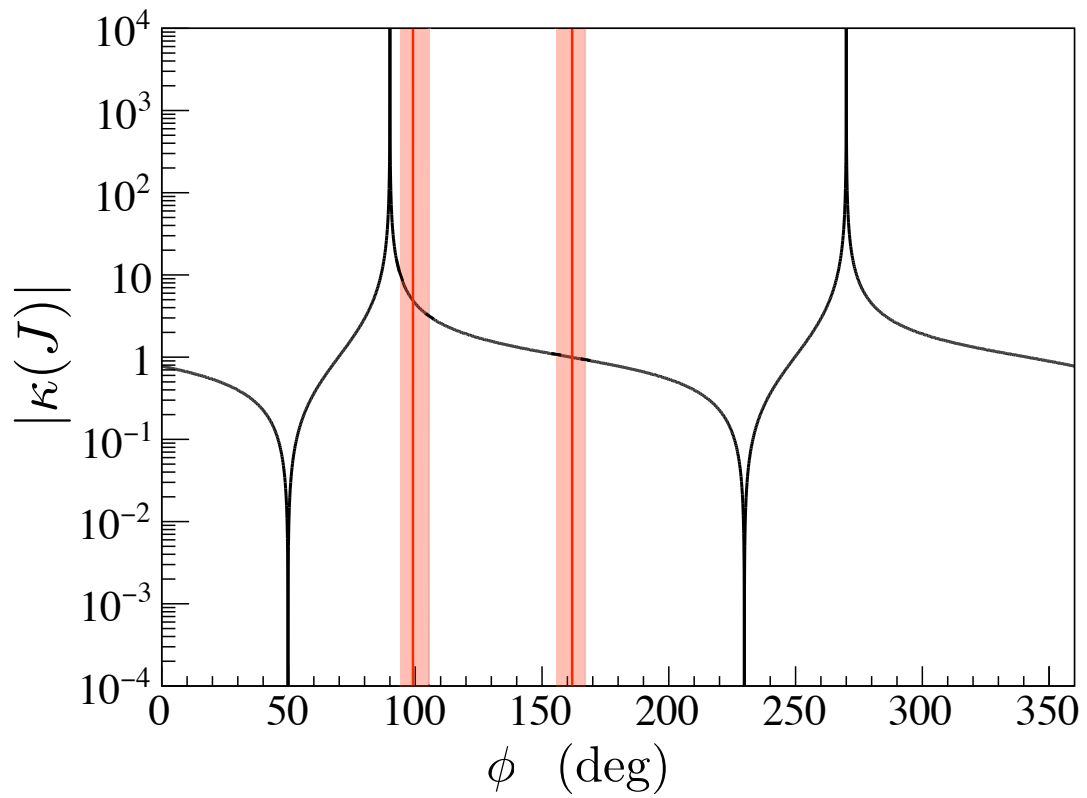


Figure 6.4: Value of $|\kappa(J)|$ as a function of ϕ . The solid line and shaded area show the central values of ϕ and the 1σ area from the central value, respectively.

Chapter 7

Discussion

The important parameter $\kappa(J)$ necessary in order to evaluate the sensitivity of the T-violation search was determined in the previous section. In this section, a more detailed analysis, an additional experimental study of the (n, γ) reaction and the estimation of the T-violation sensitivity are described.

7.1 More detailed analysis

The a_3 term was ignored in the analysis in the previous chapter since the centrifugal potential of the p-wave resonance is small. Hereafter the case that the a_3 term in Eq. 3.5 is activated is discussed in this section.

As the a_3 term has the symmetric shape as shown in Fig. 3.2, it can be evaluated using the angular dependence of $N_L + N_H$. The angular dependences of $N_L - N_H$ and $N_L + N_H$ are shown in Fig. 7.1. The a_1 and a_3 term should be described as the first and the second polynomial function of $\cos \bar{\theta}_\gamma$, respectively, as shown in Eq. 3.11, and therefore the angular dependences of $N_L - N_H$ and $N_L + N_H$ are analyzed and fitted by the functions of $f(\bar{P}_{d,1}/\bar{P}_{d,0}) = A'\bar{P}_{d,1}/\bar{P}_{d,0} + B'$ and $g(\bar{P}_{d,2}/\bar{P}_{d,0}) = C'\bar{P}_{d,2}/\bar{P}_{d,0} + D'$, respectively, with fitting parameters A' , B' , C' , and D' . The theoretical calculation of the a_3 term can be written as

$$\begin{aligned}\frac{A'}{D'} &= \frac{(\bar{a}_1)_L - (\bar{a}_1)_H}{(\bar{a}_0)_L + (\bar{a}_0)_H} \\ &= 0.295 \cos \phi_2 - 0.345 \sin \phi_2 \\ &= 0.295x - 0.345y,\end{aligned}\tag{7.1}$$

$$\begin{aligned}\frac{C'}{D'} &= \frac{(\bar{a}_3)_L + (\bar{a}_3)_H}{(\bar{a}_0)_L + (\bar{a}_0)_H} \\ &= -0.295 \cos \phi_2 \sin \phi_2 + 0.050 \sin^2 \phi_2 \\ &= -0.295xy + 0.050y^2.\end{aligned}\tag{7.2}$$

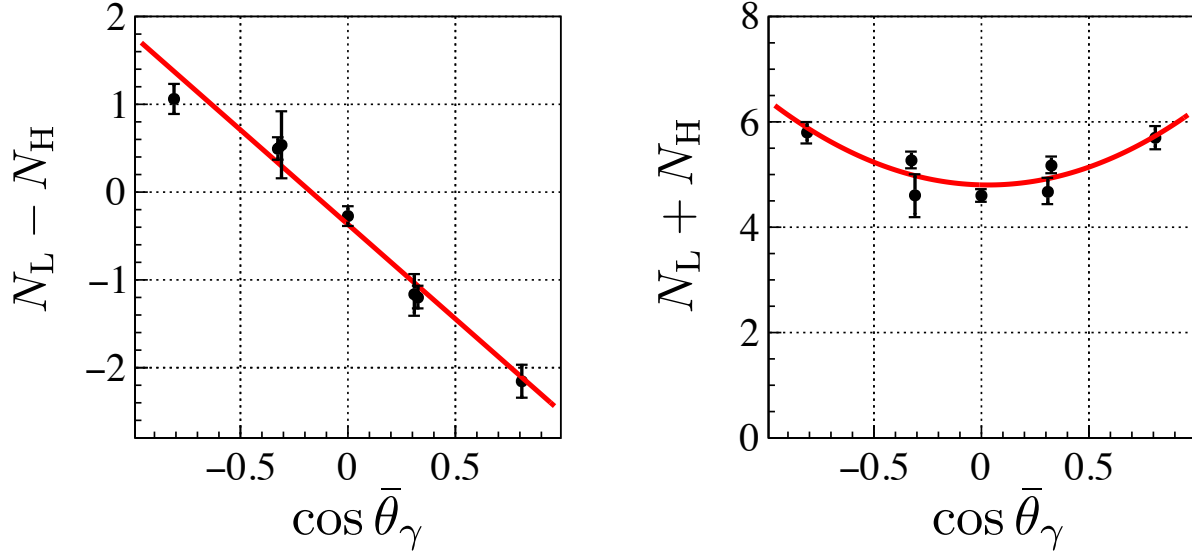


Figure 7.1: Angular dependences of $N_L - N_H$ and $N_L + N_H$. The solid line indicates the best fit.

The fitted results of C'/D' and A'/D' are

$$\frac{A'}{D'} = -0.409 \pm 0.024, \quad \frac{C'}{D'} = 0.191 \pm 0.028. \quad (7.3)$$

The equations of x and y of a_1 (Eq. 7.1) and a_3 (Eq. 7.2) are drawn on the xy -plane as shown in Fig. 7.2, and the value of ϕ is determined by combining the two equations. The restriction from the a_3 term is not consistent with that of the a_1 term. The a_3 term deviates from the requirement of $x_1^2 + y_1^2 = 1$ by more than 2σ .

In this analysis, $J_1 = J_2 = 4, J_3 = 3$ are assumed. However, there is a possibility of the case of $J_1 = J_2 = J_3 = 3$. As the effect of the s_2 -wave is negligibly small in this discussion, we discuss combinations of J_1 and J_2 only. The result of the case of $J_1 = J_2 = J_3 = 3$ is shown in Fig. 7.3. As both a_1 and a_3 in the case of $J_1 = J_2 = J_3 = 3$ have no solution and a_1 and a_3 in the case of $J_1 = J_2 = 4, J_3 = 3$ have a solution within 3σ , $J_1 = J_2 = 4$ may be correct.

The origin of the inconsistency has not been identified in the present study. The inconsistency may be due to possible incompleteness of the reaction mechanism based on the interference between s- and p-wave amplitudes using the Breit–Wigner approximation.

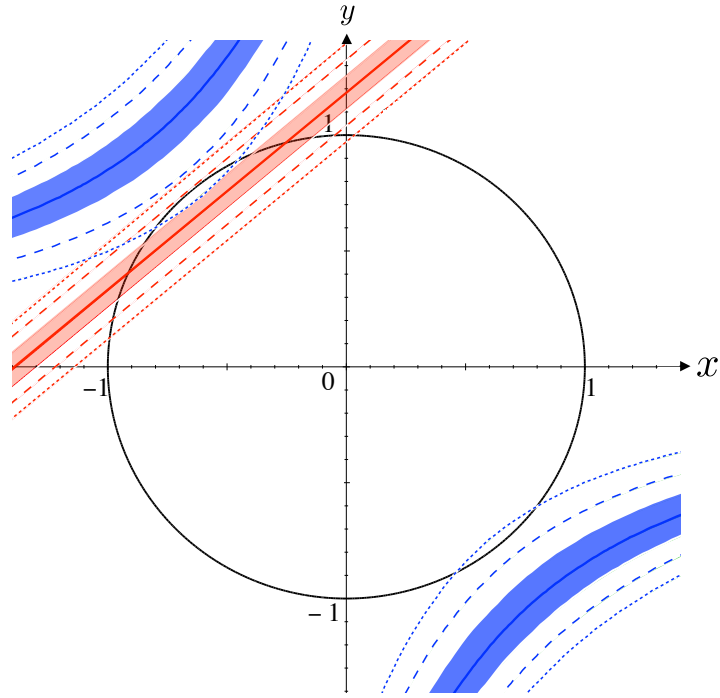


Figure 7.2: a_1 (straight lines) and a_3 (curved lines) on the xy -plane for the cases of $J_1 = J_2 = 4, J_3 = 3$. The solid line, shaded area, dashed line, and dotted line show the central values of ϕ , 1σ areas, 2σ contours and 3σ contours, respectively.

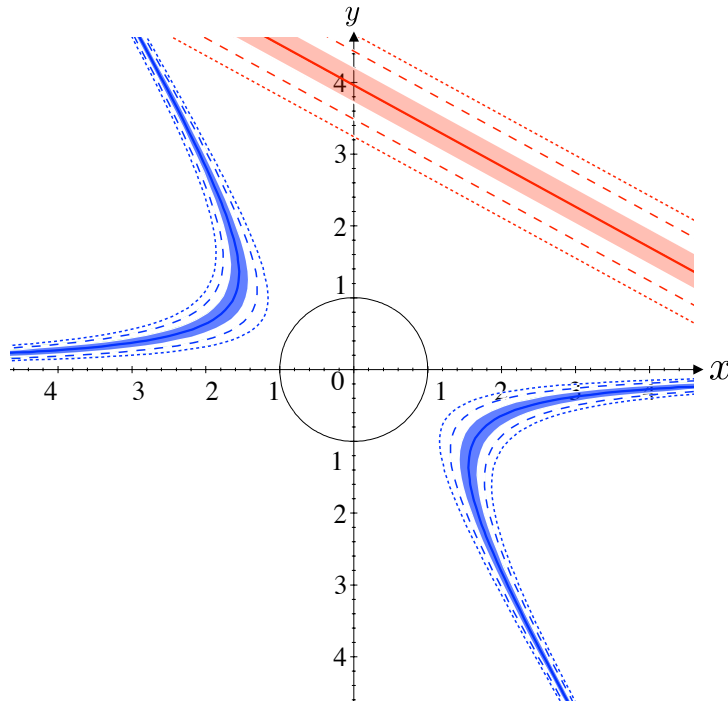


Figure 7.3: a_1 (straight lines) and a_3 (curved lines) on the xy -plane in the case of $J_1 = J_2 = J_3 = 3$. The solid line, shaded area, dashed line, and dotted line show the central values of ϕ_2 , 1σ areas, 2σ contours and 3σ contours, respectively.

7.2 Further analysis and experiments for the (n,γ) reaction

In our experiment and analysis, a_1 and a_3 terms in Eq. 3.4 were measured in the transition to the ground state and x was determined. We can predict other a terms of Eq. 3.5 for any final state by using the obtained value of ϕ .

In order to confirm the obtained value of ϕ and verify the formalism of the s-p mixing, further analysis using other final states, for example 29.96 keV and 34.65 keV excited state corresponding to the γ -ray peak of 5126 keV and 5131 keV in Fig. 6.1, can be performed using the data obtained in the experiment with the same analysis method of the transition to the ground state.

As an additional experiment, measurements of other a terms in Eq. 3.4 can be also performed using a polarized neutron beam in order to eliminate the one of the solutions of Eq. 6.16. This can make further investigation of the formalism of the s-p mixing in a compound nucleus possible. The energy dependence of these terms can be calculated by using the value of x obtained in the previous section as shown in Fig. 7.4 for $F = 3$, $F = 4$ and $F = 5$ final states. The two values are obtained in each a term in Fig. 7.4 due to the two solutions of x . We can distinguish which value of x is correct by measuring other terms. As it is difficult to measure the circular polarization of emitted γ -rays from the target nucleus, terms that do not include σ_γ should be measured. The largest term which does not include σ_γ is a_2 for the $F = 3$ final state. This term can be evaluated by measuring the angular distribution of γ -rays from an incident vertically polarized neutron beam with respect to the neutron momentum axis. The value of x can then be determined finally by measuring the a_2 term.

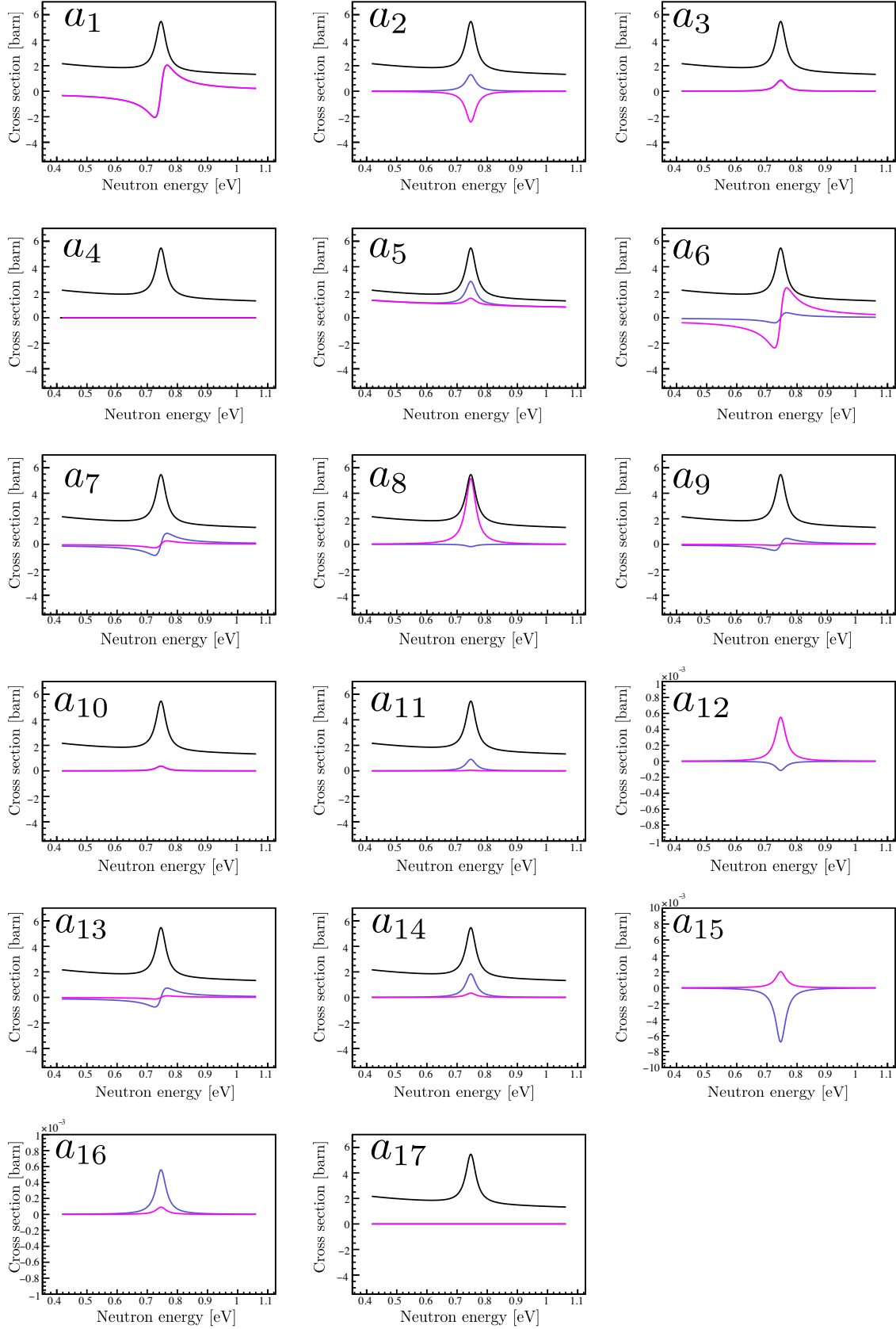


Figure 7.4: Neutron energy dependences of a_0 - a_{17} in $^{139}\text{La}(n,\gamma)$ reactions to the $F = 3$ final state using obtained x . The blue lines and pink lines show the calculated results using the solutions of $x = -0.16$ and $x = -0.95$, respectively.

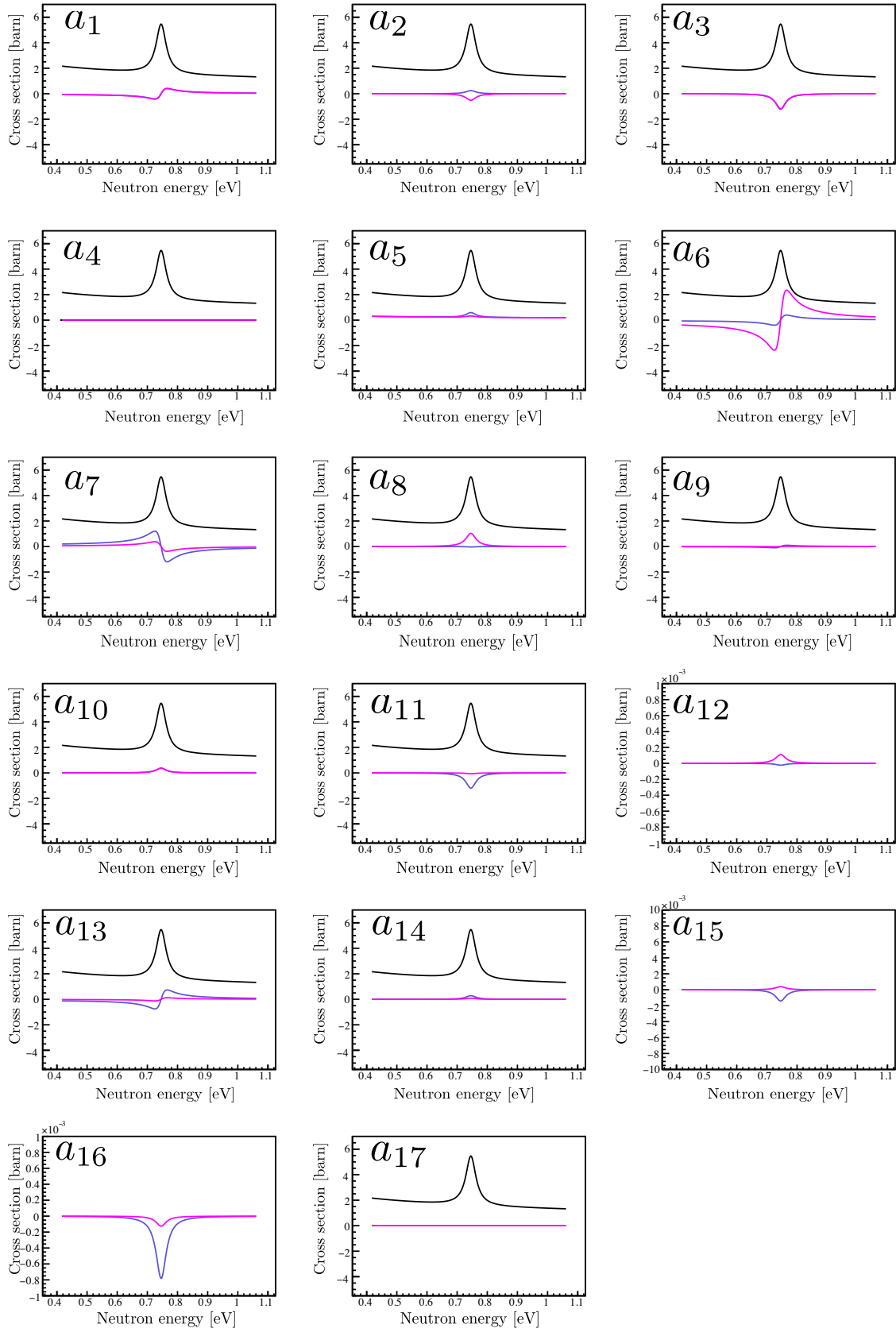


Figure 7.5: Neutron energy dependences of a_0 - a_{17} in $^{139}\text{La}(n,\gamma)$ reactions to the $F = 4$ final state using obtained x . The blue lines and pink lines show the calculated results using the solutions of $x = -0.16$ and $x = -0.95$, respectively.

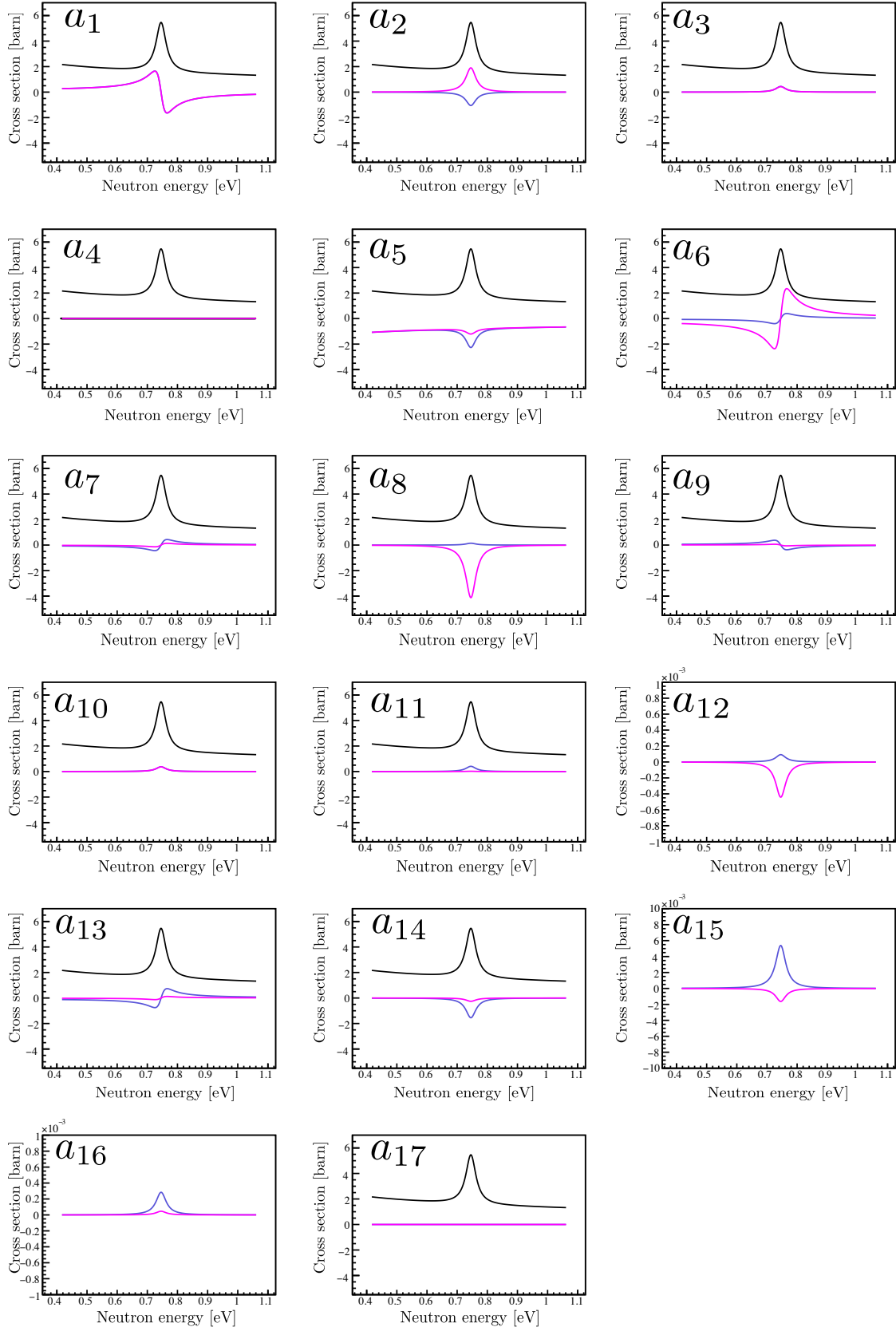


Figure 7.6: Neutron energy dependences of a_0 - a_{17} in $^{139}\text{La}(n,\gamma)$ reactions to the $F = 5$ final state using obtained x . The blue lines and pink lines show the calculated results using the solutions of $x = -0.16$ and $x = -0.95$, respectively.

7.3 Estimation of the sensitivity for the T-violation search

The sensitivity for the T-violation search with ^{139}La can be estimated by using the formalism described in Section 2.3 due to the determination of $\kappa(J)$. Since about 50% nuclear polarization has been achieved with LaAlO_3 , we assume the case for using the LaAlO_3 crystal as the nucleus target. First of all, the current upper limit of the W_T/W is needed to be estimated in Eq. 2.14.

7.3.1 Estimation of the upper limit of the W_T/W

The upper limit of the ratio of the T-violating weak matrix element to P-violating weak matrix element in the nucleon nucleon interaction in the compound nucleus W_T/W is estimated using the current upper limit of the EDM searches. The ratio of the T-odd P-odd cross section $\Delta\sigma^{\text{TP}}$ to the P-odd cross section $\Delta\sigma^{\text{P}}$ in neutron-deuteron scattering was calculated using the meson-exchange model of Effective Field Theory (EFT) by Y. H. Song. et. al [65]. We assume that the ratio is equal to W_T/W as

$$\frac{W_T}{W} = \frac{\Delta\sigma^{\text{TP}}}{\Delta\sigma^{\text{P}}} \simeq (-0.47) \left(\frac{\bar{g}_\pi^{(0)}}{h_\pi^1} + (0.26) \frac{\bar{g}_\pi^{(1)}}{h_\pi^1} \right). \quad (7.4)$$

Here, $\bar{g}_\pi^{(0)}$ and $\bar{g}_\pi^{(1)}$ are isoscalar and isovector time reversal invariant meson-nucleon coupling constants, and h_π^1 is a P-violating meson exchange coupling constant, where the superscript denotes the isospin change for the process. The upper limits of $\bar{g}_\pi^{(0)}$ and $\bar{g}_\pi^{(1)}$ are estimated from the n-EDM and ^{199}Hg -EDM search respectively as

$$\bar{g}_\pi^{(0)} < 2.5 \times 10^{-10}, \quad \bar{g}_\pi^{(1)} < 0.5 \times 10^{-11} \text{ [65]}. \quad (7.5)$$

The value of h_π^1 was obtained from the measurement of the P-violation of $n + p \rightarrow d + \gamma$ reactions as

$$h_\pi^1 = (3.04 \pm 1.23) \times 10^{-7} \text{ [66]}. \quad (7.6)$$

However, since this value is a preliminary result, it may change.

W_T/W is calculated using Eq 7.4, Eq. 7.5 and Eq. 7.6 as

$$\left| \frac{W_T}{W} \right| < 3.9 \times 10^{-4}. \quad (7.7)$$

The T-violating cross section in the 0.74 eV p-wave resonance of ^{139}La can be estimated using Eq 2.14 as

$$\begin{aligned} |\Delta\sigma_T| &= \kappa(J) \left| \frac{W_T}{W} \right| \Delta\sigma_P, \\ \rightarrow |\Delta\sigma_T| &< 1.0 \times 10^{-4} \text{ barn}. \end{aligned} \quad (7.8)$$

Here, the value of $\kappa(J) = 0.99$, which is a pessimistic case, and $\Delta\sigma_P = 0.3 \text{ barn}$ is used. .

7.3.2 Estimation of the forward scattering amplitude and an optimum target thickness

In order to calculate the experimental sensitivity ($8\text{Re}A^*D$), the coefficients of the forward scattering amplitude A' , C' and D' in Eq. 2.18 are estimated as follows.

A' can be estimated from the neutron capture cross section. From the optical theorem, the imaginary part of A' can be written as

$$\begin{aligned}\text{Im}A' &= \frac{k}{4\pi}(\sigma_{\text{abs}} + \sigma_{\text{scat}}) \\ &= 6.34 \times 10^{-2} \text{ fm.}\end{aligned}\tag{7.9}$$

The imaginary part of C' can be estimated from the P-violation. Since the ratio of the P-violating cross section to the total cross section is 2%, the imaginary part of C' can be estimated as

$$\begin{aligned}\frac{\text{Im}C'}{\text{Im}A'} &= 0.02, \\ \rightarrow \text{Im}C' &= 1.25 \times 10^{-3} \text{ fm.}\end{aligned}\tag{7.10}$$

The imaginary part of D' can be calculated by using C' and Eq. 2.14 as

$$\begin{aligned}\text{Im}D' &= \kappa(J) \frac{W_T}{W} \text{Im}C', \\ \rightarrow |\text{Im}D'| &< 4.83 \times 10^{-7} \text{ fm.}\end{aligned}\tag{7.11}$$

Here the value of $\kappa(J) = 0.99$ and $|W_T/W| < 3.9 \times 10^{-4}$ are used.

The magnitude of b in Eq. 2.21 implies the rotation of the incident neutron spin by pseudo magnetism and the experimental sensitivity decreases by this spin rotation. We therefore assume that the spin rotation from pseudo magnetism is canceled by applying an external magnetic field. This means $\text{Re}b = 0$. By using the coefficients of the forward scattering amplitudes, we can calculate the experimental sensitivity $8\text{Re}A^*D$ and the target thickness dependence of experimental sensitivity is shown in Fig. 7.7. The optimum thickness is 6.6 cm and the maximum experimental sensitivity is 1.1×10^{-5} .

7.3.3 Experimental setup

The optimum target thickness was determined as 6.6 cm in the context of the T-violation sensitivity. We are planing an experiment to search for T-violation on a neutron beam line at MLF in J-PARC. In this section, the measurement time to exceed the current upper limit of the T-violation is estimated.

We assume that a beam line where a poisoned moderator is equipped is used and the target is installed at 15 m from the moderator surface. The ways to measure the polarization P_x and the analyzing power A_x are shown in Fig. 7.8 and Fig. 7.9, respectively. If we eliminate the current limit of the T-violation

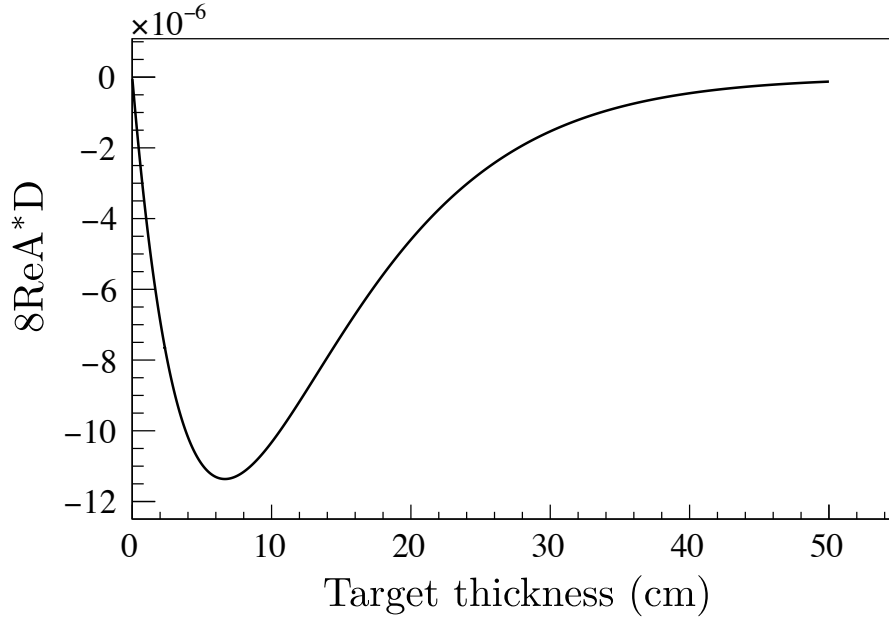


Figure 7.7: Target thickness dependence of experimental sensitivity. The optimum thickness is 6.6 cm and the maximum experimental sensitivity is 1.1×10^{-5} .

by the n-EDM search with 95% C.L., the error of A_x : ΔA_x and the error of P_x : ΔP_x need to satisfy following condition.

$$1.96\sqrt{\Delta A_x^2 + \Delta P_x^2} < 8\text{Re}A^*D. \quad (7.12)$$

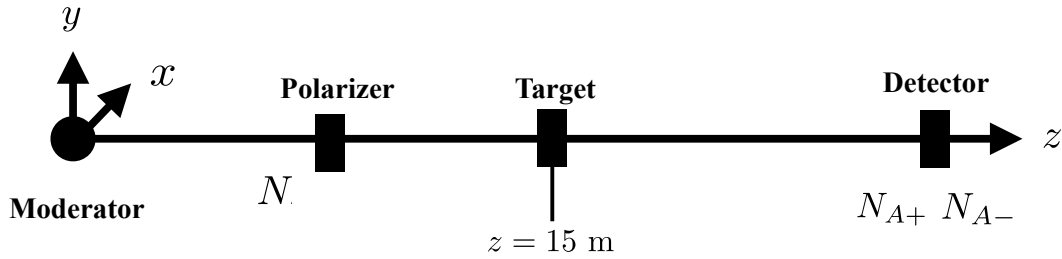
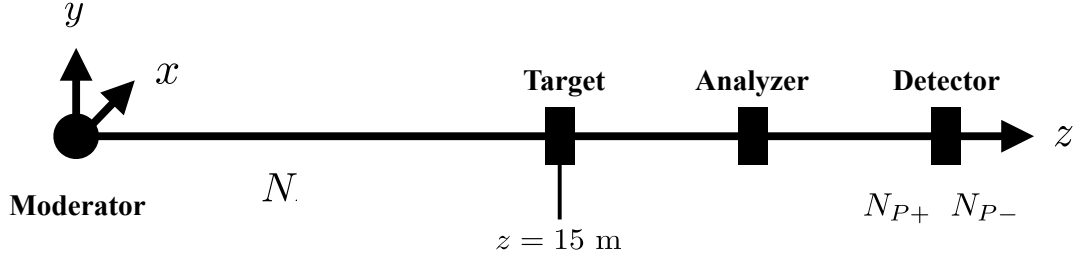


Figure 7.8: Experimental setup to measure A_x

The incident neutron intensity is defined as N . The number of the transmitted neutrons for plus (minus) polarized polarizer and pulse (minus) polarized analyzer are defined as N_{P+} (N_{P-}) and N_{A+} (N_{A-}), respectively. A_x and ΔA_x can be written as

$$A_x = \frac{N_{A+} - N_{A-}}{N_{A+} + N_{A-}}, \quad \Delta A_x = \frac{2\sqrt{N_{A+}^3 + N_{A-}^3}}{(N_{A+} + N_{A-})^2}. \quad (7.13)$$

Figure 7.9: Experimental setup to measure P_x

P_x and ΔP_x can be written as

$$P_x = \frac{N_{P+} - N_{P-}}{N_{P+} + N_{P-}} \frac{T}{\sqrt{T^2 - T_{00}^2}}, \quad \Delta P_x = \frac{2\sqrt{N_{P+}^3 + N_{P-}^3}}{(N_{P+} + N_{P-})^2} \frac{T}{\sqrt{T^2 - T_{00}^2}}. \quad (7.14)$$

Here, T_{00} and T are transmission for the unpolarized and polarized polarizer, respectively.

Assuming that the target area is $4 \text{ cm} \times 4 \text{ cm}$ and a neutron beam of $0.74 \text{ eV} \pm 0.05 \text{ eV}$ is used, the intensity of the neutron beam at the target position with a beam power of 1 MW is estimated using the Monte-Carlo simulation [67] as $1.8 \times 10^7 \text{ n/s}$.

We are planning to use following experimental techniques to carry out the experiments.

Neutron polarizer

A neutron polarizer is a device used to polarize a neutron beam and used as the polarizer and analyzer in Fig. 7.8 and Fig. 7.9. A ^3He spin filter and proton spin filter are available to polarize epithermal neutrons. Both devices utilize a spin dependence of cross section between the nucleus and neutron, and therefore a neutron beam is polarized passing through the devices.

A proton spin filter is a polarized proton target typically made from ethylene glycol, butanol, propanediol and NH_3 using the dynamic nuclear polarization method. The scattering cross sections of the proton to parallel spin and anti-parallel spin neutrons are 3.7 barn and 37 barn, which are almost constant for $E_n = 0 - 10^5 \text{ eV}$, and this 10 times difference of the cross sections can be used to polarize the neutron beam for wide energy range. Although high polarization of protons ($\sim 90\%$) has been achieved and highly polarized neutron beam (over 70%) can be provided, a very low temperature ($\sim 1 \text{ K}$) and high magnetic field ($\sim 3 \text{ T}$) are needed for the dynamic nuclear polarization method. Additionally the scattered neutron beam can be a background for the experiment. Recently, a triplet DNP method, which can be used to polarized protons in higher temperature (over 77 K) and lower magnetic field ($\sim 0.1 \text{ T}$), was developed, and is expected to be a new method for a neutron polarizer.

^3He spin filter is composed of polarized ^3He gas and alkali metal encapsulated into a special glass cell. This glass cell is made from GE180 or quartz, which does not include boron. ^3He has a very large absorption cross section (10666 barn) for anti-parallel neutrons; nevertheless the absorption cross section for parallel neutrons is approximately zero. The neutron beam can be polarized using this property, and it is

advantageous as a neutron polarizer for avoiding the background caused by scattering neutron. However, since the neutron absorption cross section decreases according to the $1/v$ law, it is difficult to obtain high polarization for high energy neutrons. The ^3He is polarized by Spin Exchange Optical Pumping (SEOP) method. The peripheral electron of Rb atoms, which are also enclosed in the glass cell, are polarized by the circular light, and the polarization is transferred to ^3He nuclei by hyper fine interactions. Recently, high polarization of ^3He was achieved by mixing potassium in addition to rubidium, that is called as Hybrid SEOP method. The quality of the ^3He spin filter is evaluated by the polarization of ^3He and quantity of the ^3He gas, which is describe by the product of length and pressure, and its unit is atm·cm. The details of the ^3He spin filter are summarized in Ref [68].

^3He spin filter is better for polarizing neutrons at $E_n = 0.74$ eV. The figure of merit (FOM) can be defined to optimize the quality of ^3He spin filter as

$$\text{FOM} = PT^2, \quad (7.15)$$

where P and T are the polarization and transmission of the neutron beam, respectively. In the case that 70% polarization of ^3He is obtained, T , P and therefore FOM depend on the quantity of ^3He gas as shown in Fig. 7.10. FOM is maximum when the quantity of ^3He spin filter is 79 atm·cm. In this case, the

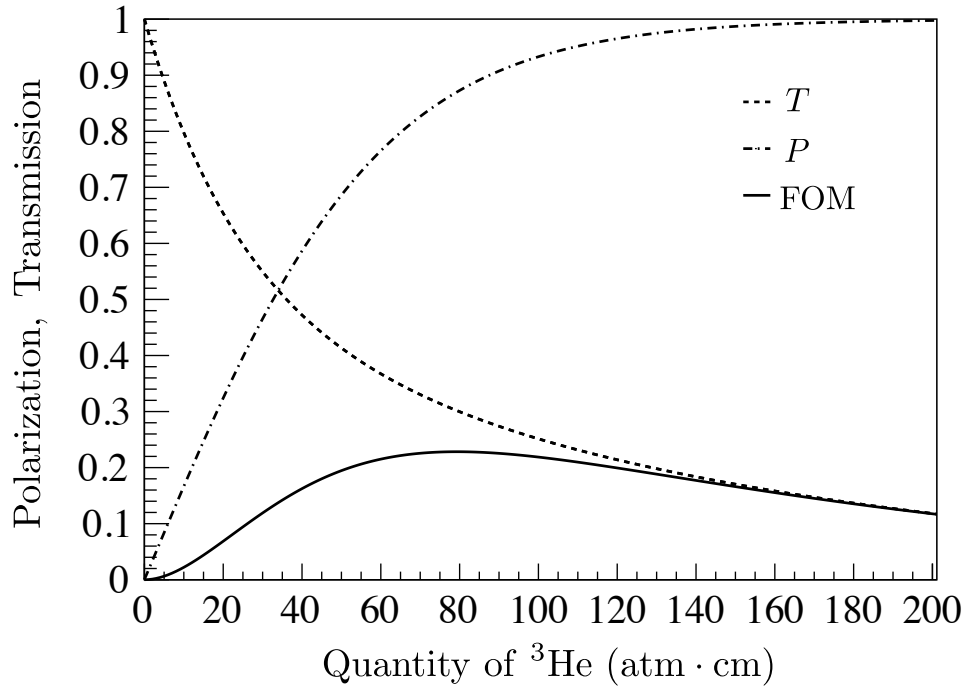


Figure 7.10: Polarization, transmission and FOM of ^3He spin filter at 70% polarization of ^3He for neutron at $E_n = 0.74$ eV.

polarization and the transmission of the neutron beam are 87% and 30%, respectively. In order to keep high polarization of ^3He , a highly uniform magnetic field which is a few gauss and laser system whose power is over 100 W need to be developed and installed on the beam line.

Neutron detector

^{10}B -loaded liquid scintillator has been commonly used to detect neutrons in eV region. In order to measure the tiny asymmetry, very high statistics needs to be obtained, and a neutron detector which can count the neutrons with a rate of approximately 1 Gcps/cm² is desirable. One of the candidate detectors is a segmented ^{10}B -loaded liquid scintillator. Very high counting rates can be achieved using it due to a fast decay time of the detector signal and segmentation. Moreover, since γ -rays can be background for the measurement, neutron and γ -ray discrimination is also important. The discrimination can be performed by using the pulse shape difference between the neutron and the γ -ray detection.

Polarization of the target

The polarization of ^{139}La has been studied with $\text{La}_2\text{Mg}_3(\text{NO}_3)_{12} \cdot 24\text{H}_2\text{O}$, F_3La and LaAlO_3 using the dynamic nuclear polarization method. The highest polarization (Approximately 50%) was achieved using neodymium doped LaAlO_3 crystal with dimensions of $15 \times 15 \times 4 \text{ mm}^3$ by applying a magnetic field of 2.35 T and a temperature below 0.3 K at ILL [46].

In order to polarize the nucleus, the DNP method requires an electron-nucleon dipolar coupling. In the case of LaAlO_3 , electrons of paramagnetic impurities (Nd^{3+}) in the crystal are polarized with a sufficiently low temperature and high magnetic field, and this electron polarization is transferred to the nuclear spin of ^{139}La through a dipole interaction between the Nd^{3+} and ^{139}La spins by applying a microwave field nearly resonant to the ESR transition.

The high quality LaAlO_3 crystal with dimensions of the order of $4 \text{ cm} \times 4 \text{ cm} \times 6.6 \text{ cm}$ and the DNP system with large cooling power and high power microwave system, which can be installed at the beam line, is desirable in our plan. Developments of this equipment will begin soon.

7.3.4 Estimation of the measurement time

Firstly, the measurement time in the ideal condition is estimated. In the ideal condition, the polarization and the transmission of ^3He spin filter are 100% and 50%, respectively, and the polarization of the target nucleus is 100%. In this case, ΔA_x and ΔP_x are

$$\begin{aligned}\Delta A_x &= \frac{2\sqrt{N_{A+}^3 + N_{A-}^3}}{(N_{A+} + N_{A-})^2}, \\ \Delta P_x &= \frac{2\sqrt{N_{P+}^3 + N_{P-}^3}}{(N_{P+} + N_{P-})^2},\end{aligned}\tag{7.16}$$

and

$$N_{A-} = N_{A+} = N_{P-} = N_{P+} = \frac{1}{2} N e^{-\rho \sigma_{\text{tar}} d},\tag{7.17}$$

where ρ , σ_{tar} and d are the number density, the total cross section, the thickness of the target, respectively. Therefore, when we use the optimum thickness target, Eq 7.12 can be written as

$$\frac{2\sqrt{2}}{\sqrt{N}e^{-\rho\sigma_{\text{tar}}d}} < 8\text{Re}A^*D = 1.1 \times 10^{-5}. \quad (7.18)$$

Here, the transmission of the LaAlO_3 target with a thickness of 6.6 cm is 0.46 for 0.74 eV neutrons. Hence the required number of neutrons is $N > 1.41 \times 10^{11}$ n, and the measurement time is estimated as 2.2 hours.

Subsequently, the measurement time in the realistic condition is estimated. In the case that the polarization of the target and neutron beam is not 100%, P_x , A_x and sensitivity are given as

$$\begin{aligned} A_x &= 4(P_I P_n \text{Re}A^*D + P_I P_n^2 \text{Im}B^*C), \\ P_x &= 4(P_I P_n \text{Re}A^*D - P_I P_n^2 \text{Im}B^*C), \\ A_x + P_x &= 8P_I P_n \text{Re}A^*D. \end{aligned} \quad (7.19)$$

Assuming the ^3He spin filter whose thickness and ^3He polarization are 79 atm-cm and 70% and the LaAlO_3 whose thickness and nuclear polarization are 6.6 cm and 40 % are used, ΔA_x and ΔP_x need to satisfy following condition.

$$1.96\sqrt{\Delta A_x^2 + \Delta P_x^2} < 8P_I P_n \text{Re}A^*D = 3.8 \times 10^{-6}. \quad (7.20)$$

In this case, ΔA_x and ΔP_x can be written as

$$\Delta A_x = \frac{1}{\sqrt{2N}e^{-\rho\sigma_{\text{tar}}d}T}, \quad \Delta P_x = \frac{1}{\sqrt{2N}e^{-\rho\sigma_{\text{tar}}d}T} \frac{T}{\sqrt{T^2 - T_{00}^2}}. \quad (7.21)$$

Here $T_{00} = 0.15$, $T = 0.30$. Using these value, the number of neutrons must be $N > 2.23 \times 10^{12}$ n. Therefore the required measurement time is 1.4 day.

From the point of view of statistics, the most sensitive T-violation search is sufficiently possible using this method. However systematic errors, for example, the stabilities of the polarization of the ^3He and ^{139}La and the spin rotation of the incident neutron by pseudo magnetism, need to be considered very carefully.

Chapter 8

Conclusion

There is a possibility that T-violation can be searched sensitively by using a compound nucleus due to the CP-violation enhancement mechanism. However, x , which is needed to estimate the sensitivity of the T-violation search, has not yet been determined in all nuclei. The experiment to determine x of ^{139}La , which is a strong candidate for the T-violation search, has been carried out by measuring the angular distribution of emitted γ -rays from the 0.74 eV p-wave resonance. It was performed in ANNRI neutron beam line at J-PARC with a germanium detector assembly which has high energy resolution and large solid angle. The simulation of the detector using GEANT4 was constructed and accurate response functions of the detectors were obtained. The accurate relative detection efficiencies of γ -rays for all germanium crystals were also obtained with the $^{14}\text{N}(n,\gamma)$ reactions. Resulting from these precise corrections and the high statistics, a clear angular distribution of γ -rays emitted in the transition from the p-wave resonance of $^{139}\text{La} + n$ to the ground state of ^{140}La was observed.

The angular distribution was analyzed using the theoretical formalism based on the interference between the s-wave resonance and p-wave resonance in consideration of the thermal motion of the target nucleus and the time structure of the neutron beam. Consequently, x and other parameters to estimate the enhancement of the T-violation in the compound nucleus were obtained.

An additional experimental study of the (n,γ) reaction was also mentioned for a more detailed description of the compound nucleus, and we confirm that the a_2 term is useful in order to determine these parameters conclusively. Moreover, the experimental sensitivity for a T-violation search using ^{139}La was estimated and such an experiment is sufficiently feasible from the point of view of the statistical sensitivity.

Acknowledgment

First and foremost I would like to show my greatest appreciation to my supervisor, Professor Hirohiko Shimizu. He always gave great advice and warm support to me, even as a transfer student. His attitude as a scientist deeply influenced my life. It was one of the greatest fortunes in my life to spend my doctoral program as his student.

I also wish to express my gratitude to Associate Professor Masaaki Kitaguchi. I was supported by his continuous encouragement and kindness. I would like to thank Associate Professor Katsuya Hirota for his hospitality and technical advice for the experiment and analysis.

I would like to express my appreciation to all the collaborators of the NOP-TREX experiment and Neutron Optics and Physics. I would like to express my gratitude toward Associate Processor Tamaki Yoshioka. His advice on physics and my life always encouraged me. I would like to thank Mr. Shunsuke Takada, Mr. Tomoki Yamamoto, and Mr. Jun Koga. I especially had a great deal of discussions about physics and private issues with Mr. Shunsuke Takada, and we supported each other from the beginning of my doctoral program. I was also greatly supported by Mr. Tomoki Yamamoto when I was depressed. I really enjoyed the experiments in J-PARC and discussions with them. I would like to show my deep gratitude to Dr. Christopher C. Haddock. He always helped me with English study, and I really enjoyed sharing a lot of time in Los Alamos and Japan with him. I am looking forward to working on experiments together. I would like to offer my special thanks to Dr. Takashi Ino and Dr. Kenji Mishima. They gave me great support and advice for neutron experiments.

I owe a very important debt to the staff of the MLF at J-PARC for providing the neutron beam and the instruments for my experiment. In particular, Dr. Atsushi Kimura, Dr. Kenji Sakai, and Dr. Taro Nakao. Their technical support on beam line 04 and technical advice to analyze the measured data are very crucial for my research.

I deeply thank my father Satoshi, my mother Keiko and my grandparents, who gave me opportunities to study and financial support throughout my life. Finally, I would like to dedicate this thesis to Ms. Kaori Takahashi.

Appendix A

Neutron absorption cross section

The reaction between neutron and nucleus is described by the elastic scattering and absorption for low energy neutrons. Although several final states result from the neutron absorption reaction, for example γ -ray, neutron and proton emission and nuclear fission, exist, only the γ -ray emission reaction was described in this thesis.

The formula used to describe the neutron cross section σ_t is given as a function of the neutron energy in the center-of-mass system:

$$\sigma_t(E) = \sigma_s + \sigma_{n\gamma}(E_n), \quad (\text{A.1})$$

$$\sigma_s = 4\pi a^2, \quad (\text{A.2})$$

$$\Gamma_r^\gamma = \sum_f \Gamma_{r,f}^\gamma, \quad (\text{A.3})$$

$$\sigma_{n\gamma}(E_n) = \sum_f \sigma_{n\gamma_f}(E_n), \quad (\text{A.4})$$

$$\sigma_{n\gamma_f}(E_n) = \sum_r \sigma_{nr\gamma_f}, \quad (\text{A.5})$$

$$\begin{aligned} \sigma_{nr\gamma_f}(E_n) = & \frac{\pi \hbar^2}{2m_n E_n} \left[\frac{E_n}{E_r} \right]^{l_r+1/2} \\ & \times \frac{g_r \Gamma_r^n \Gamma_{r,f}^\gamma}{(E_n - E_r)^2 + (\Gamma_r/2)^2}, \end{aligned} \quad (\text{A.6})$$

where σ_s is the scattering cross section, $\sigma_{n\gamma}$ is the radiative capture cross section, $k_n = \sqrt{2m_n E_n}/\hbar$, a is the scattering length, E_r is the resonance energy of the r -th resonance, $g_r = (2J_r + 1)/(2(2I + 1))$ is the statistical factor with the target nuclear spin I and the spin of the r -th resonance J_r , Γ_r^n is the neutron width of r -th resonance, and $\Gamma_{r,f}^\gamma$ is the γ -width of the γ -ray transition from the r -th resonance to the final state f . The quantity l_r represents the orbital angular momentum of the incident neutrons

contributing to r -th resonance. The above formula is valid for $l_r = 0, 1$. Higher angular momenta can be ignored in the incident neutron energy region of our interest.

Bibliography

- [1] T. D. Lee and C. N. Yang. Question of parity conservation in weak interactions. *Phys. Rev.*, 104:254–258, 1956.
- [2] C. S. Wu, E. Ambler, R. W. Hayward, D. D. Hoppes, and R. P. Hudson. Experimental test of parity conservation in beta decay. *Phys. Rev.*, 105:1413–1415, 1957.
- [3] R. L. Garwin and L. M. Lederman. *Nuovo Cim.*, 11:776, 1959.
- [4] J. I. Friedman and V. L. Telegdi. Nuclear emulsion evidence for parity non- conservation in the decay chain $\pi^+ \rightarrow \mu^+ \rightarrow e^+$. *Phys. Rev.*, 105:1681–1682, 1957.
- [5] J. H. Christenson, J. W. Cronin, V. L. Fitch, and R. Turlay. Evidence for the 2π decay of the K_S^0 meson. *Phys. Rev. Lett.*, 13:138–140, 1964.
- [6] W. M. Yao and et al. *Review of particle physics. J. phys. G: Nucl. Part. Phys.*, 33:1, 2006.
- [7] K. Abe and et al. <http://arxiv.org/abs/hep-ex/0202027>. 2002.
- [8] B. Aubert and et al. <http://arxiv.org/abs/hep-ex/0203007>. 2002.
- [9] C. Amsler and et al. *Physics. Letters. B*, 667:1–6, 2008.
- [10] C. G. Callan and et al. *Physics. Letters. B*, 63:334, 1976.
- [11] H.Y. Cheng. *Physics Reports*, 158:1, 1988.
- [12] J. Schwinger. *Phys. Rev.*, 82:914, 1951.
- [13] J. Schwinger. *Phys. Rev.*, 91:713, 1953.
- [14] G. R. Farrar. *Phys. Rev. D*, 50:774, 1994.
- [15] A. D. Sakharov. *JETP Lett.*, 5:24, 1967.
- [16] Pospelov Ritz and Adam Ritz. Electric dipole moments as probes of new physics. *Ann Phys.*, 318 (05):119–169, 2005.
- [17] P. G. H. Sandars and E. Lipworth. Electric dipole moment of the cesium atom. a new upper limit to the electric dipole moment of the free electron. *Phys. Rev. Lett.*, 13(24):718–720, 1964.

- [18] Eugene D. Commins, Stephen B. Ross, David DeMille, and B. C. Regan. Improved experimental limit on the electric dipole moment of the electron. *Phys. Rev. A.*, 50:2960–2977, 1994.
- [19] B. C. Regan, Eugene D. Commins, Christian J. Schmidt, and David DeMille. Improved experimental limit on the electric dipole moment of the electron. *Phys. Rev. Lett.*, 88:071805, 2002.
- [20] P. G. H. Sandars. *Phys. Lett. B*, 14:194, 1965.
- [21] Z. W. Liu and H. P. Kelly. *Phys. Rev. A*, 45:R4210, 1992.
- [22] J. S. M. Ginges and V. V. Flambaum. *Phys. Rep.*, 397:63, 2004.
- [23] J. J. Hudson, B. E. Sauer, M. R. Tarbutt, and E. A. Hinds. Measurement of the electron electric dipole moment using ybf molecules. *Phys. Rev. Lett.*, 89:023003, 2002.
- [24] L. I. Schiff. Measurability of nuclear electric dipole moments. *Phys. Rev.*, 132:2194–2200, 1963.
- [25] W. C. Griffith, M. D. Swallows, T. H. Loftus, M. V. Romalis, B. R. Heckel, and E. N. Fortson. Improved limit on the permanent electric dipole moment of ^{199}Hg . *Phys. Rev. Lett.*, 102:101601, 2009.
- [26] P. Harris. The neutron edm experiment. *arXiv*, pages 0709.3100v3 [hep-ex], 2007.
- [27] J. H. Smith, E. M. Purcell, and N. F. Ramsey. *Phys. Rev.*, 108 (1):120–122, 1957.
- [28] P. D. Miller, f W. B. Dress, J. K. Baird, and Norman F. Ramsey. *Phys. Rev. Lett.*, 19 (7):381–384, 1967.
- [29] W. B. Dress, J. K. Baird, P. D. Miller, and Norman F. Ramsey. *Phys. Rev.*, 170 (5):1200–1206, 1968.
- [30] J. K. Baird, P. D. Miller, W. B. Dress, and Norman F. Ramsey. *Phys. Rev.*, 179 (5):1285–1291, 1969.
- [31] W. B. Dress, P. D. Miller, and N. F. Ramsey. *Phys. Rev. D.*, 7 (11):3147–3149, 1973.
- [32] Dress W. B, P. D. Miller, J. M. Pendlebury, Paul Perrin, and Norman F. Ramsey. *Phys. Rev. D.*, 15(1):9–21, 1977.
- [33] I. S. Altarev, Yu. V. Borisov, A. B. Brandin, A. I. Egorov, V. F. Ezhov, S. N. Ivanov, V. M. Iobashov, V. A. Nazarenko, G. D. Porsev, V. L. Ryabov, A. P. Serebrov, and R. R. Tal'daev. *Nuc. Phys. A*, 341(2):269–283, 1980.
- [34] I. S. Altarev, Yu. V. Borisov, A. B. Brandin, A. I. Egorov, V. F. Ezhov, S. N. Ivanov, V. M. Iobashov, V. A. Nazarenko, G. D. Porsev, V. L. Ryabov, A. P. Serebrov, and R. R. Tal'daev. *Phys. Lett.*, 102B (1):13–16, 1981.
- [35] J.M. Pendlebury et al. *Phys. Lett*, 136B (5,6):327–330, 1984.

- [36] I. S. Altarev, Yu. V. Borisov, A. B. Brandin, A. I. Egorov, S. N. Ivanov, E. A. Kolomenskii, M. S. Lasakov, V. M. Iobashov, A. N. Pirozhkov, A. P. Serebrov, Yu. V. Sobolev, R. R. Tal'daev, and B. V. Shul'gina. *JETP. Lett.*, 44(8):460–464, 1986.
- [37] K. F. Smith, D. J. Richardson, D. Shiers, N. Crampin, J. M. Pendlebury, K. Green, A.I. Kilvington, J. Moir, H.B. Prosper, D. Thompson, N. F. Ramsey, B.R. Heckel, S.K. Iamoraux, P. Ageron, and W. Mampe and. *Phys. Lett.B.*, 234(1,2), 1990.
- [38] I. S. Altarev, Yu. V. Borisov, N. V. Borovikova, S. N. Ivanov, E. A. Kolomensky, M. S. Lasakov, V. M. Iobashov, V. A. Nazarenko, A. N. Pirozhkov, A. P. Serebrov, Yu. V. Sobolev, E. V. Shulgina, A. I. Yegorov, and A. Steyerl. *Phys. Lett. B*, 276:242–246, 1992.
- [39] P. G. Harris, C. A. Baker, K. Green, P. Iaydjiev, S. Ivanov, D. J. R. May, J. M. Pendlebury, D. Shiers, K. F. Smith, M. van der Grinten, , and P. Geltenbort. *Phys. Rev. Lett.*, 85(1), 1999.
- [40] C. A. Baker, D. D. Doyle, P. Geltenbort, K. Green, M. G. D. van der Grinten, P. G. Harris, P. Iaydjiev, S. N. Ivanov, D. J. R. May, J. M. Pendlebury, J. D. Richardson, D. Shiers, , and K. F. Smith. *Phys. Rev. Lett.*, 97:131801, 2006.
- [41] J. M. Potter, J. D. Bowman, C. F. Hwang, J. L. McKibben, R. E. Mischke, D. E. Nagle, P. G. Debrunner, H. Frauenfelder, and L. B. Sorensen. *Phys. Rev. Lett.*, 33:1307, 1974.
- [42] V. Yuan, H. Frauenfelder, R. W. Harper, J. D. Bowman, R. Carlini, D. W. MacArthur, R. E. Mischke, D. E. Nagle, R. L. Talaga, and A. B. McDonald. *Phys. Rev. Lett.*, 57:1680, 1986.
- [43] E. G. Adelberger and W. C. Haxton. *Ann. Rev. Nucl. Part. Sci.*, 35:501, 1985.
- [44] V. P. Gudkov. *Phys. Rep.*, 212:77, 1992.
- [45] V. P. Gudkov. *private communication*.
- [46] P. Hautle and M. Inuma. *NIM A.*, 440:638, 2000.
- [47] M. Bulatowicz, R. Griffith, M. Larsen, and J. Mirijanian. *Phys. Rev. Lett.*, 111:102001, 2013.
- [48] K. Shibata, O. Iwamoto, T. Nakagawa, N. Iwamoto, A. Ichihara, S. Kunieda, S. Chiba, K. Furutaka, N. Otuka, T. Ohsawa, T. Murata, H. Matsunobu, A. Zukeran, S. Kamada, and J. Katakura. Jendl-4.0: A new library for nuclear science and engineering. *J. Nucl. Sci. Technol.*, 48:1–30, 2011.
- [49] S. F. Mughabghab. *Atlas of Neutron Resonances 5th ed.* Elsevier, Amsterdam, 2006.
- [50] R. Terlizzi and others (n TOF Collaboration). The $^{139}\text{La}(n,\gamma)$ cross section: Key for the onset of the s-process. *Phys. Rev. C*, 78:035807, 2007.
- [51] G. Hacken, J. Rainwater, H. I. Liou, and U. N. Singh. Neutron resonance spectroscopy : ^{139}La . *Phys. Rev. C*, 13:1884, 1976.

- [52] web site of J-PARC. <http://www.toshiba-tetd.co.jp/eng/casestudy/jparc.htm>. Accessed: 2017-10-10.
- [53] J-PARC web site. <https://j-parc.jp/researcher/MatLife/ja/instrumentation/index.html>. Accessed: 2017-11-20.
- [54] K. Kino, M. Furusaka, F. Hiraga, T. Kamiyama, Y. Kiyanagi, K. Furutaka, S. Goko, H. Harada, M. Harada, T. Kai, A. Kimura, T. Kin, F. Kitatani, M. Koizumi, F. Maekawa, S. Meigo, S. Nakamura, M. Ooi, M. Ohta, M. Oshima, Y. Toh, M. Igashira, T. Katabuchi, and M. Mizumoto. Measurement of energy spectra and spatial distributions of neutron beams provided by the annri beamline for capture cross-section measurements at the j-parc/mlf. *Nucl. Instrum. Methods A*, 626-627:58, 2011.
- [55] Susumu Ikeda and John M. Carpenter. *Nucl. Instrum. Methods A*, 239:536, 1985.
- [56] I. Cole and C. G. Windsor. *Nucl. Instr. and Meth*, 171:107, 2002.
- [57] M. C. Moxon, T. C. Ware, and C. J. Dean. *Users ' Guide for REFIT-2009-10*, 2010.
- [58] M. C. Moxon, T. C. Ware, and C. J. Dean. *J. Nucl. Sci. Technol. Suppl*, 2:685, 2002.
- [59] H. J. Stone, M. G. Tucker, Y. Le Godec, F. M. Meducin, E. R. Cope, S. A. Hayward, G. P. J. Ferlat, W. G. Marshall, S. Manolopoulos, S. A. T. Redfern, and M. T. Dove. *Nucl. Instr. Meth. Phys. Res. A*, 547:601, 2005.
- [60] H. J. Stone, M. G. Tucker, F. M. Meducin, M. T. Dove, and S. A. T. Redfern. *J. Appl. Phys.*, 98:064905, 2005.
- [61] H. Ikeda. J-parc status update. *Nucl. Instrum. Meth. Phys. Res.*, A600:1, 2009.
- [62] T. Kin et al. *The 2009 NSS-MIC Conference Record. Orland. USA. October 2009*, pages 1194–1197, 2009.
- [63] CAEN. <http://www.caen.it/>. Accessed: 2017-10-01.
- [64] C. D. Bowman, J. D. Bowman, and V. W. Yuan. *Phys. Rev. C*, 39:1721, 1989.
- [65] Y.H.Song, R. Lazauskas, and V. Gudkov. *Phys. Rev. C.*, 83:065503, 2011.
- [66] Jason A. Fry. *PhD. thesis*, 2015.
- [67] J-PARC web site. http://www.j-parc.jp/researcher/MatLife/ja/instrumentation/deta/Pulse_0310_mod.pdf. Accessed: 2017-10-01.
- [68] T. R. Gentile, P. J. Nacher, B. Saam, and T. G. Walker. Optically polarized ^3He . *arXiv*, pages 1612.04178v2 [physics.atom-ph], 2017.